Direct imaging of free-standing clay mineral nanosheets and their molecular complexes via multivalent electrostatic interactions using scanning transmission electron microscopy

Free-standing な粘土鉱物ナノシートと多重静電相互作用による
有機分子複合体の走査透過電子顕微鏡観察

A dissertation submitted in partial fulfillment of the requirements

for the degree of Doctorate in Engineering

By

Ikumi AKITA

Division of Materials Science and Engineering,

Graduate School of Engineering, Hokkaido University,

Kita 13 Nishi 8, Kita-ku, Sapporo, Hokkaido 060-8628, Japan.

March 2021

Contents

Chapter 1

General Introduction

1.1 Supramolecular assemblies based on two-dimensional nanomaterials

Originating from the early discoveries by Pedersen, Cram, and Lehn,[1,2] supramolecular assembly is one of the most important topic in nanomaterials science in recent decades. Supramolecular assemblies are constructed by non-covalent interaction between the molecules as blocks, such as coordination bonds, hydrogen bonds, van der Waals interactions, and electrostatic interactions.[3] Their high flexibility in design than systems using covalent bonds fascinates the exploration of the possibility for wide range of applications, e.g. sensing, separation, catalytic, and biomedical technologies. The functionalization of ultrathin two-dimensional (2D) nanomaterials, termed "2D nanosheets," is one of the fields where supramolecular structuring via non-covalent interaction is extensively used.[4,5]

2D nanosheet is an emerging class of nanomaterials that possess sheet-like structures with the lateral size larger than 100 nm, or up to a few micrometers and even larger, but the thickness is only one- or few-atoms thick (typically less than 5 nm).[6–8] The growth of graphene research [8–12] has led to exploring family of 2D nanosheets such as hexagonal boron nitride (h-BN),[13,14] transition metal dichalcogenides (TMDs),[12,15] graphitic carbon nitride (g-C_3N_4),[16,17] layered metal oxides,[18,19] layered double

hydroxides (LDHs),[18,20] MXenes,[21,22] metal−organic frameworks (MOFs),[23,24] covalent−organic frameworks (COFs),[25,26] black phosphorus (BP),[8] silicene,[27,28] antimonene,[29–31] and perovskites.[32–34] The atomically thin nature of these materials results in unique structural and physical properties and provides access to novel fundamental properties which are not present in their bulk counterparts. Common properties of 2D nanosheet are summarized below. First, the confinement of electrons in two dimensions in the ultrathin region, especially for single-layer 2D nanomaterials, facilitates their compelling electronic properties, which are ideal for the fundamental study in condensed matter physics and electronic/optoelectronic devices. Second, the strong in-plane covalent bond and atomic thickness enable their excellent mechanical strength, flexibility, and optical transparency, which are important for utilization in the next generation devices.[35,36] Third, the ultrahigh specific surface area is exceedingly attractive for those surface-related applications such as catalysis and supercapacitors.[36,37] Fourth, the solution-based processability of ultrathin 2D nanomaterials is essential for fabrication of high-quality free-standing thin films via simple methods, such as vacuum filtration, spin coating, drop casting, spray-coating, and inkjet printing.[38–41]

In addition to these features, the most noteworthy is the structure of 2D nanosheet with all atoms exposed, which allows highly effective surface functionalization or modification by organic molecules. Both non-covalent and covalent functionalization approaches are highly promising methods for the controlled modification of a number of properties such as dispersion in solutions, tuning of the electronic band structure and transport properties.[4,5] Covalent functionalization of molecules on 2D materials provides a more robust approach for controllably tuning the properties of 2D materials, but causes detrimental effects on the novel properties 2D nanosheet by affecting on their structure.

Non-covalent functionalization of 2D nanosheets does not disrupt the crystal structure of nanosheets while, they exhibits less robust structure due to weak non-covalent (supramolecular) interaction between molecules and nanosheet surfaces. A systematic control over the degree and site of functionalization would result in better control over the optoelectronic properties of 2D nanosheet based materials.

1.2 Fascinating properties of clay mineral nanosheet

Clay mineral nanosheet is a 2D nanosheet with a thickness of *ca.* 1 nm obtained by exfoliating a single layer of clay minerals, featuring physicochemical properties such as atomically flat surfaces with a large surface area, high surface charges, and high thermal stability.[42,43] Clay mineral nanosheets have been used as host material to build supramolecular assemblies for photochemical reaction.[42,44–47] Clay minerals are phyllosilicates or layered materials which are frequently used in various field such as selective adsorption for heterogeneous catalyst or sensing,[48] or photoenergy conversion,[49] as well as agricultural or architectural uses. Unite layer of clay minerals consists of one sheet of SiO_4 tetrahedral sheet joined to one sheet of Al (or Mg) octahedral sheet, or of one Al (or Mg) octahedral sheet sandwiched by two of SiO_4 tetrahedral sheets as shown in Figure 1. The former are called 1:1, the latter 2:1 clay minerals. Those with an Al-octahedral sheet are called dioctahedral; those with a Mg-octahedral sheet, trioctahedral.

Surface of clay minerals is negatively charged due to isomorphic substitutions, such as Si^{4+} by Al^{3+} in the tetrahedral sheets or Al^{3+} by Mg^{2+} in the Al-octahedral sheets. Exchangeable cations, such as Na^{+}, balance the negative surface charge of clay particles.

The intercalation and adsorption via cation exchange reactions of organic and inorganic molecules into the interlayer space of clay minerals have been extensively reported. Relatedly, owing to the surface charges, interlayers of the clay have a reversibly swelling ability with solvents especially with water (Figure 2a). Generally, the swelling ability depends on the charge density on the clay surface, which is described as cation exchange capacity (CEC). A general classification of clay minerals by the structure and CEC is shown in Table. Clay minerals can be obtained by purification of natural clays, while chemical synthesis has been also developed especially in saponite clays.[50]

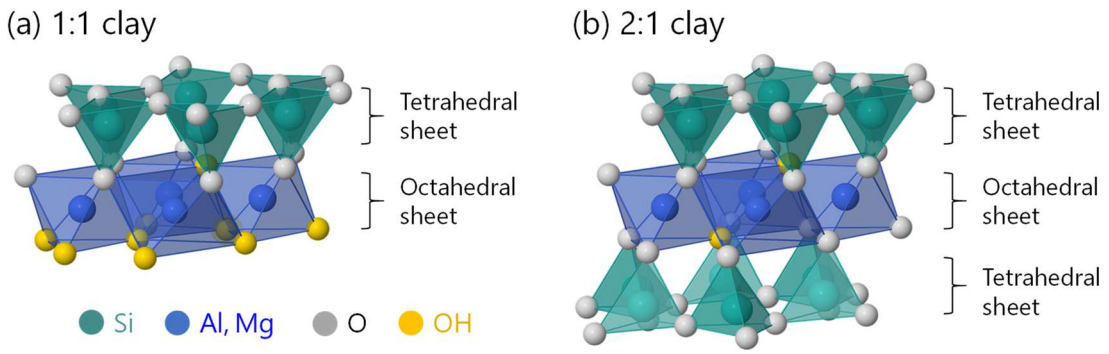

Figure 1. Typical atomic structure of (a) 1 :1 and (b) 2 :1 clay minerals.

Table. The classification of clay minerals.[45]

Clay	Ideal composition $M_{int}(M_{oct})(M_{tetra})O_1(OH)_m \cdot nH_2O$[a]	Layer type	Schematic structure[b]
1:1			
Kaolinite group (charge density ~ 0 per unit)			
Kaolinite	$(Al_2)(Si_2)O_5(OH_4)$	Dioctahedral	
Halloysite	$(Al_2)(Si_2)O_5(OH_4)\cdot 2H_2O$	Dioctahedral	
Serpentine group (charge density ~ 0 per unit)			
Serpentine	$(Mg_6)(Si_4)O_{10}(OH)_8$	Trioctahedral	
2:1			
Pylophyllite group (charge density ~ 0 per unit)			
Pyrophyllite	$(Al_2)(Si_4)O_{10}(OH)_2$	Dioctahedral	
Talc	$(Mg_3)(Si_4)O_{10}(OH)_2$	Trioctahedral	
Smectite group (charge density: x ~ 0.2–0.6 per unit)			
Montmorillonite	$M_x(Al_{2-x}Mg_x)(Si_4)O_{10}(OH)_2\cdot nH_2O$	Dioctahedral	
Beidellite	$M_x(Al_2)(Si_{4-x}Al_x)O_{10}(OH)_2\cdot nH_2O$	Dioctahedral	
Nontronite	$M_x(Fe_2^{3+})(Si_{4-x}Al_x)O_{10}(OH)_2\cdot nH_2O$	Dioctahedral	
Saponite	$M_x(Mg_3)(Si_{4-x}Al_x)O_{10}(OH)_2\cdot nH_2O$	Trioctahedral	
Hectorite	$M_x(Mg_{3-x}Li_x)(Si_4)O_{10}(OH)_2\cdot nH_2O$	Trioctahedral	
Vermiculite group (charge density: x ~ 0.6–0.9 per unit)			
Dioctahedral vermiculite	$M_x(Al_{2-y}Fe_4^{3+})(Si_{4-x}Al_x)O_{10}(OH)_2\cdot nH_2O$	Dioctahedral	
Trioctahedral vermiculite	$M_x(Mg_3)(Si_{4-x}Al_x)O_{10}(OH)_2\cdot nH_2O$	Trioctahedral	
Mica group (charge density: x ~ 0.6–1 per unit)			
Mica (muscovite)	$K(Al_2)(Si_3Al)O_{10}(OH)_2$	Dioctahedral	
Illite	$K_x(Al_2)(Si_{4-x}Al_x)O_{10}(OH)_2$	Dioctahedral	
Biotite	$K[(Mg, Fe^{2+})(Fe^{3+}, Al, Ti)](Si, Al)_4O_{10}(OH)_2$	Trioctahedral	
Chlorite group			
Cookeite	$[LiAl_2(OH)_6][(Al_2)(Si_3Al)O_{10}(OH)_2]$	Dioctahedral	
Clinochlore	$[Mg_2Al(OH)_6][(Mg_3)(Si_3Al)O_{10}(OH)_2]$	Trioctahedral	
Chamosite	$[Fe_2Al(OH)_6][(Mg_3)(Si_3Al)O_{10}(OH)_2]$	Trioctahedral	
Channel type			
Sepiolite	$M^{2+}_{(x+y+2z)/2}(Mg_{8-y-z}M_y^{3+}\square_z)(Si_{12-x}M_x^{3+})O_{30}(OH)_4(OH_2)_4\cdot 8H_2O$		
Palygorskite	$M^{2+}_{(x-y+2z)/2}(Mg_{5-y-z}M_y^{3+}\square_z)(Si_{8-x}M_x^{3+})O_{20}(OH)_2(OH_2)_4\cdot 4H_2O$		

[a] M_{int}: intercalated metal cations; M_{oct}: cations occupying octahedral position; M_{tetra}: cations occupying tetrahedral position.
[b] ▱: tetrahedral sheet; ▭: octahedral sheet; ▬: OH surface; ⊙: H_2O; ⊕: interlayer cation.

Among many types of clay minerals, smectite groups (e.g., saponite, montmorillonite) has moderate anionic charge density imparting exfoliation (or stacking) ability to individual monolayers in aqueous solutions. The general chemical formula of smectite is $[(Si_{8-x}Al_x)(Mg_{6-y}Al_y)O_{20}(OH)_4]\cdot(x-y)Y^+$, where Y represents the balancing cations that compensate for the anionic charge. Monolayer of smectite is composed of tetrahedral and octahedral sheets in a 2:1 ratio (Figure 2b). The thickness of the obtained monolayers is *ca.* 1 nm, while the particle size is tens to hundreds of nanometers. A

completely exfoliated clay mineral (i.e., monolayer) can thus be defined as a family of 2D nanosheets and termed "clay mineral nanosheet (Figure 2b)". Clay mineral nanosheets offer unique characteristics atomically flat surfaces with a large surface area,[51] high surface charges (i.e., ion exchange capacity), high thermal stability, and optical transparency of smaller exfoliated particles in visible light.[42,48,49,52] This is not the case for clay minerals without isomorphous substitution such as kaolinite, pyrophyllite, and talc, because of the very strong attractive interactions between the layers.

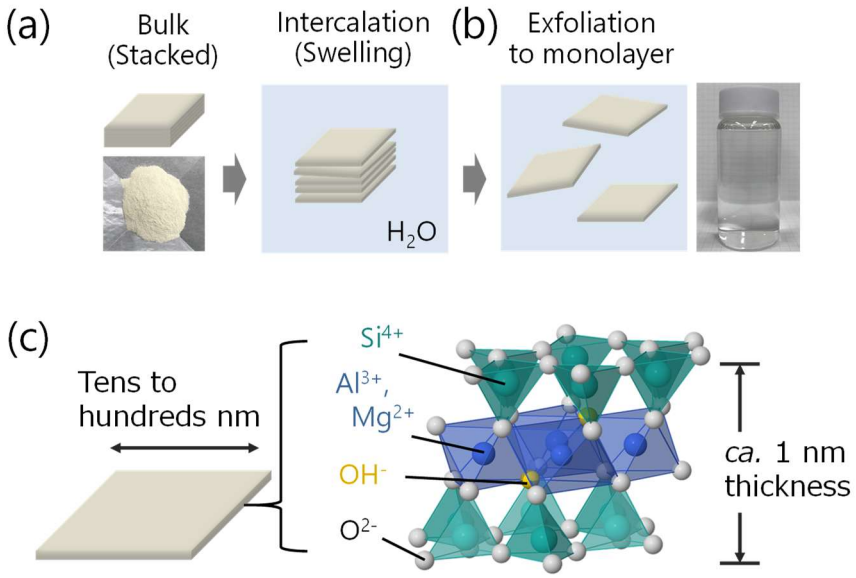

Figure 2. Schematic images of (a) swelling, (b) monolayer exfoliation process of clay minerals by immersion in water. (c) Atomic structure of montmorillonite.

1.3 Previous studies for organic molecules-clay mineral nanosheet supramolecular assemblies via electrostatic interaction

Anionic charged clay nanosheets have been used as a host material to build a supramolecular assembly of organic molecules without aggregation via (multivalent) electrostatic interaction for photochemical reaction (Figure 3a).[49] Interactions between clay minerals and cationic organic dye molecules, such as porphyrins and related structured molecules, cause significant changes in the optical, spectral and chemical properties of the chromophores. These changes are due to the formation of supramolecular assemblies of the molecules, and can be and applied in nanoscale devices of optical memory systems, optical switching systems, amplifiers, energy storage devices and solar cells.[42] However, cationic organic molecules easily form aggregates owing to hydrophobic interactions and van der Waals interactions (Figure 3b), and thus it is difficult to control their 2D-alignment on the clay surface.[42,52] Since aggregation formation drastically decreases the excited state lifetime (i.e., self-quenching), efficient photochemical reactions have been regarded as impossible in organic dye molecule-clay mineral assemblies.

Inoue and Takagi et al. reported a novel mechanism to build a supramolecular assembly of organic dye molecules on clay mineral nanosheet without aggregation via multivalent electrostatic interaction (Figure 3c). Through systematic experiments using numerous cationic porphyrin derivatives (Figure 4) and synthetic saponite with different CEC,[53] it has been revealed that such non-aggregated alignment results from distance matching between the intramolecular cationic charge distance of molecules and the anionic surface charge distance of clay mineral nanosheet (Figure 4,). Even 100% vs.

CEC adsorption without aggregation was realized when the inter-cationic charge distance in the porphyrin molecules matches well to the inter-anionic charge distance on the clay surface. Takagi *et al.* termed this effect a "Size-Matching Effect" (Figure 3c), when ΔL (the difference between the inter-cationic charge distance in the porphyrin molecule and the inter-anionic charge distance on the clay surface) is less than or equal to 0.2 nm.

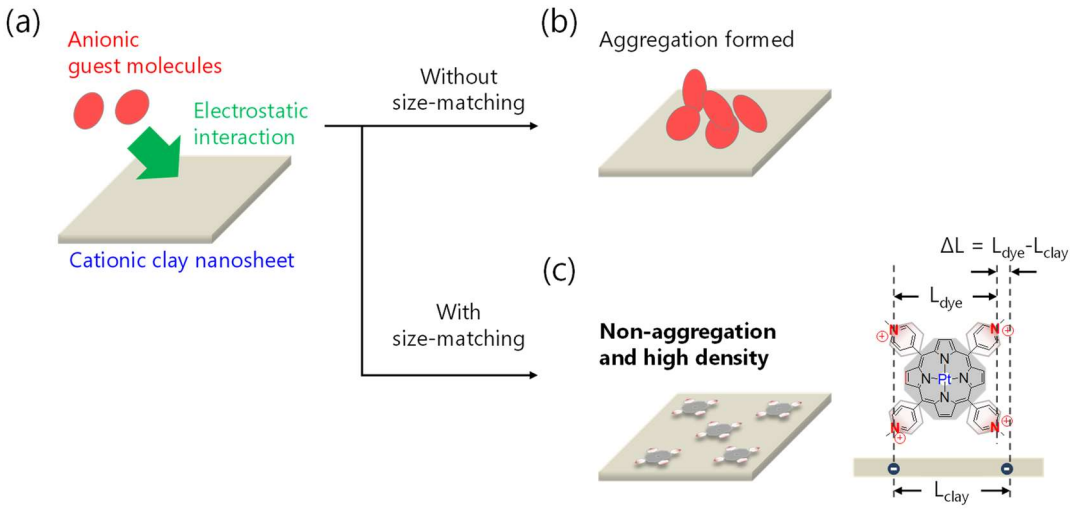

Figure 3. Schematic images of (a) organic molecule-clay mineral nanosheet self-assemblies via electrostatic interactions, (b) typical aggregation formation of molecules on solid surfaces, and (c) non-aggregated and high density adsorption of molecules following size matching effect.

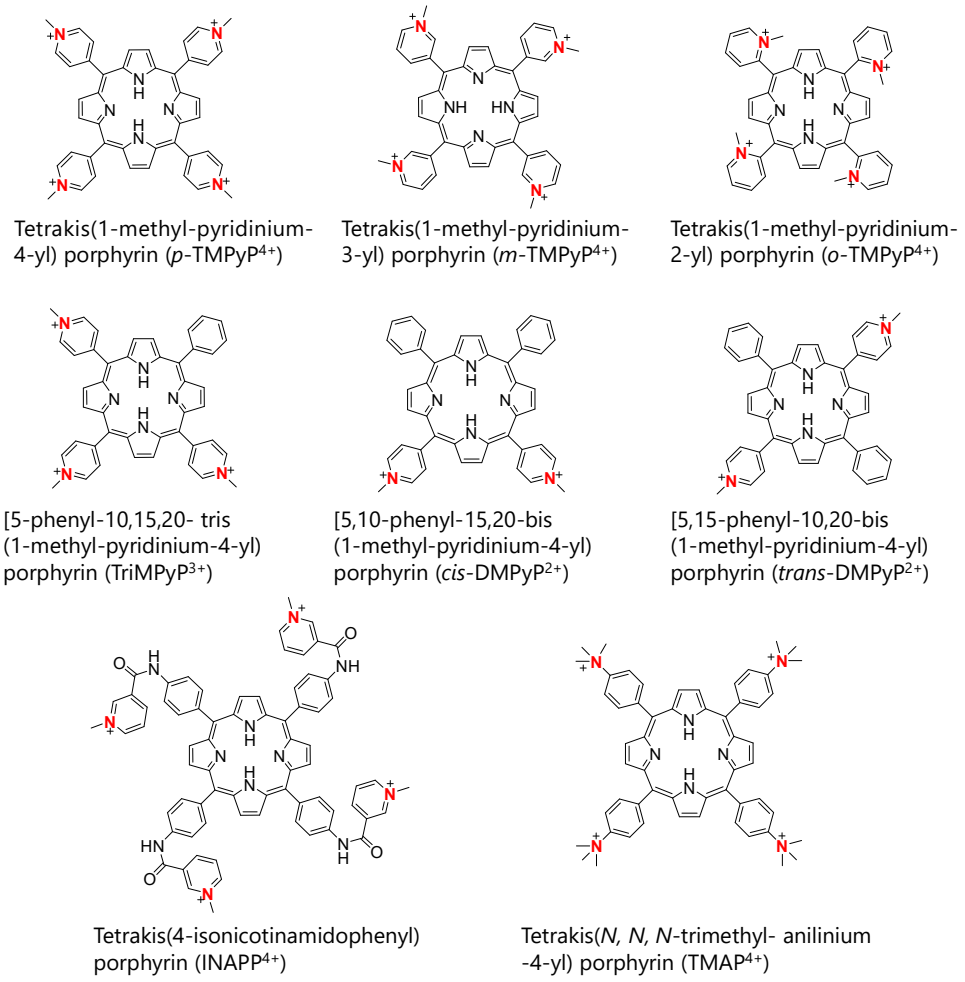

Figure 4. Structural formula of porphyrin derivatives.

The adsorption behavior of porphyrin molecules on the clay surface was primarily interpreted by the absorption spectra.[6,7,54] General UV-visible spectrum of porphyrin derivetes exhibits a very intense Soret band in the 400- to 500-nm region, corresponding to the porphyrin π-π* transition/ the porphyrin ring structure with 18p electrons in the conjugated system, and less intense Q-bands in the 500- to 700-nm region. For example, the absorption spectra of tetrakis(1-methylpyridinium-4-yl) porphyrin (*p*-TMPyP) in aqueous solution (free) and complexed with clay mineral nanosheet (with clay) exhibits 30 nm red-shift upon adsorption on the clay surface. The unique absorption

spectral shifts of porphyrin molecules upon adsorption on the clay surface was experimentally confirmed to be the flattening of the meso substituent with respect to the plane of the porphyrin ring.[55] The spectral shapes are the same below 100% vs CEC of the clay. Here, the concentration of molecules on the clay mineral nanosheets was expressed as the loading level vs. the cation exchange capacity (CEC) of the clay, which is the ratio between the amount of cation charges of the molecule and the CEC of the clay mineral nanosheet. Specifically, a loading level of 100% vs. CEC of the clay indicated that the number of cationic sites in the guest adsorbed on the clay surface was the same as the number of anionic sites on the clay surface. Above 100% CEC, absorption spectra consist of two components. The absorption at 450 nm is the component of adsorbed porphyrin on the clay surface, and 420 nm is the component of non-adsorbed porphyrin in a bulk solution. Absorbance concentration plot at 450 nm and 420 nm clearly indicates that *p*-TMPyP can adsorb on the clay surface below 100% CEC (Figure 5b). Moreover, linearity of the plot suggests that there is no aggregation. Aggregation is defined as the interaction between transition dipole moments of molecules resulting the appearance of different absorption components. While organic molecules tend to be aggregated on the solid surfaces mainly due to the hydrophobic interaction in general, cationic porphyrin molecules can exist as a single molecule unit.

According to the results of spectroscopic measurements, the schematic image of the *p*-TMPyP/clay complex is described in Figure 6a. In the case of tetra cationic porphyrins-clay complexes, the average center-to-center intermolecular distance is calculated to be 2.4 nm at 100% CEC condition on the basis of hexagonal array. If the distribution of intermolecular distance is wide, the spectral change due to the exciton coupling could be observed for the components whose intermolecular distances are short. Since such spectral changes were not observed at all (Figure 5b), the distribution of intermolecular distance should be pretty narrow in the porphyrin-clay complexes. This intermolecular distance is most interesting from the viewpoint of photochemical reactions, since there is almost no interaction between the transition moments of porphyrin molecules. It surely avoids the drastic decrease of the excited-state lifetime, if they cannot interact with each other in the excited state.

The structure determined by conventional method including spectroscopy is, however, based on the data averaged over molecules or time and often both, indicating the exclusion of fluctuation and inhomogeneity. Especially for supramolecular assemblies with non-periodic structure, the local structure including actual intermolecular distance, intermolecular and intramolecular orientation on clay surfaces is remained issue to understand the correlation between structural characteristics and properties or functionalities (Figure 6b). According to recent excellent works on imaging of single organic molecules combined with low-dimensional materials in the next section, I propose that most promising method is aberration corrected transmission electron microscopy (TEM) and scanning transmission electron microscopy c(STEM).

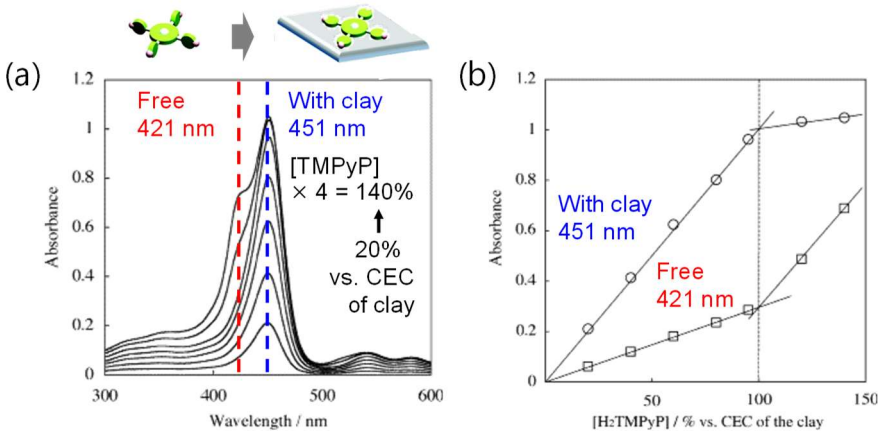

Figure 5. (a) Absorption spectra of *p*-TMPyP/saponite complex at various porphyrin concentrations at 20, 40, 60, 80, 95, 120, 140% vs. CEC of the clay. (b) Absorbance-concentration plots for *p*-TMPyP/saponite complex at Soret band maxima (with clay; 451 nm, free; 420 nm) in aqueous solution.[56]

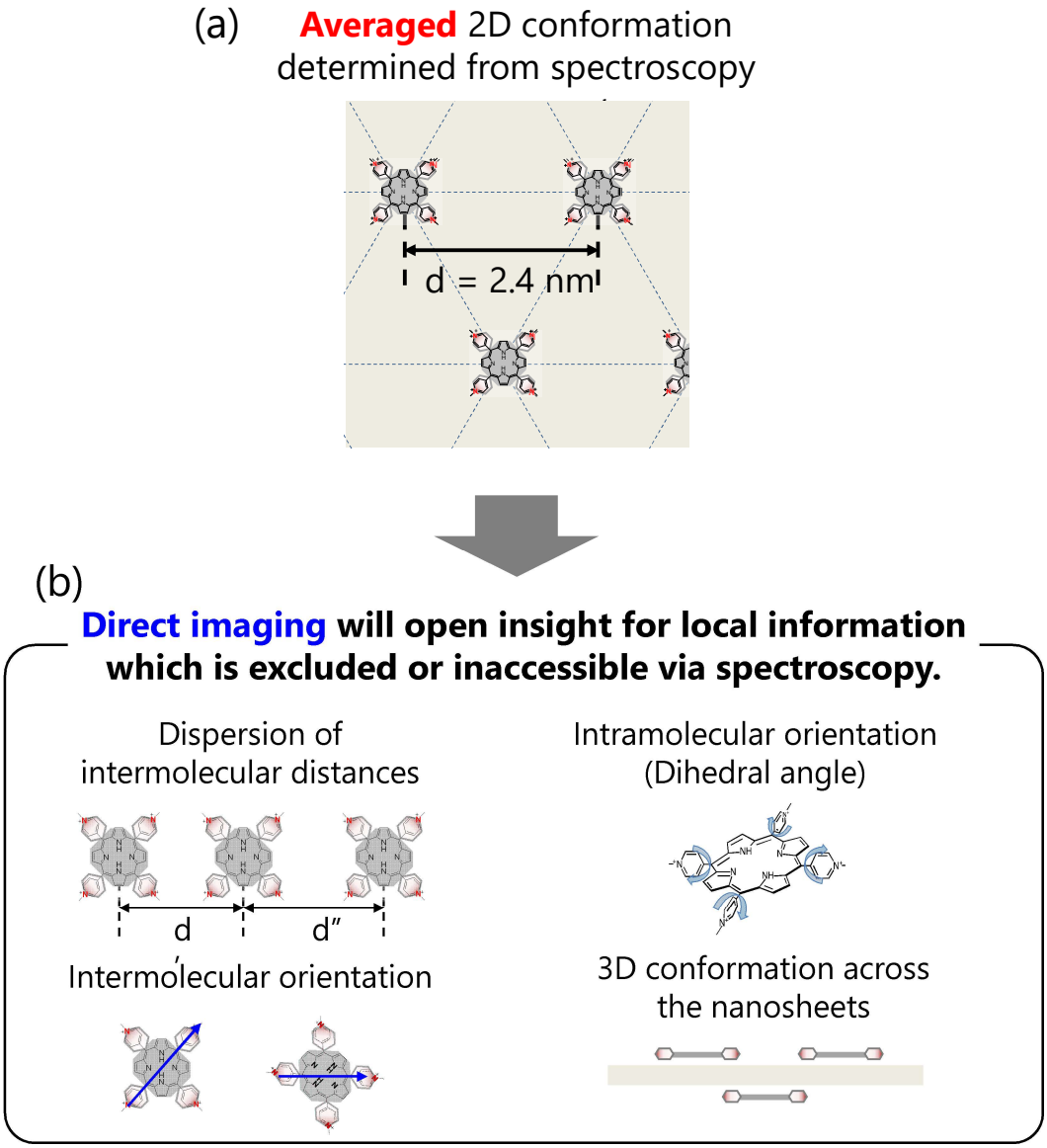

Figure 6. The schematic image for the structure of *p*-TMPyP/clay complex. The average center-to-center intermolecular distance is calculated to be 2.4 nm at 100% vs. CEC. (b) The representative local structural information of organic molecules-clay mineral nanosheet assemblies which would be revealed by direct imaging.

1.4 Imaging of individual single molecules using aberration corrected S/TEM

Aberration corrected TEM and STEM[57–59] are the most promising technique that allows direct imaging of the local structure of nanomaterials at the atomic resolution.[6,7,54,60–64] Improved electron microscopic equipment including aberration corrected optics and techniques for the precise control of low-dimensional nanomaterials have led to advancements in the direct observation of single organic molecules and their supramolecular assemblies.[65,66] Due to the use of high energy electron beam, however, direct imaging of the individual molecules by S/TEM includes some challenges: (i) suppression of electron beam damage, (ii) effective fixation of molecules during observation, and (iii) getting sufficient contrast from light element such as carbon.

Electron beam damage

The quality of information obtained by newly developed TEM and STEM instruments is predominantly limited by electron beam damage of the specimens, rather than by the capability of the instrument. This issue is particularly challenging in the study of beam sensitive organic molecules and their assemblies. Two basic mechanisms of scattering of electrons by atoms, elastic and inelastic scattering (Figure 7), causes distinct formation of electron beam damage of specimen

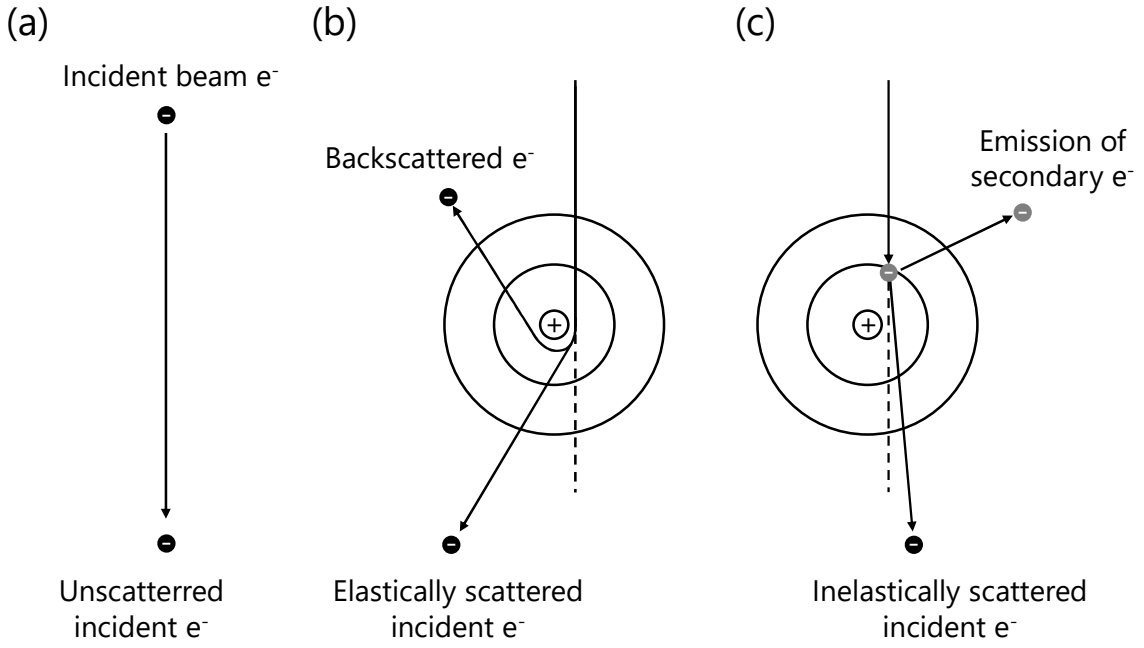

Figure 7. Interaction between the incident beam electron and atoms in specimen. (a) unscattered, (b) elastically scattered, and (c) inelastically scattered electrons.

Elastic scattering implies electrostatic interaction between the primary electrons of incident beam and atomic nuclei of the specimen (Figure 7b) with the conservation of the total kinetic energy. A small fraction of the incident electrons pass close enough to an atomic nucleus to be scattered through large angles and suffer appreciable energy loss causing knock-on or displacement damage. Knock-on damage is avoidable if the kinetic energy of incident electrons is reduced by decrease the acceleration voltage below certain threshold value in principle.[67] Inelastic scattering-the transfer of energy from the incident electron to the electrons in the specimen is another scattering mechanism which causes more complicated damage process proceeding simultaneously (Figure 7c). Inelastic scattering includes many distinct physical events including direct ionization (radiolysis), individual electronic excitations and collective plasmon/phonon excitations, which give

rise to secondary/Auger electrons, X-rays, cathodoluminescence, and heat.[67–69]

Radiolysis (ionization) is typical electron beam damage mechanism arise from the inelastic scattering of electrons, which suffer energy losses between a few eV (for excitation of conduction or valence electrons) and tens or hundreds of eV (for ionization of inner atomic shells). In a conducting specimen such as a metal, this energy transfer leaves a vacancy (hole) in the initial state (e.g. conduction band) but this vacancy is rapidly filled by one of the many electrons in the system before atoms can become displaced, and the material does not undergo ionization damage. In the case of insulators and some semi-conductors, however, holes created in the valence band or in the inner atomic shell last long enough for the excited atom to move, resulting in the permanent breakage of chemical bonds and a change in the atomic or molecular structure. In case of TEM, radiolysis cross sections are of the order of kbarn or Mbarn whereas knock-on displacement cross sections are of the order of 100 b (1 b = 10^{-28} m^2). Although knock-on displacement (particularly of hydrogen atoms) occurs in organic materials, radiolysis creates nearly all of the damage.[70] Hence, the insulating materials (oxides and organics) is easily damaged during observation by S/TEM. Note that the efficiency of radiolysis is increased due to the chain generation of secondary electrons created by inelastic scattering. Furthermore, as a result of the escape of secondary electrons, a poorly conducting TEM specimen would be expected to charge positively within the electron beam. This charge can cause image drift or distortion, structural change or mass transport arising from the drift of ions in the resulting electric field, or even complete destruction of the specimen due to electrostatic forces.[69,71,72] The inelastic scattering also causes heating of the specimen. The amount of energy imparted to the specimen critically depends on the electron dose or dose rate, which are defined as the number of incident

electrons per unit area of the specimen and the number of incident electrons per unit area per unit time, respectively.

Although electron beam damage has been typically suppressed using low acceleration voltages or low electron-dose conditions,[67,68,73–78] the modern methods for stable direct imaging of beam sensitive materials including oxides and organics is reducing the dimension of the specimen (from 3D to 2D or 1D).[65,79] Radiolysis damage is accelerated by secondary electrons produced by inelastic scattering, and the possibility of secondary electrons escaping from the sample surface into the vacuum depends on their depth from the surface.[80] Therefore, if the sample is an atomically thin film or small particulate matter, the beam sensitivity decreases as the secondary electrons excited from near-surface atoms escape from the specimen to vacuum without causing damage.[67,69,79] The ultimate idea of electron damage suppression by lowering the dimensionality is the isolation of individual organic molecules, which has been a key role for the stable TEM and STEM observations of individual organic molecules during the last two decades. The much smaller secondary electron scattering cross-sections of these isolated single molecules result in less damage. [65,66,81]

Fixation of molecules during observation

To realize the idea for direct imaging of the individual molecules by S/TEM, macroscopic supporting are required for stable fixation and isolation of the target molecules during observation, as they prevent dropout, migration, and aggregation. The supporting material and target molecule should be distinguishable with a large contrast, where nanocarbon materials (e.g., graphene, carbon nanotubes, and fullerene) are the most commonly used supporting substrate.[65,66,82] Several methods have been developed

for the fixation of molecules to nanocarbon substrates, including encapsulation into graphene layers, carbon nanotubes, or fullerene,[65,66,79,83–85]direct attachment via covalent bonding,[86] and weak adsorption via non-covalent interactions (e.g., van der Waals or π-π interactions) as shown in the next paragraph.[79,83,87,88]

Sufficient contrast from light element such as carbon

The organic molecules constructed of light elements have very low contrast in electron microscopy due to small scattering cross sections, which make single-molecule imaging more difficult. This problem was improved by the nanocarbon supporting materials which do not interfere with imaging owing to their single-atom-thick monolayer nature as well as the ability to molecule fixation. Aberration corrected TEM have been used to visualize an entire molecular framework on nanocarbon substrates. [65,81] The advantage of TEM is very short acquisition time and atomic resolution allowing us to interpret the reaction kinetics of the molecules during the observation, but generally faces the challenge of obtaining sufficient contrast from small carbon molecules against the supporting substrate. Since 2007, Nakamura et al. have pioneered the method to obtain movies of a variety of single organic molecules, organometallic molecules, and their assemblies, which are rotating, stretching, and reacting by single-molecule atomic-resolution real-time (SMART) TEM equipment with spherical aberration corrector.[65,81] The time resolution of SMART-TEM has been reached to sub-millisecond with the spatial resolution of sub-angstrom scale.[89] Encapsulation into CNT has been used to capture the molecules of my interest in solution and bring them into the nanoscale viewing field of TEM (Figure 8).

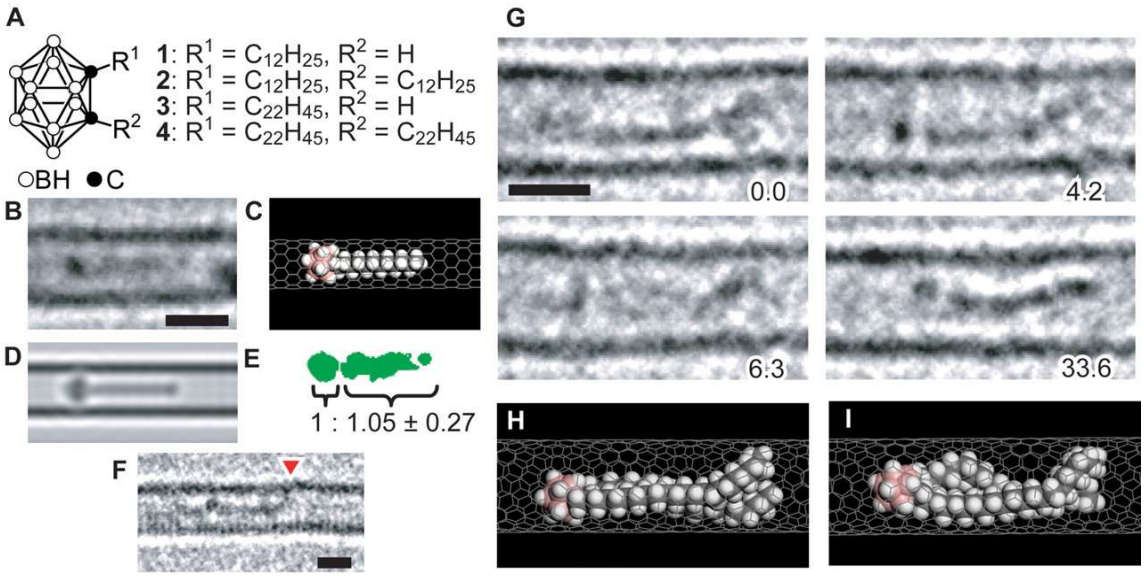

Figure 8. (A) Molecules 1 to 4. (B) TEM image of 1 in a CNT. Scale bars indicate 1 nm. (C and D) Model of 1 in CNT and simulation of its micrograph. Hydrogen, white; boron, pink; and carbon, gray. (E) Molecular image and digitized image contrast ratio of 1 obtained by subtracting the background contrast from (B). (F) TEM image of 2 sticking to a tube defect indicated by a red arrow (movie S3). (G) Experimental images of the intertwined hydrocarbon chains of 4 at consecutive times in seconds. (H and I) Models of 4 at 4.2 s and 6.3 s, respectively.[81]

Further development of the use of SMART-TEM was driven by "covalent fishing" where fish (organic molecules) in solution can be captured on a single-walled carbon nanotube (CNT) and tapered variant such as carbon nanohorn (CNH) serving as a "fishing rod." The amine groups on amino CNH, serve as a typical chemical fishhook (Figure 9).[86,90,91] Nakamura et al. demonstrated that the target molecule can be fixed to amino CNH using standard amide forming reactions, which allows to deal with molecules of any size attach to the CNT surface while encapsulation into CNT has size limitation intrinsically. The individual organic molecules in a vacuum did not decomposes rapidly

during TEM observation while the typical organic solids do. In organic solid, electrons hit numerous atoms to activate molecules (cation or in excited states) and to heat the solid. This causes dislocation of molecules in crystals, chemical reaction among neighboring molecules, and, importantly, generation of slow secondary electrons that destroy the molecule even more effectively. In vacuum where molecules are far apart, e-beam does not cause such chain events. Electrons may occasionally hit some atoms right in the center of their nuclei, but the cross section of collision and ionization at the high acceleration voltage is extremely small, and such events occur probabilistically, apparently not disturbing the SMART-TEM observation of the molecules. Textbooks of mass spectroscopy tell that ionization and destruction of organic molecules occur very rarely even by the use of slow e-beam optimized for this purpose (e.g., 70 V transferring average 15 eV (346 kcal) energy to a molecule).

Kaiser et al. have also demonstrated the direct imaging of individual molecule and their reaction processes by the TEM equipment with chromatic aberration (Cs) and spherical aberration (Cs) corrector in the project of sub-angstrom low-voltage electron microscopy (SALVE).[77] Encapsulation in CNT is mostly used fixation method owing to their restriction of the dynamics freedom of molecules (Figure 10). In addition to the spatial fixation, encapsulation in graphene derivates, such as CNT can moderate the electron beam damage since highly conductive CNT can act as sinks to alleviate the build-up of heat and charge, as well as the cage effect to increase the recombination probability.[79] Note that simply physisorbed molecules on graphene exhibit a low barrier for migration that allows for significant molecular motions on a shorter time scale than image capture (Figure 11).[4,5,66,92]

As represented by above studies, TEM provide the atomic-scale observations owing to nanocarbon supports with its simple structure, which reduce the disadvantage of the low contrast of light elements in the TEM. This method is, however, inconvenient for single molecule imaging on thicker supporting materials such as MoS_2, titania, and clay mineral nanosheet due to complicated contrast.

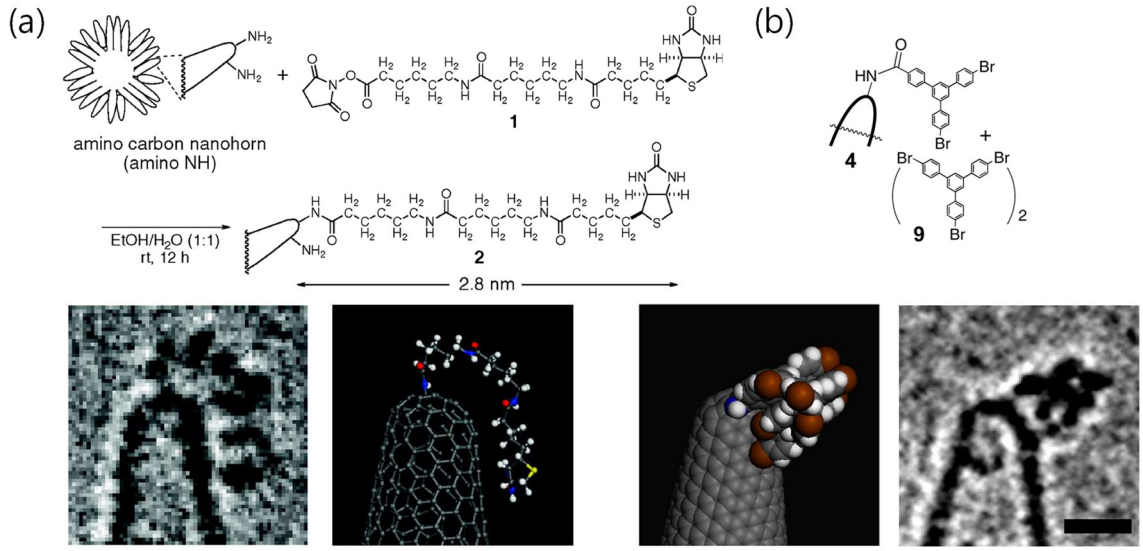

Figure 9. (a) Attachment of biotinylated diamine molecule to amino carbon nanohorn to form conjugate,[86] (b) A van der Waals cluster of two molecules of 9 attached to amino carbon nanohorn. structural formula, 3-D model, and one frame of the movie. Scale bar 1 nm.[90]

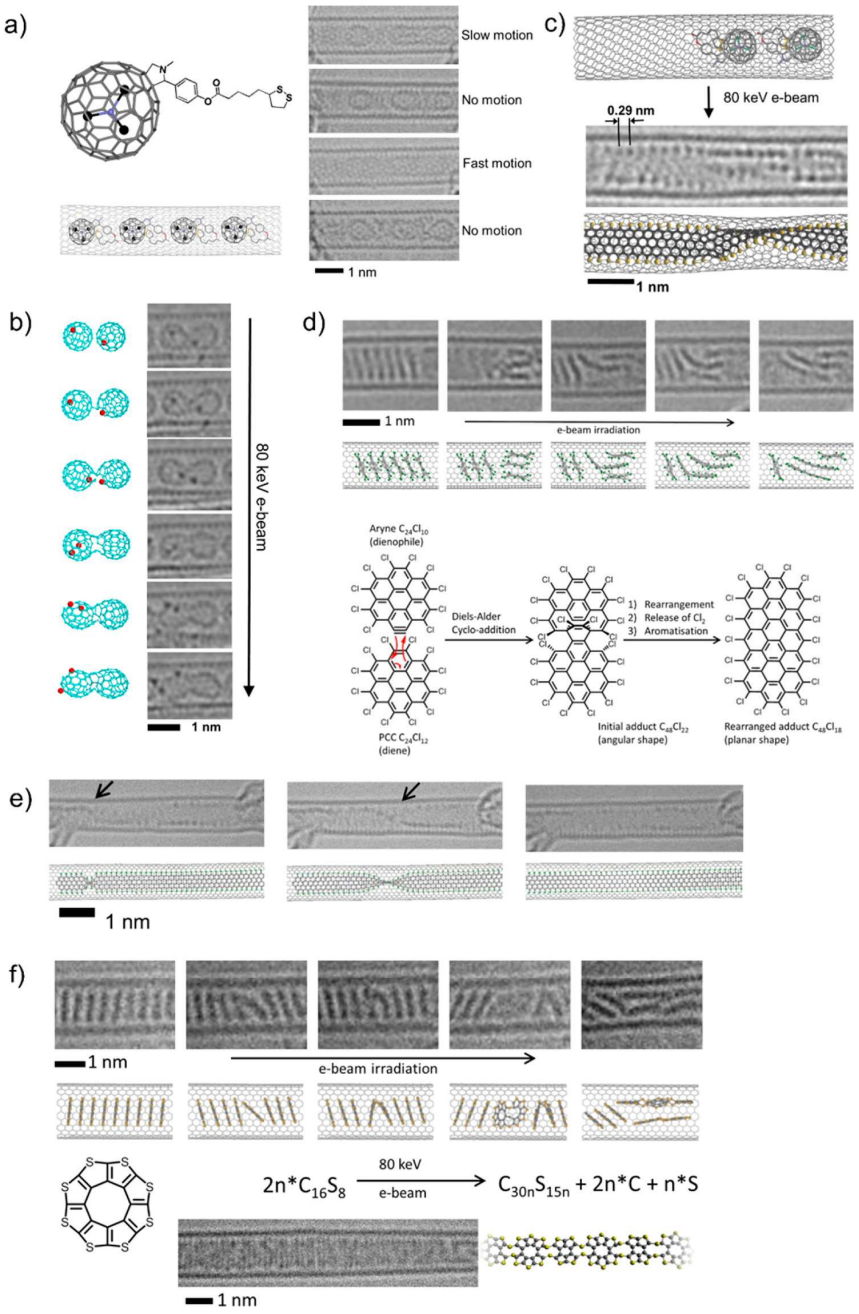

Figure 10. (a) Restricted motion of molecules in nanotubes allows accurate analysis of their structures when the molecules are stationary. (b) The 80 keV e-beam activates bonds of Dy@C82 fullerene, (c) thioctic ester fullerene, (d) perchlorocoronene and (f) octathiacirculene, transforming them into new products, such as sulfur or chlorine terminated graphene nanoribbons (e) (black arrows indicate points of twists in the nanoribbon).[66]

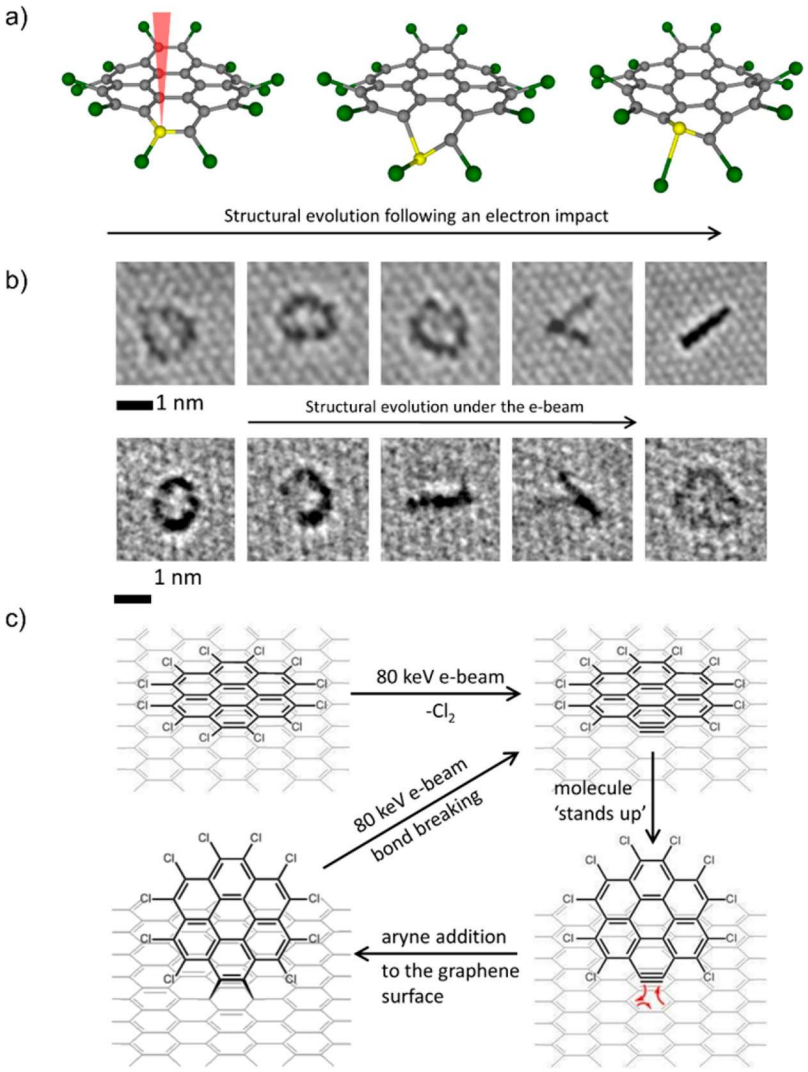

Figure 11. (a) Perchlorocoronene on graphene undergoes C–Cl bond dissociation due to impact of the 80 keV e-beam, (b, c) leading to the formation of aryne species that react with the graphene substrate, thus changing the orientation of the molecule from face-on to edge-on.[66]

Direct imaging of individual molecules by high-angle ADF−STEM has been also developed using heavy metal atom markers (e.g., Pt,[88,93] Cu,[82] Ru,[94] and W[95]) coordinated within the molecule. The fraction of high-angle scattered electrons approach "Rutherford scattering" and gives rise to "Z-contrast" proportional to the 1.4-1.7th power of the atomic number Z.[96–98] The heavy metal atom markers, therefore, exhibit bright contrast in ADF-STEM, which allows for visualization of single molecules on a host material with a more complex structure as well as graphene analogs with a single atom thickness. The ambition to use metal atom markers for ADF-STEM studies of molecules dates back to beyond 30 years ago, with work on using iridium clusters.[99] To date, the combination of ADF-STEM with graphene supports has been successful in tracking contrast from heavy Pt metal atoms in azobenzene photoswitching molecules (Figure 12A),[88] epitaxial assemblies of Pt-porphyrin hexamers (Figure 12B),[100] and Gd-based metallofullerene fusion dynamics on graphene.[84] Noteworthy, the popularity of nanocarbon supports and ADF−STEM imaging with heavy metal markers has led to the investigation of individual molecules on more complicated nanosheet than nanocarbons with a thickness of a few atoms and a periodical structure, including titania nanosheets (Figure 13A)[94] and MoS_2 (Figure 13B).[93]

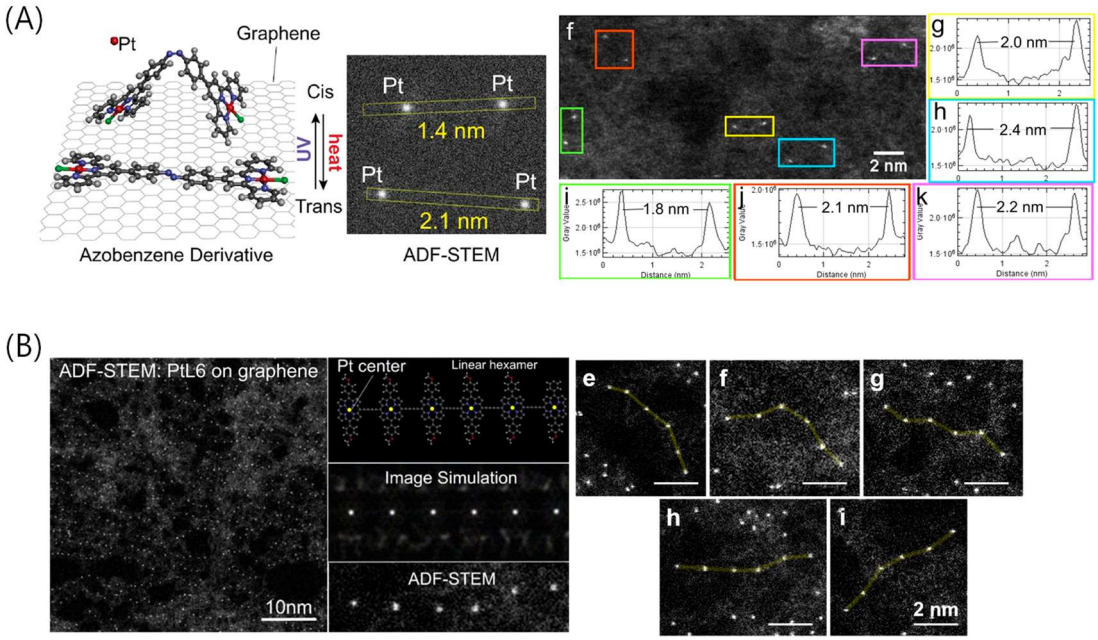

Figure 12. (A) Top view of atomic models of azobenzene molecule in *cis*- and *trans*-isomeric states on a monolayer graphene substrate, multislice HAADF image simulation based on the atomic model in (a) showing high contrast from the heavy Pt atoms in the molecules, and experimental HAADF images.[88] (B) ADF-STEM images, atomic model, and multislice HAADF image of Pt-porphyrin hexamers dispersed on graphene surface.[100]

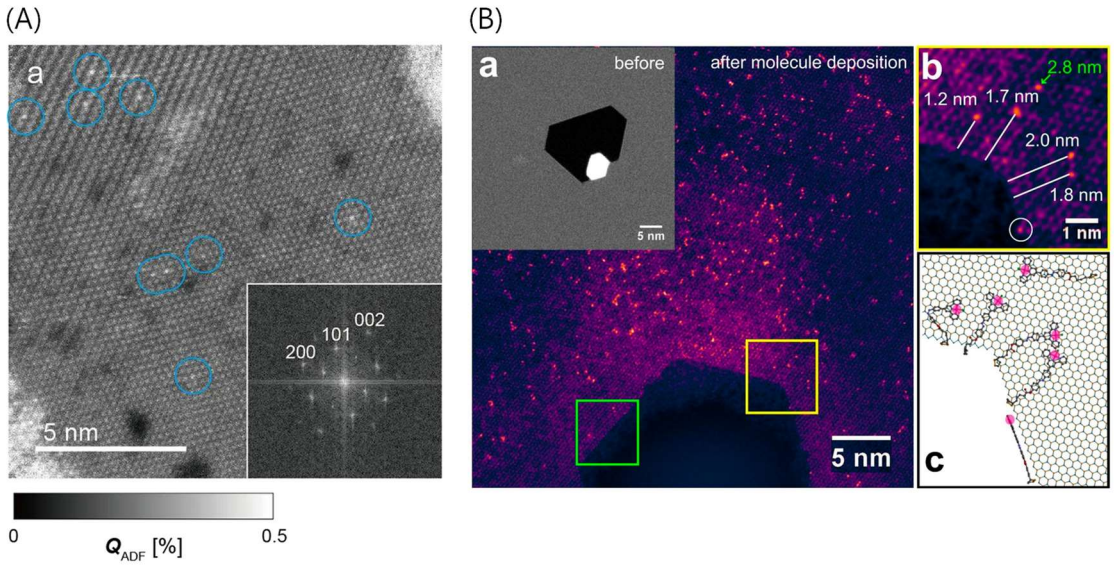

Figure 13. (A) Experimental ADF image of dye molecules attached on a titania nanosheet. The insets show the Fourier transform patterns,[94] (B) (a) ADF-STEM image of Pt-marked molecules deposited on a nanoporous MoS2 monolayer. (Inset) Nanoporous MoS2 monolayer before molecule deposition. (b) Magnified image of the area defined in the yellow box in (a). The distance between each Pt atom and the nearest Mo edge atom is shown. The green arrow points at a Pt atom 2.8 nm away from the nearest Mo edge, indicating that the molecule is not bound to the edge. The white circle shows a Pt atom found on the edge of a pore. (c) Atomic model of six Pt-marked molecules deposited near a nanopore, describing plausible configurations of molecules in (b).[93]

1.5 S/TEM imaging of bulk clay minerals and their nanosheets

The results of S/TEM observations of the individual molecules are interpreted based on the detailed observation of the support materials themselves with the periodic contrasts. The material science of clay nanosheet is, however, a relatively new topic and STEM imaging of a free-standing clay nanosheet, which doesn't contain any supports such as surfactants or polymer matrices, at an atomic resolution along the plane direction has not been achieved in spite of many reports on the few-atom-thick graphene analogs.[6,48,52,64,101–108] In the fields of mineralogy, Kogure et al. reported excellent works on cross-sectional imaging of bulk (stacked) clay minerals using high-resolution (HR) TEM and HAADF−STEM to reveal the layer stacking or distribution of the interlayer cations (Figure 14).[109–114] S/TEM observations of bulk clay minerals at the atomic scale from a cross-sectional direction have been conducted to visualize the atomic columns despite the electron beam damage of the specimen. Although S/TEM successfully visualized the atomic column of bulk clay minerals, the uses of S/TEM was limited to cross-sectional imaging and suffered from electron beam damage. Considering the effect of reducing the thickness of insulating materials on reduction of damage derived from inelastically scattered electrons, completely exfoliated clay mineral nanosheets with very low thickness (*ca.* 1 nm) may be more stable to electron beams irradiation than bulk minerals. Stable electron microscopy of monolayer clay mineral nanosheets will not only provide insights into single-molecule observations, but will also lead to solutions to problems in the field of clay mineralogy, such as determination of the actual distribution of isomorphous substituted cations and tracing of structural changes due to heat treatment.[111,112,115]

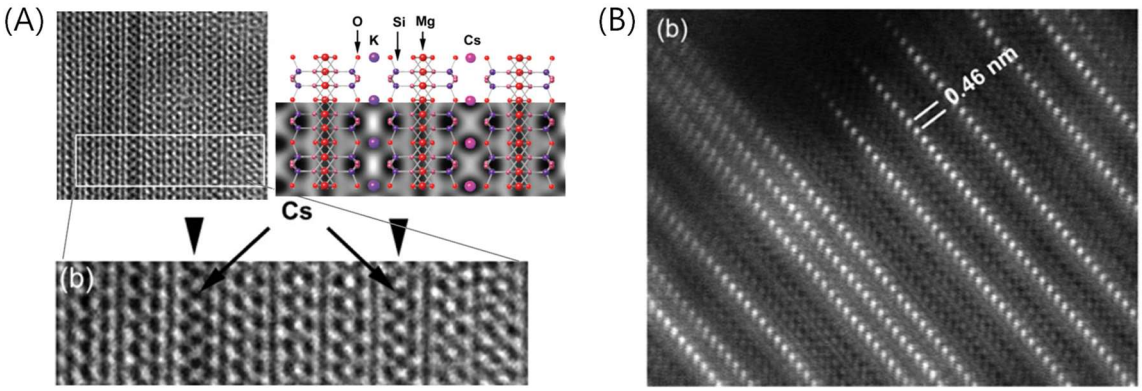

Figure 14. (A) Atomic arrangement, multislice simulation, and HRTEM images of the phlogopite super-cell in which K- and Cs-occupied interlayers alternate, viewed down [100]. (B) Filtered high-magnification HAADF image near the edge. The bright spots are Cs columns in the interlayer regions.[114]

1.6 Purpose of this thesis

Clay mineral nanosheets are two-dimensional nanosheets with a thickness of *ca.* 1 nm and a particle size of tens to hundreds of nm, which have unique surface-specific physicochemical properties such as large specific surface areas, atomically smooth surfaces, and surface charges derived from isomorphic substitutions. Owing to these properties, anionic charged clay nanosheets have been used as a host material to build a supramolecular assembly of organic molecules via electrostatic interactions. The structure and function of the dye-clay complexes, as well as the adsorption density of molecules within the structure and their association and aggregation, have been interpreted by spectroscopic measurements. However, the information obtained from spectroscopic measurements is an average of a vast number of molecules. The aim is to obtain the local structural information of dye-clay assemblies via electron microscopy, which can be complemented with averaged information from spectroscopic analysis to correlate the structural characteristics and properties or functionalities of individual molecular species during characterization.

Recent developments in electron microscopy and novel techniques for the precise control of low-dimensional substrate materials have led to the emergence of direct imaging of organic molecules. In the context of those prior studies, I concluded that the direct imaging of individual molecules in organic molecules-clay nanosheet assemblies is possible, considered from three points of view: (i) electron beam damage, (ii) effective fixation of molecules during observation, and (iii) getting sufficient contrast from light element (Figure 15). First, electron damage may be suppressed and stable electron microscopy is possible in organic molecule-clay nanosheet assemblies due to the small

	Prior researches in S/TEM observation of individual molecules	Organic molecules-clay mineral nanosheet assemblies
(i) Suppression of electron beam damage	• Low acceleration voltage • Low electron dose • **Low dimensional specimen** • **Isolated molecules**	• Thinness of clay nanosheet (ca. 1nm) • Isolation and fixation via multivalent electrostatic interaction
(ii) Effective fixation of molecules	• Encapsulation • Covalent bond • **Non-covalent interaction**	
(iii) Sufficient contrast form light elements	• Nanocarbons imparting easy contrast distinction • Heavy atoms working as marker in ADF–STEM	• Lack of knowledge of atomic resolution observations of clay mineral nanosheets • Extensive variety of metalloporphyrin

Figure 15. Summary of the points for realization of the direct imaging of individual molecules in organic molecule-clay mineral nanosheet assemblies via multivalent electrostatic interaction using S/TEM.

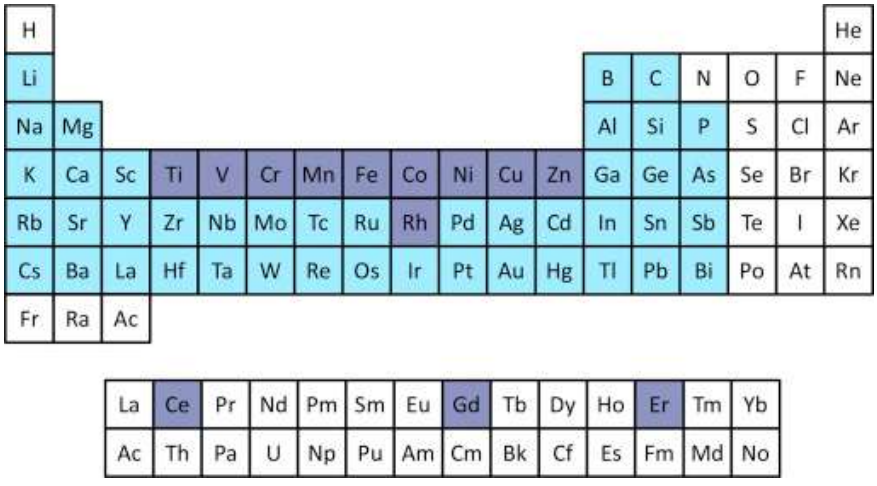

Figure 16. The elements that form complexes with porphyrins and related macrocycles are shown in light blue. In dark blue, the elements that have been reported to metalation of empty porphyrins or phthalocyanines on solid substrates.[116]

thickness of monolayer clay mineral nanosheet and non-aggregated adsorption of molecules on clay surface. Note that in previous reports multivalent molecules strongly adsorb on the clay mineral nanosheet surface, and do not desorb or make aggregation in the aqueous solutions[42,117] and even in the solid state as membrane films.[118,119] Second, multivalent electrostatic interactions, which is stronger than simple physical adsorption on graphene via van der Waals and π-π interactions, inhibit the desorption, aggregation, and intermolecular reactions during observation. Hence, multivalent electrostatic interaction are expected to provide isolation and fixation effects of the molecules during the S/TEM observation. Third, direct imaging of individual molecules on clay nanosheet would be realized by ADF−STEM imaging of heavy metal markers despite relatively thicker structure (ca. 1nm) of clay mineral nanosheets than graphene analogues. This observation method is also driven by the fact that porphyrins form coordination bonds with a variety of metal atoms (Figure 16).[116]

In this thesis, I demonstrated direct imaging of the supramolecular assemblies of well-isolated organic molecules based on multivalent electrostatic interactions, where anionically charged clay mineral nanosheets were used as a host material. Based on the my first direct imaging of clay mineral nanosheet at the atomic scale, the individual organic molecules and supramolecular assemblies on the monolayer clay mineral nanosheets was visualized successfully via annular dark field scanning transmission electron microscopy using heavy metal atom markers. The versatility of multivalent electrostatic interactions for the stable fixation of organic molecules during electron microscopic imaging was demonstrated. This strategy can be applied to a wide range of supramolecular systems comprising various guest molecules and host materials, thereby

broadening the scope of atomic-scale imaging. The combination of fixation and isolation by multivalent electrostatic interactions in this system will not only reveal individual structures, but may also be applied to an energetic understanding of non-covalent interactions.

1.7 Outline of this thesis

This thesis consists of seven chapters. The key contents of each chapter are outlined as follows.

Chapter 1 summarizes the general background including supramolecular assemblies via non-covalent interactions, supramolecular assemblies by multivalent electrostatic interactions using clay mineral nanosheets, and direct imaging of individual molecules in the assemblies by aberration-corrected electron microscopy. The objective and outline of the thesis were provided.

Chapter 2 presents the determination of the layer number of clay mineral nanosheets deposited on a carbon grid from a single layer to four, based on the difference in ADF contrast.

Chapter 3 shows a stable imaging of free-standing (without any surfactants or matrices) monolayer clay mineral by ADF−STEM at the atomic-scale.

Chapter 4 demonstrates that the monolayer clay mineral exhibited the outstanding stability under electron beam irradiation compared to two- or three-layered nanosheets via electron diffraction analysis.

Chapter 5 presents a direct imaging of the single organic molecules and supra-molecular assemblies on the monolayer clay mineral nanosheets was demonstrated via ADF−STEM

using heavy metal atom markers.

Chapter 6 presents the candidates marker atoms other than platinum and shows for the possibility to discriminate between two types of molecules containing markers with different atomic numbers from ADF-STEM contrast for the first time.

Chapter 7 presents the summary and perspectives are summarized in the last part.

1.8 References

(1) Lehn, J. M. Cryptates: Inclusion Complexes of Macropolycyclic Receptor Molecules. *Pure Appl. Chem.* **1978**, *50*, 871–892.

(2) Lehn, J. M. Supramolecular Chemistry - Scope and Perspectives Molecules, Supermolecules, and Molecular Devices. *Angew. Chem. Int. Ed.* **1988**, *27*, 89–112.

(3) Biedermann, F.; Schneider, H. J. Experimental Binding Energies in Supramolecular Complexes. *Chem. Rev.* **2016**, *116*, 5216–5300.

(4) Georgakilas, V.; Tiwari, J. N.; Kemp, K. C.; Perman, J. A.; Bourlinos, A. B.; Kim, K. S.; Zboril, R. Noncovalent Functionalization of Graphene and Graphene Oxide for Energy Materials, Biosensing, Catalytic, and Biomedical Applications. *Chem. Rev.* **2016**, *116*, 5464–5519.

(5) Daukiya, L.; Seibel, J.; De Feyter, S. Chemical Modification of 2D Materials Using Molecules and Assemblies of Molecules. *Adv. Phys. X* **2019**, *4*, 1625723.

(6) Tan, C.; Cao, X.; Wu, X. J.; He, Q.; Yang, J.; Zhang, X.; Chen, J.; Zhao, W.; Han, S.; Nam, G. H.; et al. Recent Advances in Ultrathin Two-Dimensional Nanomaterials. *Chem. Rev.* **2017**, *117*, 6225–6331.

(7) Mas-Ballesté, R.; Gómez-Navarro, C.; Gómez-Herrero, J.; Zamora, F. 2D Materials: To Graphene and Beyond. *Nanoscale* **2011**, *3*, 20–30.

(8) Hirsch, A.; Hauke, F. Post-Graphene 2D Chemistry: The Emerging Field of Molybdenum Disulfide and Black Phosphorus Functionalization. *Angew. Chem. Int. Ed.* **2018**, *57*, 4338–4354.

(9) Novoselov, K. S.; Geim, A. K.; Morozov, S. V.; Jiang, D.; Zhang, Y.; Dubonos, S. V.; Grigorieva, I. V.; Firsov, A. A. Electric Field in Atomically Thin Carbon Films. *Science* **2004**, *306*, 666–669.

(10) Geim, A. K.; Novoselov, K. S. The Rise of Graphene. *Nat. Mater.* **2007**, *6*, 183–191.

(11) Bhimanapati, G. R.; Lin, Z.; Meunier, V.; Jung, Y.; Cha, J.; Das, S.; Xiao, D.; Son, Y.; Strano, M. S.; Cooper, V. R.; et al. Recent Advances in Two-Dimensional Materials beyond Graphene. **2015**, *9*, 11509–11539.

(12) Zhang, H.; Cheng, H. M.; Ye, P. 2D Nanomaterials: Beyond Graphene and Transition Metal Dichalcogenides. *Chem. Soc. Rev.* **2018**, *47*, 6009–6012.

(13) Lin, Y.; Williams, T. V; Connell, J. W. Soluble, Exfoliated Hexagonal Boron Nitride Nanosheets. *J. Phys. Chem. Lett* **2010**, *1*, 277–283.

(14) Zheng, Z.; Cox, M. C.; Li, B. Surface Modification of Hexagonal Boron Nitride Nanomaterials: A Review. *J. Mater. Sci.* **2018**, *53*, 66–99.

(15) Lv, R.; Robinson, J. A.; Schaak, R. E.; Sun, D.; Sun, Y.; Mallouk, T. E.; Terrones, M. Transition Metal Dichalcogenides and beyond: Synthesis, Properties, and Applications of Single- and Few-Layer Nanosheets. *Acc. Chem. Res.* **2015**, *48*, 56–64.

(16) Zhang, J.; Chen, Y.; Wang, X. Two-Dimensional Covalent Carbon Nitride Nanosheets: Synthesis, Functionalization, and Applications. *Energy Environ. Sci.* **2015**, *8*, 3092–3108.

(17) Ong, W. J.; Tan, L. L.; Ng, Y. H.; Yong, S. T.; Chai, S. P. Graphitic Carbon Nitride (g-C_3N_4)-Based Photocatalysts for Artificial Photosynthesis and Environmental Remediation: Are We a Step Closer to Achieving Sustainability? *Chem. Rev.* **2016**, *116*, 7159–7329.
(18) Ma, R.; Sasaki, T. Two-Dimensional Oxide and Hydroxide Nanosheets: Controllable High-Quality Exfoliation, Molecular Assembly, and Exploration of Functionality. *Acc. Chem. Res.* **2015**, *48*, 136–143.
(19) Timmerman, M. A.; Xia, R.; Le, P. T. P.; Wang, Y.; Elshof, J. E. Metal Oxide Nanosheets as 2D Building Blocks for the Design of Novel Materials. *Chem. Eur. J.* **2020**, *26*, 9084–9098.
(20) Yu, J.; Wang, Q.; O'Hare, D.; Sun, L. Preparation of Two Dimensional Layered Double Hydroxide Nanosheets and Their Applications. *Chem. Soc. Rev.* **2017**, *46*, 5950–5974.
(21) Hantanasirisakul, K.; Gogotsi, Y. Electronic and Optical Properties of 2D Transition Metal Carbides and Nitrides (MXenes). *Adv. Mater.* **2018**, *30*, 1804779.
(22) Hemanth, N. R.; Kandasubramanian, B. Recent Advances in 2D MXenes for Enhanced Cation Intercalation in Energy Harvesting Applications: A Review. *Chem. Eng. J.* **2020**, *392*, 123678.
(23) Peng, Y.; Li, Y.; Ban, Y.; Jin, H.; Jiao, W.; Liu, X.; Yang, W. Metal- Organic Framework Nanosheets as Building Blocks for Molecular Sieving Membranes. *Science* **2014**, *346*, 1356–1359.
(24) Zhao, M.; Huang, Y.; Peng, Y.; Huang, Z.; Ma, Q.; Zhang, H. Two-Dimensional Metal-Organic Framework Nanosheets: Synthesis and Applications. *Chem. Soc. Rev.* **2018**, *47*, 6267–6295.
(25) Wang, H.; Zeng, Z.; Xu, P.; Li, L.; Zeng, G.; Xiao, R.; Tang, Z.; Huang, D.; Tang, L.; Lai, C.; et al. Recent Progress in Covalent Organic Framework Thin Films: Fabrications, Applications and Perspectives. *Chem. Soc. Rev.* **2019**, *48*, 488–516.
(26) Hu, J.; Gupta, S. K.; Ozdemir, J.; Beyzavi, M. H. Applications of Dynamic Covalent Chemistry Concept toward Tailored Covalent Organic Framework Nanomaterials: A Review. *Appl. Nano Mater.* **2020**, *3*, 6239–6269.
(27) Vogt, P.; De Padova, P.; Quaresima, C.; Avila, J.; Frantzeskakis, E.; Asensio, M. C.; Resta, A.; Ealet, B.; Le Lay, G. Silicene: Compelling Experimental Evidence for Graphenelike Two-Dimensional Silicon. *Phys. Rev. Lett.* **2012**, *108*, 155501.
(28) Molle, A.; Grazianetti, C.; Tao, L.; Taneja, D.; Alam, M. H.; Akinwande, D. Silicene, Silicene Derivatives, and Their Device Applications. *Chem. Soc. Rev* **2018**, *47*, 6370–6387.
(29) Peng, L.; Ye, S.; Song, J.; Qu, J. Solution-Phase Synthesis of Few-Layer Hexagonal Antimonene Nanosheets via Anisotropic Growth. *Angew. Chem. Int. Ed.* **2019**, *58*, 9891–9896.
(30) Kuriakose, S.; Jain, S. K.; Tawfik, S. A.; Spencer, M. J. S.; Murdoch, B. J.; Singh, M.; Rahman, F.; Mayes, E. L. H.; Taha, M. Y.; Ako, R. T.; et al. Monocrystalline Antimonene Nanosheets via Physical Vapor Deposition. *Adv. Mater. Interfaces* **2020**, 2001678.
(31) Ares, P.; Aguilar-Galindo, F.; Rodríguez-San-Miguel, D.; Aldave, D. A.; Díaz-Tendero, S.; Alcamí, M.; Martín, F.; Gómez-Herrero, J.; Zamora, F. Mechanical Isolation of Highly Stable Antimonene under Ambient Conditions. *Adv. Mater.* **2016**, *28*, 6332–6336.

(32) Osada, M.; Sasaki, T. Two-Dimensional Dielectric Nanosheets: Novel Nanoelectronics from Nanocrystal Building Blocks. *Adv. Mater.* **2012**, *24*, 210–228.
(33) Zheng, J. Y.; Manning, H. G.; Zhang, Y.; Wang, J. J.; Purcell-Milton, F.; Pokle, A.; Porter, S. B.; Zhong, C.; Li, J.; O'Reilly Meehan, R.; et al. Synthesis of Centimeter-Size Free-Standing Perovskite Nanosheets from Single-Crystal Lead Bromide for Optoelectronic Devices. *Sci. Rep.* **2019**, *9*, 11738.
(34) Dou, L.; Wong, A. B.; Yu, Y.; Lai, M.; Kornienko, N.; Eaton, S. W.; Fu, A.; Bischak, C. G.; Ma, J.; Ding, T.; et al. Atomically Thin Two-Dimensional Organic-Inorganic Hybrid Perovskites. *Science* **2015**, *349*, 1518–1521.
(35) Fiori, G.; Bonaccorso, F.; Iannaccone, G.; Palacios, T.; Neumaier, D.; Seabaugh, A.; Banerjee, S. K.; Colombo, L. Electronics Based on Two-Dimensional Materials. *Nat. Nanotechnol.* **2014**, *9*, 768–779.
(36) Bonaccorso, F.; Colombo, L.; Yu, G.; Stoller, M.; Tozzini, V.; Ferrari, A. C.; Ruoff, R. S.; Pellegrini, V. Graphene, Related Two-Dimensional Crystals, and Hybrid Systems for Energy Conversion and Storage. *Science* **2015**, *347*, 1246501.
(37) Deng, D.; Novoselov, K. S.; Fu, Q.; Zheng, N.; Tian, Z.; Bao, X. Catalysis with Two-Dimensional Materials and Their Heterostructures. *Nat. Nanotechnol.* **2016**, *11*, 218–230.
(38) Guo, S.; Dong, S. Graphene Nanosheet: Synthesis, Molecular Engineering, Thin Film, Hybrids, and Energy and Analytical Applications. *Chem. Soc. Rev.* **2011**, *40*, 2644–2672.
(39) Dikin, D. A.; Stankovich, S.; Zimney, E. J.; Piner, R. D.; Dommett, G. H. B.; Evmenenko, G.; Nguyen, S. T.; Ruoff, R. S. Preparation and Characterization of Graphene Oxide Paper. *Nature* **2007**, *448*, 457–460.
(40) Mendoza-Sánchez, B.; Gogotsi, Y. Synthesis of Two-Dimensional Materials for Capacitive Energy Storage. *Adv. Mater.* **2016**, *28*, 6104–6135.
(41) Tan, C.; Liu, Z.; Huang, W.; Zhang, H. Non-Volatile Resistive Memory Devices Based on Solution-Processed Ultrathin Two-Dimensional Nanomaterials. *Chem. Soc. Rev.* **2015**, *44*, 2615–2628.
(42) Bujdák, J. Effect of the Layer Charge of Clay Minerals on Optical Properties of Organic Dyes. A Review. *Appl. Clay Sci.* **2006**, *34*, 58–73.
(43) Schoonheydt, R. A.; Johnston, C. T. The Surface Properties of Clay Minerals. In *Layered Mineral Structures and their Application in Advanced Technologies*; Brigatti, M. F., Mottana, A., Eds.; Mineralogical Society of Great Britain and Ireland, 2011; Vol. 11, pp 337–373.
(44) Bujdák, J. The Effects of Layered Nanoparticles and Their Properties on the Molecular Aggregation of Organic Dyes. *J. Photochem. Photobiol. C Photochem. Rev.* **2018**, *35*, 108–133.
(45) Shichi, T.; Takagi, K. Clay Minerals as Photochemical Reaction Fields. *J. Photochem. Photobiol. C Photochem. Rev.* **2000**, *1*, 113–130.
(46) Ishida, Y. Manipulation of Supramolecular 2D Assembly of Functional Dyes toward Artificial Light-Harvesting Systems. *Pure Appl. Chem.* **2015**, *87*, 3–14.
(47) Ishida, Y.; Akita, I.; Pons, T.; Yonezawa, T.; Hildebrandt, N. Real-Space Investigation of Energy Transfer through Electron Tomography. *J. Phys. Chem. C* **2017**, *121*, 28395−28402.

(48) Okada, T.; Ide, Y.; Ogawa, M. Organic-Inorganic Hybrids Based on Ultrathin Oxide Layers: Designed Nanostructures for Molecular Recognition. *Chem. Asian J.* **2012**, *7*, 1980–1992.
(49) Ishida, Y. Manipulation of Supramolecular 2D Assembly of Functional Dyes toward Artificial Light-Harvesting Systems. *Pure Appl. Chem.* **2015**, *87*, 3–14.
(50) Carniato, F.; Gatti, G.; Bisio, C. An Overview of the Recent Synthesis and Functionalization Methods of Saponite Clay. *New J. Chem.* **2020**, *44*, 9969–9980.
(51) Takagi, S.; Eguchi, M.; Tryk, D. A.; Inoue, H. Porphyrin Photochemistry in Inorganic/Organic Hybrid Materials: Clays, Layered Semiconductors, Nanotubes, and Mesoporous Materials. *J. Photochem. Photobiol. C Photochem. Rev.* **2006**, *7*, 104–126.
(52) López Arbeloa, F.; Martínez Martínez, V.; Arbeloa, T.; López Arbeloa, I. Photoresponse and Anisotropy of Rhodamine Dye Intercalated in Ordered Clay Layered Films. *J. Photochem. Photobiol. C Photochem. Rev.* **2007**, *8*, 85–108.
(53) Egawa, T.; Watanabe, H.; Fujimura, T.; Ishida, Y.; Yamato, M.; Masui, D.; Shimada, T.; Tachibana, H.; Yoshida, H.; Inoue, H.; et al. Novel Methodology to Control the Adsorption Structure of Cationic Porphyrins on the Clay Surface Using the "Size-Matching Rule." *Langmuir* **2011**, *27*, 10722–10729.
(54) Büchner, C.; Heyde, M. Two-Dimensional Silica Opens New Perspectives. *Prog. Surf. Sci.* **2017**, *92*, 341–374.
(55) Ishida, Y.; Masui, D.; Shimada, T.; Tachibana, H.; Inoue, H.; Takagi, S. The Mechanism of the Porphyrin Spectral Shift on Inorganic Nanosheets: The Molecular Flattening Induced by the Strong Host-Guest Interaction Due to the "Size-Matching Rule." *J. Phys. Chem. C* **2012**, *116*, 7879–7885.
(56) Eguchi, M.; Takagi, S.; Tachibana, H.; Inoue, H. The "size Matching Rule" in Di-, Tri-, and Tetra-Cationic Charged Porphyrin/Synthetic Clay Complexes: Effect of the Inter-Charge Distance and the Number of Charged Sites. *J. Phys. Chem. Solids* **2004**, *65*, 403–407.
(57) Baston, P. E.; Dellby, N.; Krivanek, O. L. Sub-Ångstrom Resolution Using Aberration Corrected Electron Optics. *J. Electron Microsc. (Tokyo).* **2002**, *418*, 617–620.
(58) Haider, M.; Rose, H.; Uhlemann, S.; Kabius, B.; Urban, K. Towards 0.1 Nm Resolution with the First Spherically Corrected Transmission Electron Microscope. *J. Electron Microsc. (Tokyo).* **1998**, *47*, 395–405.
(59) Pennycook, S. J. The Impact of STEM Aberration Correction on Materials Science. *Ultramicroscopy* **2017**, *180*, 22–33.
(60) Lin, Y. C.; Susi, T.; Kotakoski, J.; Ramasse, Q. M.; Kepaptsoglou, D.; Meyer, J. C.; Suenaga, K. Towards Atomically Precise Manipulation of 2D Nanostructures in the Electron Microscope. *2D Mater.* **2017**, *4*, 042004.
(61) Sohlberg, K.; Pennycook, T. J.; Zhou, W.; Pennycook, S. J. Insights into the Physical Chemistry of Materials from Advances in HAADF-STEM. *Phys. Chem. Chem. Phys.* **2015**, *17*, 3982–4006.
(62) Krivanek, O. L.; Chisholm, M. F.; Nicolosi, V.; Pennycook, T. J.; Corbin, G. J.; Dellby, N.; Murfitt, M. F.; Own, C. S.; Szilagyi, Z. S.; Oxley, M. P.; et al. Atom-by-Atom Structural and Chemical Analysis by Annular Dark-Field Electron Microscopy. *Nature* **2010**, *464*, 571–574.

(63) Chhowalla, M.; Shin, H. S.; Eda, G.; Li, L. J.; Loh, K. P.; Zhang, H. The Chemistry of Two-Dimensional Layered Transition Metal Dichalcogenide Nanosheets. *Nat. Chem.* **2013**, *5*, 263–275.
(64) Hashimoto, A.; Suenaga, K.; Gloter, A.; Urita, K.; Iijima, S. Direct Evidence for Atomic Defects in Graphene Layers. *Nature* **2004**, *430*, 870–873.
(65) Nakamura, E. Atomic-Resolution Transmission Electron Microscopic Movies for Study of Organic Molecules, Assemblies, and Reactions: The First 10 Years of Development. *Acc. Chem. Res.* **2017**, *50*, 1281–1292.
(66) Skowron, S. T.; Chamberlain, T. W.; Biskupek, J.; Kaiser, U.; Besley, E.; Khlobystov, A. N. Chemical Reactions of Molecules Promoted and Simultaneously Imaged by the Electron Beam in Transmission Electron Microscopy. *Acc. Chem. Res.* **2017**, *50*, 1797–1807.
(67) Egerton, R. F. Radiation Damage to Organic and Inorganic Specimens in the TEM. *Micron* **2019**, *119*, 72–87.
(68) Susi, T.; Meyer, J. C.; Kotakoski, J. Quantifying Transmission Electron Microscopy Irradiation Effects Using Two-Dimensional Materials. *Nat. Rev. Phys.* **2019**, *1*, 397–405.
(69) Jiang, N. Electron Beam Damage in Oxides: A Review. *Reports Prog. Phys.* **2015**, *79*, 016501.
(70) Egerton, R. F. Mechanisms of Radiation Damage in Beam-Sensitive Specimens, for TEM Accelerating Voltages between 10 and 300 KV. *Microsc. Res. Tech.* **2012**, *75*, 1550–1556.
(71) Cazaux, J. Mechanisms of Charging in Electron Spectroscopy. *J. Electron Spectros. Relat. Phenomena* **1999**, *105*, 155–185.
(72) Wei, X.; Tang, D. M.; Chen, Q.; Bando, Y.; Golberg, D. Local Coulomb Explosion of Boron Nitride Nanotubes under Electron Beam Irradiation. *ACS Nano* **2013**, *7*, 3491–3497.
(73) Liu, L.; Lopez-Haro, M.; Calvino, J. J.; Corma, A. Tutorial: Structural Characterization of Isolated Metal Atoms and Subnanometric Metal Clusters in Zeolites. *Nat. Protoc.* **2020**, DOI: 10.1038/s41596-020-0366-9.
(74) Chen, Q.; Dwyer, C.; Sheng, G.; Zhu, C.; Li, X.; Zheng, C.; Zhu, Y. Imaging Beam-Sensitive Materials by Electron Microscopy. *Adv. Mater.* **2020**, *32*, 1–42.
(75) Krivanek, O. L.; Dellby, N.; Murfitt, M. F.; Chisholm, M. F.; Pennycook, T. J.; Suenaga, K.; Nicolosi, V. Gentle STEM: ADF Imaging and EELS at Low Primary Energies. *Ultramicroscopy* **2010**, *110*, 935–945.
(76) Kramberger, C.; Meyer, J. C. Progress in Structure Recovery from Low Dose Exposures: Mixed Molecular Adsorption, Exploitation of Symmetry and Reconstruction from the Minimum Signal Level. *Ultramicroscopy* **2016**, *170*, 60–68.
(77) Linck, M.; Hartel, P.; Uhlemann, S.; Kahl, F.; Müller, H.; Zach, J.; Biskupek, J.; Niestadt, M.; Kaiser, U.; Haider, M. Performance of the SALVE-Microscope: Atomic-Resolution TEM Imaging at 20kV. *Microsc. Microanal.* **2019**, *2016*, 878–879.
(78) Sasaki, T.; Sawada, H.; Hosokawa, F.; Sato, Y.; Suenaga, K. Aberration-Corrected STEM/TEM Imaging at 15kV. *Ultramicroscopy* **2014**, *145*, 50–55.

(79) Skowron, S. T.; Roberts, S. L.; Khlobystov, A. N.; Besley, E. The Effects of Encapsulation on Damage to Molecules by Electron Radiation. *Micron* **2019**, *120*, 96–103.
(80) Seiler, H. Secondary Electron Emission in the Scanning Electron Microscope. *J. Appl. Phys.* **1983**, *54*, R1.
(81) Koshino, M.; Tanaka, T.; Solin, N.; Suenaga, K.; Isobe, H.; Nakamura, E. Imaging of Single Organic Molecules in Motion. *Science* **2007**, *316*, 853–853.
(82) Mittelberger, A.; Kramberger, C.; Meyer, J. C. Insights into Radiation Damage from Atomic Resolution Scanning Transmission Electron Microscopy Imaging of Mono-Layer $CuPcCl_{16}$ Films on Graphene. *Sci. Rep.* **2018**, *8*, 4813.
(83) Choe, J.; Lee, Y.; Park, J.; Kim, Y.; Kim, C. U.; Kim, K. Direct Imaging of Structural Disordering and Heterogeneous Dynamics of Fullerene Molecular Liquid. *Nat. Commun.* **2019**, *10*, 1–7.
(84) Sinha, S.; Sheng, Y.; Griffiths, I.; Young, N. P.; Zhou, S.; Kirkland, A. I.; Porfyrakis, K.; Warner, J. H. In Situ Atomic-Level Studies of Gd Atom Release and Migration on Graphene from a Metallofullerene Precursor. *ACS Nano* **2018**, *12*, 10439–10451.
(85) Cao, K.; Skowron, S. T.; Biskupek, J.; Stoppiello, C. T.; Leist, C.; Besley, E.; Khlobystov, A. N.; Kaiser, U. Imaging an Unsupported Metal–Metal Bond in Dirhenium Molecules at the Atomic Scale. *Sci. Adv.* **2020**, *6*, eaay5849.
(86) Nakamura, E.; Koshino, M.; Tanaka, T.; Niimi, Y.; Harano, K.; Nakamura, Y.; Isobe, H. Imaging of Conformational Changes of Biotinylated Triamide Molecules Covalently Bonded to a Carbon Nanotube Surface. *J. Am. Chem. Soc.* **2008**, *130*, 7808–7809.
(87) Markevich, A.; Kurasch, S.; Lehtinen, O.; Reimer, O.; Feng, X.; Müllen, K.; Turchanin, A.; Khlobystov, A. N.; Kaiser, U.; Besley, E. Electron Beam Controlled Covalent Attachment of Small Organic Molecules to Graphene. *Nanoscale* **2016**, *8*, 2711–2719.
(88) Gerkman, M. A.; Sinha, S.; Warner, J. H.; Han, G. G. D. Direct Imaging of Photoswitching Molecular Conformations Using Individual Metal Atom Markers. *ACS Nano* **2019**, *13*, 87–96.
(89) Shimizu, T.; Lungerich, D.; Stuckner, J.; Murayama, M.; Harano, K.; Nakamura, E. Real-Time Video Imaging of Mechanical Motions of a Single Molecular Shuttle with Sub-Millisecond Sub-Angstrom Precision. *Bull. Chem. Soc. Jpn.* **2020**, *93*, 1079–1085.
(90) Harano, K.; Homma, T.; Niimi, Y.; Koshino, M.; Suenaga, K.; Leibler, L.; Nakamura, E. Heterogeneous Nucleation of Organic Crystals Mediated by Single-Molecule Templates. *Nat. Mater.* **2012**, *11*, 877–881.
(91) Isobe, H.; Tanaka, T.; Maeda, R.; Noiri, E.; Solin, N.; Yudasaka, M.; Iijima, S.; Nakamura, E. Preparation, Purification, Characterization, and Cytotoxicity Assessment of Water-Soluble, Transition-Metal-Free Carbon Nanotube Aggregates. *Angew. Chem. Int. Ed.* **2006**, *45*, 6676–6680.
(92) Colliex, C.; Gloter, A.; March, K.; Mory, C.; Stéphan, O.; Suenaga, K.; Tencé, M. Capturing the Signature of Single Atoms with the Tiny Probe of a STEM. *Ultramicroscopy* **2012**, *123*, 80–89.

(93) Gerkman, M. A.; Lee, J. K.; Li, X.; Zhang, Q.; Windley, M.; Fonseca, M. V; Lu, Y.; Warner, J. H.; Han, G. G. D. Direct Imaging of Individual Molecular Binding to Clean Nanopore Edges in 2D Monolayer MoS_2. *ACS Nano* **2020**, *14*, 153–165.
(94) Koshiya, S.; Yamashita, S.; Kimoto, K. Microscopic Observation of Dye Molecules for Solar Cells on a Titania Surface. *Sci. Rep.* **2016**, *6*, 2–7.
(95) Kengmana, E. S.; Lee, J. K.; Li, X.; Warner, J. H.; Han, G. G. D. Self-Assembly of Bowlic Supramolecules on Graphene Imaged at the Individual Molecular Level Using Heavy Atom Tagging. *Small* **2020**, 2002860.
(96) Krivanek, O. L.; Chisholm, M. F.; Nicolosi, V.; Pennycook, T. J.; Corbin, G. J.; Dellby, N.; Murfitt, M. F.; Own, C. S.; Szilagyi, Z. S.; Oxley, M. P.; et al. Atom-by-Atom Structural and Chemical Analysis by Annular Dark-Field Electron Microscopy. *Nature* **2010**, *464*, 571–574.
(97) Yamashita, S.; Kikkawa, J.; Yanagisawa, K.; Nagai, T.; Ishizuka, K.; Kimoto, K. Atomic Number Dependence of Z Contrast in Scanning Transmission Electron Microscopy. *Sci. Rep.* **2018**, *8*, 12325.
(98) Treacy, M. M. J. Z Dependence of Electron Scattering by Single Atoms into Annular Dark-Field Detectors. *Microsc. Microanal.* **2011**, *17*, 847–858.
(99) Miller, L. L.; Furuya, F. R.; Hainfeld, J. F.; Christopfel, W. C.; Kenny, P. W. Use of Ir4(CO)11 To Measure the Lengths of Organic Molecules with a Scanning Transmission Electron Microscope. *J. Am. Chem. Soc.* **1988**, *110*, 641–643.
(100) Lee, J. K.; Bulut, I.; Rickhaus, M.; Sheng, Y.; Li, X.; Han, G. G. D.; Andrew, G.; Briggs, D.; Anderson, H. L.; Warner, J. H. Metal Atom Markers for Imaging Epitaxial Molecular Self-Assembly on Graphene by Scanning Transmission Electron Microscopy. *ACS Nano* **2019**, *13*, 7252–7260.
(101) Sanchez, C.; Belleville, P.; Popall, M.; Nicole, L. Applications of Advanced Hybrid Organic–Inorganic Nanomaterials: From Laboratory to Market. *Chem. Soc. Rev.* **2011**, *40*, 696–753.
(102) Thomas, J. K. Physical Aspects of Photochemistry and Radiation Chemistry of Molecules Adsorbed on SiO2, γ-AI203, Zeolites, and Clays. *Chew. Rev* **1993**, *93*, 301–320.
(103) Wang, S.; Robertson, A.; Warner, J. H. Atomic Structure of Defects and Dopants in 2D Layered Transition Metal Dichalcogenides. *Chem. Soc. Rev.* **2018**, *47*, 6764–6794.
(104) Huang, P. Y.; Kurasch, S.; Srivastava, A.; Skakalova, V.; Kotakoski, J.; Krasheninnikov, A. V.; Hovden, R.; Mao, Q.; Meyer, J. C.; Smet, J.; et al. Direct Imaging of a Two-Dimensional Silica Glass on Graphene. *Nano Lett.* **2012**, *12*, 1081–1086.
(105) Börner, P. C.; Kinyanjui, M. K.; Björkman, T.; Lehnert, T.; Krasheninnikov, A. V; Kaiser, U. Observation of Charge Density Waves in Free-Standing 1T-$TaSe_2$ Monolayers by Transmission Electron Microscopy. *Appl. Phys. Lett.* **2018**, *113*, 173103.
(106) Yamashita, S.; Koshiya, S.; Nagai, T.; Kikkawa, J.; Ishizuka, K.; Kimoto, K. Quantitative Annular Dark-Field Imaging of Single-Layer Graphene—II: Atomic-Resolution Image Contrast. *Microscopy* **2015**, *64*, 409–418.
(107) Beall, G. W.; Powell, C. E. *Fundamentals of Polymer–Clay Nanocomposites*; Cambridge University Press.: Cambridge, 2011.

(108) Chen, B.; Evans, J. R. G.; Greenwell, H. C.; Boulet, P.; Coveney, P. V; Bowden, A. A.; Whiting, A. A Critical Appraisal of Polymer–Clay Nanocomposites. *Chem. Soc. Rev.* **2008**, *37*, 568–594.
(109) Kogure, T.; Murakami, T. Direct Identification of Biotite/Vermiculite Layers in Hydrobiotite Using High-Resolution TEM. *Mineral. J.* **1996**, *18*, 131–137.
(110) Kogure, T.; Jige, M.; Kameda, J.; Yamagishi, A.; Miyawaki, R.; Kitagawa, R. Stacking Structures in Pyrophyllite Revealed by High-Resolution Transmission Electron Microscopy (HRTEM). *Am. Mineral.* **2006**, *91*, 1293–1299.
(111) Kogure, T.; Okunishi, E. Cs-Corrected HAADF-STEM Imaging of Silicate Minerals. *J. Electron Microsc. (Tokyo).* **2010**, *59*, 263–271.
(112) Kogure, T. Imaging of Dioctahedral 2:1 Layers by High-Resolution Transmission Electron Microscopy (HRTEM): Possibility of Recording the Dehydroxylate. *Am. Mineral.* **2007**, *92*, 1368–1373.
(113) Kogure, T.; Morimoto, K.; Tamura, K.; Sato, H.; Yamagishi, A. XRD and HRTEM Evidence for Fixation of Cesium Ions in Vermiculite Clay. *Chem. Lett.* **2012**, *41*, 380–382.
(114) Okumura, T.; Tamura, K.; Fujii, E.; Yamada, H.; Kogure, T. Direct Observation of Cesium at the Interlayer Region in Phlogopite Mica. *Microscopy* **2014**, *63*, 65–72.
(115) Drits, V. A.; Besson, G.; Muller, F. An Improved Model for Structural Transformations of Heat-Treated Aluminous Dioctahedral 2:1 Layer Silicates. *Clays Clay Miner.* **1995**, *43*, 718–731.
(116) Gallego, J. M. Macrocycle Metalation on Solid Surfaces. In *Encyclopedia of Interfacial Chemistry: Surface Science and Electrochemistry*; Elsevier, 2018; pp 91–99.
(117) Ishida, Y.; Masui, D.; Tachibana, H.; Inoue, H.; Shimada, T.; Takagi, S. Controlling the Microadsorption Structure of Porphyrin Dye Assembly on Clay Surfaces Using the “Size-Matching Rule” for Constructing an Efficient Energy Transfer System. *ACS Appl. Mater. Interfaces* **2012**, *4*, 811–816.
(118) Fujimura, T.; Shimada, T.; Hamatani, S.; Onodera, S.; Sasai, R.; Inoue, H.; Takagi, S. High Density Intercalation of Porphyrin into Transparent Clay Membrane without Aggregation. *Langmuir* **2013**, *29*, 5060–5065.
(119) Fujimura, T.; Shimada, T.; Sasai, R.; Takagi, S. Optical Humidity Sensing Using Transparent Hybrid Film Composed of Cationic Magnesium Porphyrin and Clay Mineral. *Langmuir* **2018**, *34*, 3572-3577.

Chapter 2

Counting the Layer Number of Free-Standing Montmorillonite Nanosheets Using Annular Dark Field Scanning Transmission Electron Microscopy

2.1 Introduction

The direct imaging of low-dimensional nanomaterials, e.g., graphene, fullerene, titanium dioxide, transition metal dichalcogenides, or two-dimensional (2D) metal-organic frameworks, has significantly progressed owing to the recent development of aberration-corrected electron microscopy. Aberration-corrected transmission electron microscopy (TEM) and scanning transmission electron microscopy (STEM) are the most common techniques for characterization of ultrathin 2D nanomaterials.[1–5] Aberration-corrected optics have refined the spatial resolution of these imaging technologies to the atomic scale. This has resulted in the direct imaging of the local atomic structure, such as crystal phases, dopants, defects, and vacancies of ultrathin 2D nanomaterials.[2,6]

Conventional-TEM, high-resolution (HR) TEM, and STEM have their own advantages and limitations, as briefly summarized below. Conventional-TEM images can examine the lateral size of nanosheets and approximately determine their thickness. Ultrathin 2D nanomaterials, however, normally have low contrast in TEM images. From the HRTEM images and corresponding selected area electron diffraction patterns, one can evaluate the crystallinity, phase, crystal orientation, and exposed crystal facet of ultrathin

2D nanomaterials. However, HRTEM imaging cannot directly image or localize the different atoms, making it difficult to identify the defects, vacancies, doping, and alloyed atoms. Unlike conventional-TEM or HRTEM, focused electrons scan over the sample in the STEM mode. The types of imaging of STEM can be basically classified as bright-field (BF) and annular-dark-field (ADF) imaging by the electron detection angle. In BF−STEM mode, the electrons that are not scattered by the specimen are collected by the BF detector. These images are similar to the BF images obtained using conventional TEM. Thus, ultrathin 2D nanomaterials typically give low contrast in BF−STEM as well owing to their atomic thickness. On the other hands, ADF−STEM is an indispensable technique for analyzing local crystal structures because of its intuitive interpretability, atomic resolution, and compositional sensitivity. The ADF detector is a disk with a hole in its center where the BF detector is installed, and it detects the electrons scattered incoherently by a specimen.[7] The signal intensities of ADF−STEM are proportional to the atomic number of the atoms (i.e., Z contrast) and are the integrated intensities of each atom in an atomic column.[8,9]

In our previous study, we used anionically charged clay nanosheets of the smectite group of minerals (e.g., saponite, montmorillonite) as a host material to build a high-density and non-aggregated 2D assembly of cationic guest molecules via electrostatic interaction.[10] These clay nanosheets are ultrathin 2D nanomaterials with attractive properties of; atomically flat and negatively charged surfaces; exfoliation or stacking ability of individual nanosheets in aqueous solution; and optical transparency in the visible light region in the exfoliated state at small particle size (ca. < 200 nm).[11–16] Bulk clay minerals are widely studied and the layer stacking or distribution of the interlayer cations have been revealed using (S)TEM,[17–22] yet the material science of clay

minerals is a relatively new topic and is widely debated.

In this section, we demonstrate that ADF−STEM imaging is the most suitable imaging technique for a prompt counting of the layer number of Mt nanosheets due to its sufficient contrast compared with BF−STEM and conventional TEM imaging.

2.2 Experimental section

Materials

Montmorillonite was acquired from Kunimine Industries (Kunipia F with the chemical structure corresponding to $Na_{0.35}K_{0.01}Ca_{0.06}(Al_{1.56}Mg_{0.33}Fe_{0.09}Ti_{0.01})(Si_{3.87}Al_{0.13})O_{10}(OH)_2$ [23] and the cation exchange capacity of 1.19 meq. g^{-1} [24]) and was purified using the following procedure. First, raw clay dispersion (300 mL, 10 g L^{-1}) was poured into centrifuge bottles, which were then centrifuged at a rotation speed of 7,000 rpm for 15 min. The obtained supernatant was collected and poured into a container with 1,500 mL of ethanol. After 1 h of mixing at a temperature of 70 °C, the resulting colloidal solution was filtered using a PTFE membrane with a pore size of 0.1 μm (Millipore). The produced cake was collected and dried under vacuum by a rotary pump overnight. Then, the dried cake was dispersed in water, and the suspension was stored overnight to achieve complete exfoliation into nanosheets.

Sample preparation and STEM/TEM observation

A specimen for STEM/TEM was prepared by drop-casting the aqueous solution of the Mt nanosheets onto a holey carbon-coated Cu grid. The STEM/TEM observations were conducted with a JEM-ARM200F (JEOL) instrument, which had spherical

aberration correctors in STEM mode. The acceleration voltage was set at 80 kV. The camera length was set to 100 mm and the convergence semi-angle of the incident probe was ~13.8 mrad. The detection semi-angle of the ADF−STEM detector was 54−220 mrad.

2.3 Results and discussion

A cross-sectional view of the unit layer structure of a typical montmorillonite is shown in Figure 1. The unit layer comprises 2:1 pair of tetrahedral silica and octahedral aluminum hydroxide sheets. The general chemical formula of the layered aluminosilicates, such as Mt, mica, and pyrophyllite, is $[Si_4O_8][Al_2O_2(OH)_2]$. The isomorphous substitution of Al^{3+} to Mg^{2+} in the octahedral sheet produces anionic charges within the Mt structure.

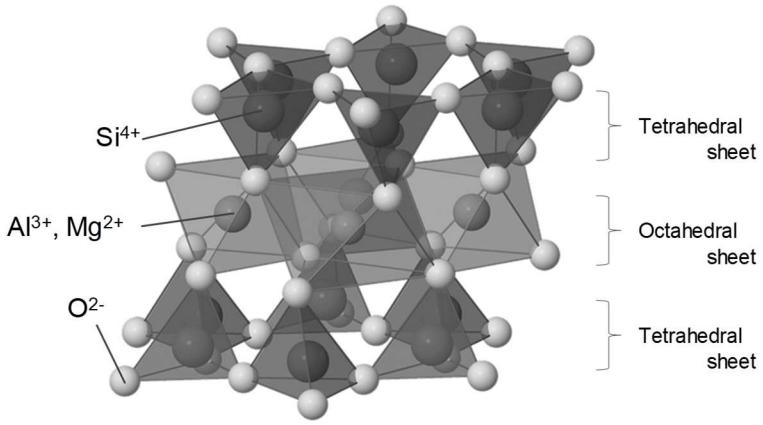

Figure 1. Atomic structure model of the unit layer of montmorillonite showing the octahedral alumina sheet sandwiched by two tetrahedral silica sheets. Hydrogen atoms are omitted for clarity.

ADF−STEM, BF−STEM, and conventional-TEM images of the free-standing Mt nanosheets and the corresponding intensity profiles of the white boxed regions are shown in Figure 2. As shown in Figure 2a, there are distinct differences in the ADF contrast between the vacuum and the regions of the Mt nanosheets. Meanwhile, the difference in contrast was less obvious in the BF−STEM and conventional TEM images (Figures 2b, c), although the edges of the Mt nanosheet were detectable in their images up to one or two layers. The intensity profile along 1−1' in Figure 2a consistently exhibits a stepwise feature corresponding to vacuum, the edges of the monolayer, and the bilayer Mt nanosheet as visually detectable by ADF images, while there was no apparent feature for 2−2' and 3−3' (Figures 2e, f). These results suggest that ADF−STEM is the most suitable imaging technique for a prompt detection of the monolayer Mt nanosheet.

To attempt to count the layer number of Mt nanosheets by the ADF−STEM imaging, we compared the intensity profiles along the different particles of the Mt nanosheet in an ADF−STEM image. Figures 3a and b show ADF−STEM images of free-standing Mt nanosheets and their overlaid image with the information of the edges of the Mt nanosheets and the corresponding stacked layer number. As shown in Figure 3b, the edges of the monolayer (1L) to four-layered (4L) Mt nanosheet regions were distinguished by the difference in the ADF contrast among them. When many nanosheets are overlapped, counting of the layer number by the edges in the ADF−STEM image was difficult due to the complicated form of stacking and a loss of horizontality. As demonstrated in Figures 3c and d, the intensity profiles along A−A' and B−B' exhibit similar stepwise features, although different particles of the Mt nanosheet were included in A−A' and B−B'. The five steps in the intensity profiles along A−A' and B−B' (Figure 3d) are distinguishable as the vacuum and Mt nanosheet with 1L–4L regions, as

determined by the ADF image, respectively. Note that there was no observable sample contamination.

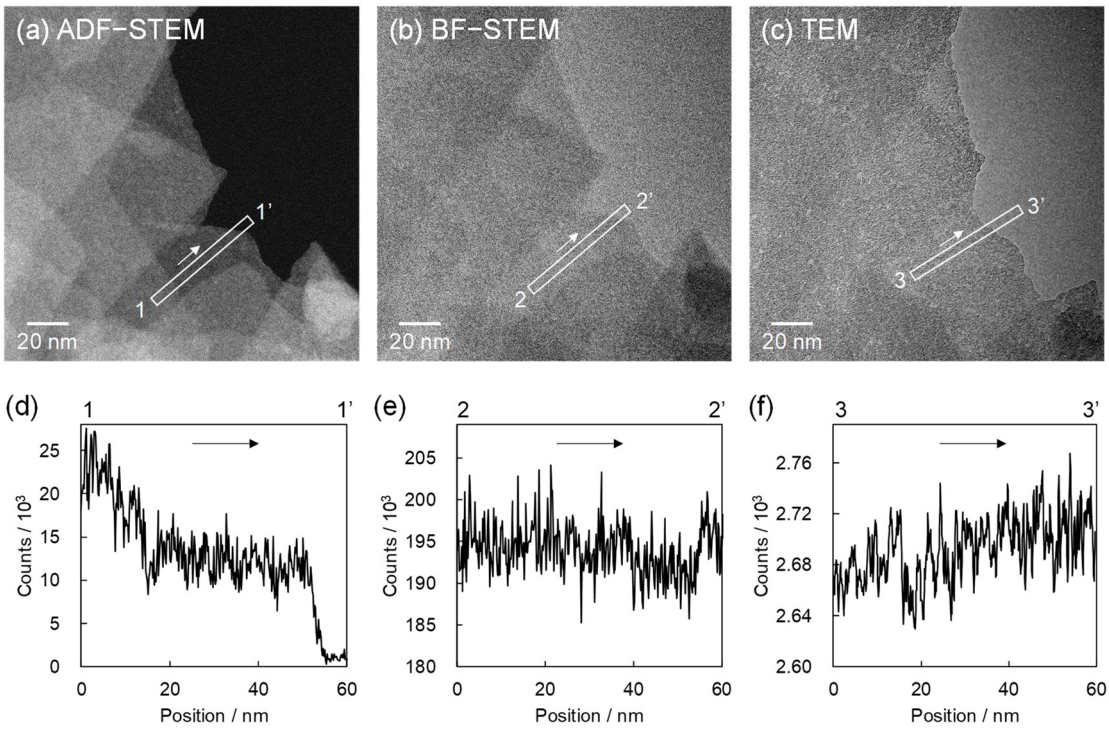

Figure 2. Comparison of three imaging techniques for free-standing Mt nanosheets: (a) ADF−STEM; (b) BF−STEM; (c) conventional TEM. (d–f) Intensity profiles of the white boxed region in (a), (b), and (c), along the longitudinal direction indicated by the arrows. The acceleration voltage and the magnification were 80 kV and 1.2 M×. Pixel time and image size of STEM were set at 15 μs and 1,024×1,024 pixel, respectively. Acquisition time and image size of TEM were set at 1 s and 2,048×2,048 pixel, respectively.

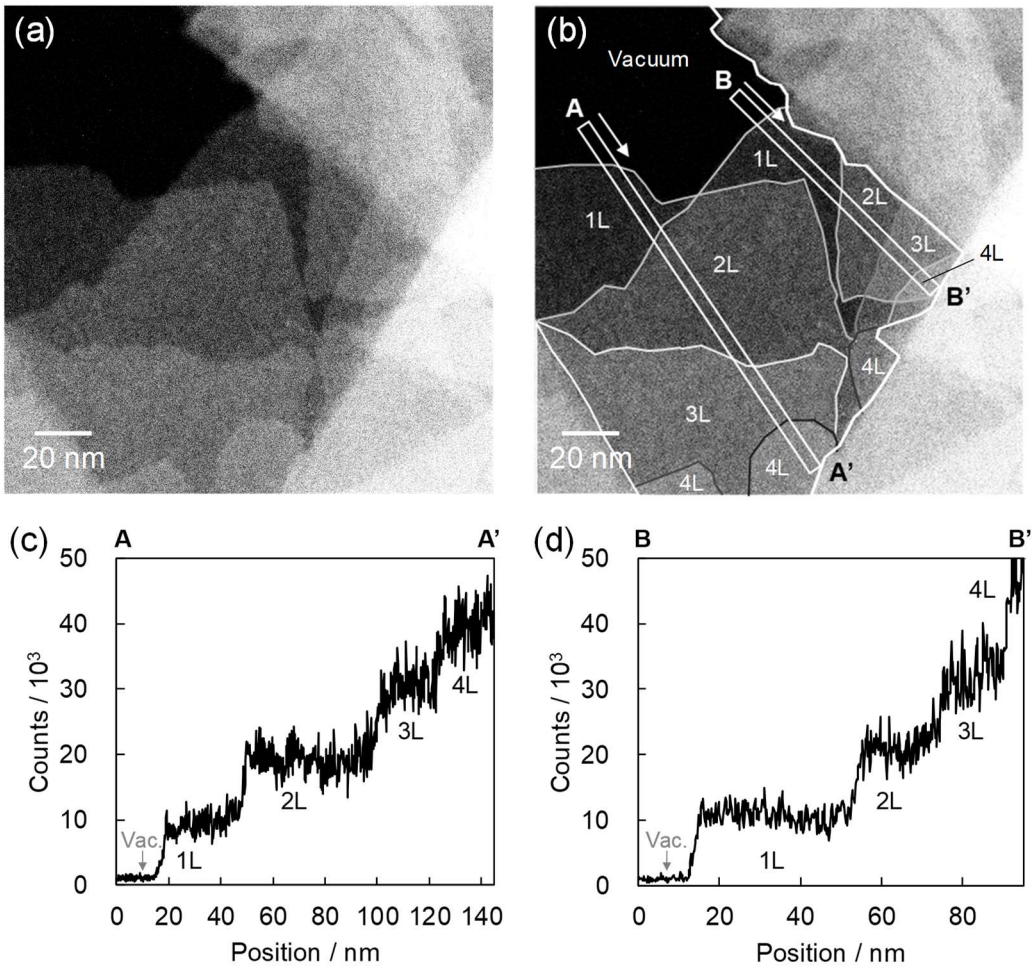

Figure 3. (a) ADF−STEM image of free-standing Mt nanosheets. (b) Overlay image on (a) indicating the edges of the Mt nanosheets and the corresponding stacked layer number from one (1L) to four (4L). (c, d) Intensity profiles of the white boxed region A−A' and B−B' in (b) along the longitudinal direction indicated by the arrows, respectively. The acceleration voltage and the magnification were 80 kV and 1.2 M×. Pixel time and image size of STEM were set at 15 μs and 1,024×1,024 pixel, respectively.

Figure 4 shows the averaged ADF signal intensities of each step of the intensity profiles along A−A' and B−B' (Figures 3c and d), which are plotted against the layer number of the Mt nanosheets determined by the ADF image. The averaged value of the ADF signal intensities was obtained by averaging the intensity of each step on A−A' and B−B', except for the step edges in which the intensity changed gradually depending on the angle between the edges of the Mt nanosheet and the longitudinal direction of the white boxes. The corresponding standard deviations are also indicated as the error bars in Figure 4. Note that the small difference in the averaged contrast values between A−A' and B−B' may be caused by a small bending of the nanosheets or a tilting of the specimen. In both cases of A−A' and B−B', the ADF signal intensities increased in proportion to the layer number of the Mt nanosheets determined by the ADF image. Furthermore, the ADF contrast on A−A' and B−B' were in good agreement, even though A−A' and B−B' included the different particles of the Mt nanosheets. This result strongly indicates that the layer number of Mt nanosheets can be quantitively determined by ADF imaging.

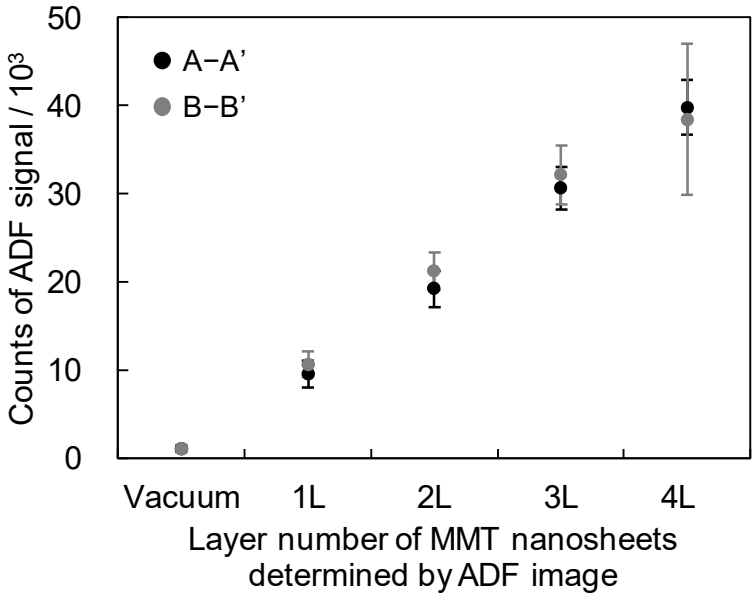

Figure 4. Layer number dependence of the averaged ADF contrast in the vacuum and 1L–4L Mt nanosheet region obtained from the intensity profiles along A−A' (black) and B−B' (gray) in Figure 3b, respectively.

2.4 Conclusion

In this section, we demonstrate the direct determination of the layer number of free-standing montmorillonite (Mt) nanosheets using annular dark field (ADF) scanning transmission electron microscopy (STEM). The layer number of the free-standing Mt nanosheets deposited on a holey carbon-coated grid was successfully counted to range from monolayer to four layers by the difference in the ADF contrast. Meanwhile, counting of the layer numbers was difficult using conventional TEM and bright field STEM due to the low contrast. Therefore, ADF−STEM can potentially be applied to further investigate the clay nanosheets and their molecular complexes by the atomic scale imaging for a deeper understanding of clay-nanosheet-based chemistry.

2.5 References

(1) Lin, Y. C.; Susi, T.; Kotakoski, J.; Ramasse, Q. M.; Kepaptsoglou, D.; Meyer, J. C.; Suenaga, K. Towards Atomically Precise Manipulation of 2D Nanostructures in the Electron Microscope. *2D Mater.* **2017**, *4*, 042004.

(2) Tan, C.; Cao, X.; Wu, X. J.; He, Q.; Yang, J.; Zhang, X.; Chen, J.; Zhao, W.; Han, S.; Nam, G. H.; et al. Recent Advances in Ultrathin Two-Dimensional Nanomaterials. *Chem. Rev.* **2017**, *117*, 6225–6331.

(3) Hashimoto, A.; Suenaga, K.; Gloter, A.; Urita, K.; Iijima, S. Direct Evidence for Atomic Defects in Graphene Layers. *Nature* **2004**, *430*, 870–873.

(4) Hirsch, A.; Hauke, F. Post-Graphene 2D Chemistry: The Emerging Field of Molybdenum Disulfide and Black Phosphorus Functionalization. *Angew. Chem. Int. Ed.* **2018**, *57*, 4338–4354.

(5) Wang, S.; Robertson, A.; Warner, J. H. Atomic Structure of Defects and Dopants in 2D Layered Transition Metal Dichalcogenides. *Chem. Soc. Rev.* **2018**, *47*, 6764–6794.

(6) Mas-Ballesté, R.; Gómez-Navarro, C.; Gómez-Herrero, J.; Zamora, F. 2D Materials: To Graphene and Beyond. *Nanoscale* **2011**, *3*, 20–30.

(7) Pennycook, S. J.; Jesson, D. E. High-Resolution Z-Contrast Imaging of Crystals. *Ultramicroscopy* **1991**, *37*, 14–38.

(8) LeBeau, J. M.; Stemmer, S. Experimental Quantification of Annular Dark-Field Images in Scanning Transmission Electron Microscopy. *Ultramicroscopy* **2008**, *108*, 1653–1658.

(9) Yamashita, S.; Kikkawa, J.; Yanagisawa, K.; Nagai, T.; Ishizuka, K.; Kimoto, K. Atomic Number Dependence of Z Contrast in Scanning Transmission Electron Microscopy. *Sci. Rep.* **2018**, *8*, 12325.

(10) Ishida, Y. Manipulation of Supramolecular 2D Assembly of Functional Dyes toward Artificial Light-Harvesting Systems. *Pure Appl. Chem.* **2015**, *87*, 3–14.

(11) Shichi, T.; Takagi, K. Clay Minerals as Photochemical Reaction Fields. *J. Photochem. Photobiol. C Photochem. Rev.* **2000**, *1*, 113–130.

(12) López Arbeloa, F.; Martínez Martínez, V.; Arbeloa, T.; López Arbeloa, I. Photoresponse and Anisotropy of Rhodamine Dye Intercalated in Ordered Clay Layered Films. *J. Photochem. Photobiol. C Photochem. Rev.* **2007**, *8*, 85–108.

(13) Takagi, S.; Shimada, T.; Ishida, Y.; Fujimura, T.; Masui, D.; Tachibana, H.; Eguchi, M.; Inoue, H. Size-Matching Effect on Inorganic Nanosheets: Control of Distance, Alignment, and Orientation of Molecular Adsorption as a Bottom-up Methodology for Nanomaterials. *Langmuir* **2013**, *29*, 2108–2119.

(14) Okada, T.; Ide, Y.; Ogawa, M. Organic-Inorganic Hybrids Based on Ultrathin Oxide Layers: Designed Nanostructures for Molecular Recognition. *Chem. Asian J.* **2012**, *7*, 1980–1992.

(15) Thomas, J. K. Physical Aspects of Photochemistry and Radiation Chemistry of Molecules Adsorbed on SiO2, γ-AI203, Zeolites, and Clays. *Chew. Rev* **1993**, *93*, 301–320.

(16) Bujdák, J. Effect of the Layer Charge of Clay Minerals on Optical Properties of Organic Dyes. A Review. *Appl. Clay Sci.* **2006**, *34*, 58–73.

(17) Okumura, T.; Tamura, K.; Fujii, E.; Yamada, H.; Kogure, T. Direct Observation of Cesium at the Interlayer Region in Phlogopite Mica. *Microscopy* **2014**, *63*, 65–72.
(18) Kogure, T.; Okunishi, E. Cs-Corrected HAADF-STEM Imaging of Silicate Minerals. *J. Electron Microsc. (Tokyo).* **2010**, *59*, 263–271.
(19) Kogure, T.; Murakami, T. Direct Identification of Biotite/Vermiculite Layers in Hydrobiotite Using High-Resolution TEM. *Mineral. J.* **1996**, *18*, 131–137.
(20) Kogure, T.; Jige, M.; Kameda, J.; Yamagishi, A.; Miyawaki, R.; Kitagawa, R. Stacking Structures in Pyrophyllite Revealed by High-Resolution Transmission Electron Microscopy (HRTEM). *Am. Mineral.* **2006**, *91*, 1293–1299.
(21) Banfield, J. F.; Murakami, T. Atomic-Resolution Transmission Electron Microscope Evidence for the Mechanism by Which Chlorite Weathers to 1:1 Semi-Regular Chlorite-Vermiculite. *Am. Mineral.* **1998**, *83*, 348–357.
(22) Buseck, P. R.; Iijima, S. High Resolution Electron Microscopy of Silicates. *Am. Mineral.* **1974**, *59*, 1–21.
(23) Takahashi, T.; Ohkubo, T.; Suzuki, K.; Ikeda, Y. High Resolution Solid-State NMR Studies on Dissolution and Alteration of Na-Montmorillonite under Highly Alkaline Conditions. *Microporous Mesoporous Mater.* **2007**, *106*, 284–297.
(24) Seyama, H.; Soma, M. X-Ray Photoelectron and Auger Electron Spectroscopic Study of Mg-Montmorillonite. *Chem. Lett.* **1981**, *10*, 1009-1012.

Chapter 3

Atomic-scale imaging of a free-standing monolayer clay mineral nanosheet using scanning transmission electron microscopy

3.1 Introduction

Recent powerful characterization techniques have uncovered the useful structural and electronic properties of ultrathin two-dimensional (2D) nanomaterials (e.g. graphene, molybdenum disulfide, hexagonal boron nitride, transition metal dichalcogenides, and black phosphorus) that are intrinsically related to their characteristics and functionalities.[1–4] Transmission electron microscopy (TEM) and scanning transmission electron microscopy (STEM) are the most common technique to characterize ultrathin 2D nanomaterials.[1,5–9] Aberration-corrected optics has refined the spatial resolution of these imaging technologies to the atomic scale. This has resulted in the direct imaging of the local atomic structure, such as crystal phases, dopants, defects, and vacancies. ¥In the fields of mineralogy, bulk (stacked) clay minerals are widely studied to reveal the layer stacking or distribution of the interlayer cations yet the material science of clay nanosheet is a relatively new topic and is widely debated. (S)TEM observations of bulk clay minerals at the atomic scale from a cross-sectional direction have been conducted to visualize the atomic columns [10,11], while STEM imaging of a free-standing clay nanosheet, which doesn't contain any supports such as surfactants or

polymer matrices, at an atomic resolution along the plane direction has not been achieved in spite of many reports on the few-atom-thick graphene analogs.[1,5–9] Atomic-scale direct imaging of clay mineral nanosheets or other 2D nanomaterials having electron-beam sensitivity and structural-complexity will make a significant advancement for fundamental understanding of these materials and further promote organic-inorganic hybrid materials that have strongly relied on these non-graphene-family 2D nanomaterials.[12–17] In this section, we demonstrate the first direct atomic-scale imaging of a free-standing monolayer montmorillonite (Mt) nanosheet by annular dark field (ADF) imaging on an aberration-corrected STEM.

3.2 Experimental section

Specimen preparation.

Montmorillonite, a typical anionic clay mineral, was acquired from Kunimine Industries (Kunipia F, its chemical structure corresponded to the formula $Na_{0.66}(Al_{3.34}Mg_{0.66})Si_8O_{20}(OH)_4$ with the cation exchange capacity equal to 1.19 meq. g^{-1}) and was purified using the following procedure. First, raw clay dispersion (300 mL, 10 g L^{-1}) was placed in centrifuge bottles, which were then centrifuged at a rotation speed of 7000 rpm for 15 min. The obtained supernatant was collected and poured into a container with 1500 mL of ethanol. After 1 h of mixing at a temperature of 70°C, the resulting colloidal solution was filtered using a PTFE membrane with a pore size of 0.1 μm (Millipore). The produced cake was collected and dried under vacuum by rotary pump overnight. The dried cake was dispersed in water, and the dispersion was stored overnight to achieve complete exfoliation into nanosheets. A specimen for STEM/TEM was

prepared by drop casting the aqueous solution of Mt nanosheets on a holey carbon coated Cu grid.

ADF−STEM experiments and simulations.

For the STEM observations, a Titan Cubed G2 equipped with spherical aberration correctors was used at an acceleration voltage of 300 kV. The convergence semi-angle of the incident probe was 21.4 mrad. The inner and outer detection semi-angle of ADF detector were 31.4 and 192 mrad, respectively. The incident probe current was set to ~30 pA. The ADF–STEM image simulations were performed using a multislice program Dr. Probe.[18] The unit cell information of montmorillonite for simulation was downloaded from the Crystallography Open Database[19] with CIF number 1100106 followed by modification. The cell dimension is a = 5.411 (4), b= 9.0 (5), c = 10.25 (2) Å, β = 100.3 (1) º as shown in Figure 1. The electron optical parameters were set to the experimental conditions. FWHM of the incident beam was set to 90 pm for the simulation. Low-pass and Fourier filtering were performed using the DigitalMicrograph (Gatan). In Fourier filtering the crystalline reflections were placed a finite sized mask, inverse FFT was performed using only the intensity inside the masked regions.

3.3 Results and discussion

The unit layer structure of a typical monolayer montmorillonite (1L-Mt) nanosheet seen from the cross-section direction is shown in Fig. 1a. The unit layer of 1L-Mt nanosheet consists of 2:1 pairs of tetrahedral silica and octahedral aluminohydroxide sheets. The general chemical formula for layered aluminosilicates such as Mt, mica and pyrophyllite is $[Si_4O_8][Al_2O_2(OH)_2]$. In case of Mt, the isomorphous substitution of Al^{3+} to Mg^{2+} in the octahedral sheet produces anionic charges within the structure. In this work, we used industrial purified natural Mt from the original bentonite of Tukinuno Mine with further purification (for the details, see experimental procedures in Supplementary Information). Figures 1b-d show the atomic structure model and the corresponding simulated ADF–STEM image of the 1L-Mt nanosheet visualized from the normal to plane direction (z direction). The apexes of the yellow and red hexagons in Fig. 1c indicate the central coordinates of the Si atoms in two tetrahedral sheets of the Mt nanosheet. A small shift of 1.7 Å can be observed along the a direction. Observed from the normal to the surface direction, the atomic structure of the 1L-Mt nanosheet has two hexagonal networks of Si and adjacent atoms of O, Al (or Mg) with pores in the center. The simulated ADF image in Fig. 1d shows a hexagonal contrast pattern with a pore of ~4 Å corresponding to the atomic structure of 1L-Mt nanosheet, which consisted of adjacent Si, Al, Mg, and O atoms. Incidentally, we could not distinguish the position of each of the Si, O, Al (or Mg) atoms one by one in the simulated ADF image, even under ideal conditions (see Fig. S1 in Supplementary Information, for correspondence between atomic structure model, projection potential of ADF−STEM, and simulated ADF−STEM image). Note that Na^+ interlayer cations were omitted for the analysis since they would

freely move on the surface of nanosheet that results in the negligible contrast in the imaging.

Figure 2a shows an ADF−STEM image of the free-standing Mt nanosheets on a holey carbon film at low magnification. The acceleration voltage and the incident probe current were 300 kV and ~30 pA, respectively. A STEM sample was prepared by pouring an aqueous dispersion of the Mt nanosheets onto a carbon-coated Cu grid. As shown in Fig. 2a, the Mt nanosheets are stacked horizontally. Hence, the electron beam was irradiated normal to the surface direction. The stacking number of the Mt nanosheets from one (1L-) to three (3L-) layers, indicated in Fig. 1a, was determined by the difference between their contrasts. Figure 2b shows a representative selected area electron diffraction (SAED) pattern of the 1L-Mt nanosheet obtained by the TEM mode. The in-plane distances, d, summarized in Table S1, were determined by the SAED pattern. The d values are in good agreement with the values of (hk0) facets reported elsewhere.[20] Note that, due to their thin structure composed of light elements, the Mt nanosheets, especially 1L-Mt, were difficult to detect by TEM. Therefore, the stacking number of the Mt nanosheets was determined by ADF−STEM, where the contrast is primarily proportional to the thickness of the specimen. For this procedure, we used ADF−STEM at low-magnification, i.e. low dose rate, to minimize the effect of the electron beam on the Mt nanosheet structure. The decrease in their crystallinity due to ADF–STEM was negligible (for evidence of the effects of the electron beam on the Mt nanosheet, see Fig. S2 in the Supplementary Information with sequentially recorded ADF−STEM images and the corresponding FFTs).

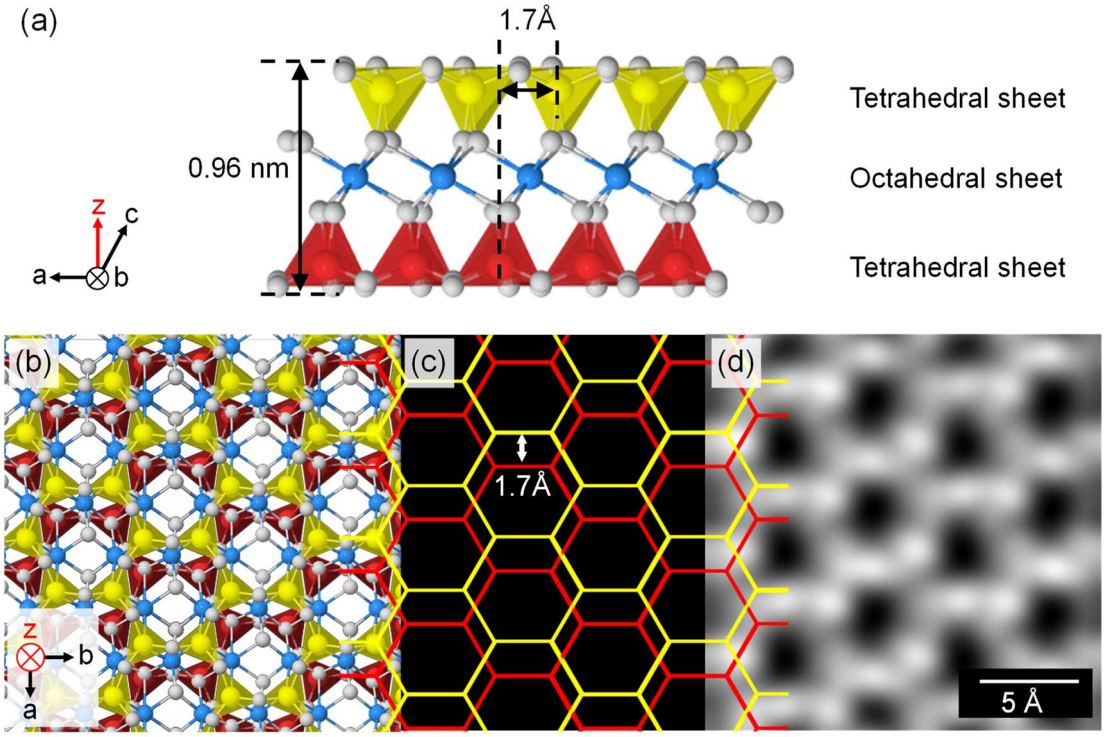

Figure 1. Structural model and simulated ADF–STEM image of 1L-Mt. (a) Atomic structure model of a typical monolayer montmorillonite (1L-Mt) nanosheet along the b direction, showing that the octahedral alumina sheet is sandwiched by two tetrahedral silica sheets. (b-d) Correspondence between an atomic structure model (b) and the simulated ADF–STEM image (d) of 1L-Mt nanosheet along the z-axis, which is perpendicular to the plane direction. The two Si tetrahedral sheets in the Mt nanosheet are distinguished by yellow and red colors, respectively. The apexes of the hexagons in (c) indicate the central coordinates of the Si atoms. Colors: Si, yellow and red; Al, Mg; blue, O, grey. Hydrogen are omitted, for clarity.

Figure 3 is an experimental ADF−STEM image after low-pass filtering and the corresponding Fourier transform (FT), at a high magnification (see Fig. S3 in the Supplementary Information, for the original ADF−STEM images). The acceleration voltage and the incident probe current were 300 kV and ~30 pA, respectively. The acquisition time was set to 10s. The FT pattern of the 1L-Mt nanosheet is in good agreement with the SAED pattern in TEM (Fig. 2b), indicating that the nanosheet retained its crystallinity during the ADF−STEM acquisition. In other words, the free-standing 1L-Mt nanosheets were stable during the ADF−STEM observation. This is contrast to the general knowledge of bulk clay minerals that reported high sensitivity of the bulk clay mineral, namely intensely stacked nanosheets to electron beams and lack of resistance to damage.[21–24] By observing ADF−STEM at various tilted angles, we confirm that the tilting in the specimen was less than 10°. When the tilting is over 10°, the 1L-Mt nanosheets are out of focus and not discernible (for the sequentially recorded ADF−STEM images at various tilted angles, see Figure S4 in Supplementary Information).

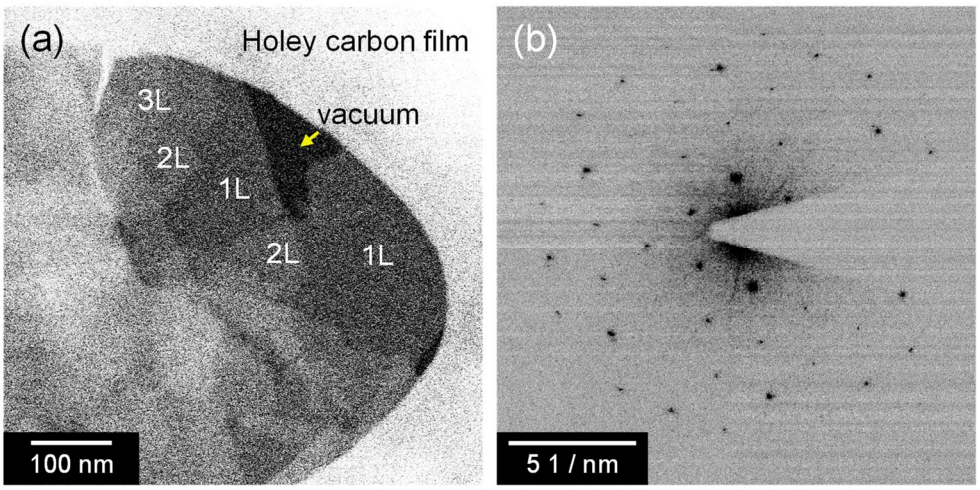

Figure 2. Low magnification ADF–STEM and SAED pattern. (a) Low-magnification ADF–STEM image of free-standing Mt nanosheets on holey carbon film. The stacking number of Mt nanosheets from one (1L-) to three (3L-) layers was determined by the difference between their ADF contrasts. (b) A representative selected area electron diffraction (SAED) pattern of 1L-Mt nanosheet obtained by TEM mode.

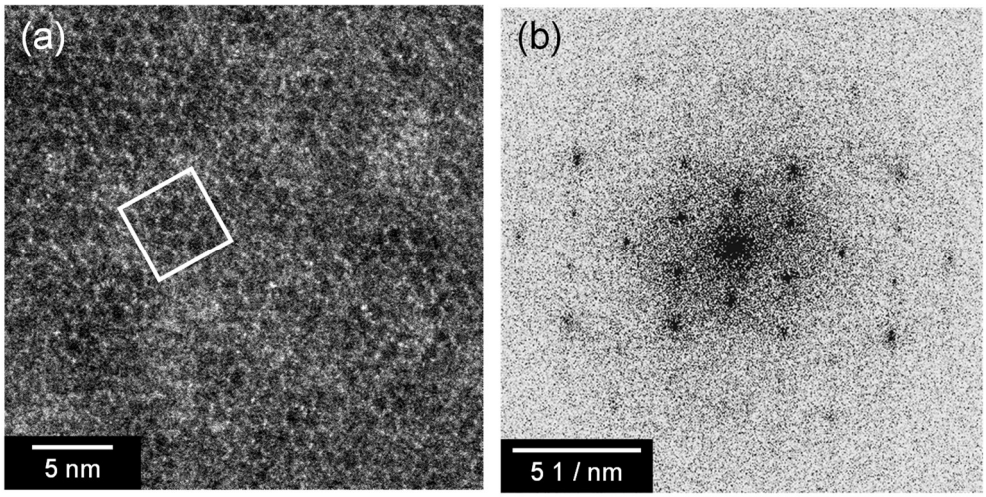

Figure 3. ADF–STEM image of 1L-Mt nanosheet (a) with low-pass filtering and (b) the corresponding Fourier transform.

In insulating materials such as clay minerals, inelastic scattering is the dominant cause of beam damage, because the holes left by the ejected electrons cannot be compensated quickly by the surroundings electrons.[35] It should be noted that, if the specimen is made of a very thin film or small-sized particles, the beam sensitivity decreases as the secondary electrons excited from near-surface atoms escape from the specimen to vacuum without causing damage.[25,26] Hence, in the ADF−STEM observation, due to its thin structure (0.96 nm), the beam damage to the Mt nanosheet along the surface direction could be contained. In addition, because these escaped electrons are not compensated by the neighboring electrons quickly, the insulating specimen gained a positive charge.[27] For ionic materials such as clay minerals, this positive charge can induce an electric field in the specimen, which results in image drift or distortion, structural change, or mass transport due to ion drift.[25]

Figures 4a and b show a higher magnification print of a small area in Fig. 3 (white square) before and after Fourier filtering, respectively. For comparison, the simulated ADF−STEM image after noise addition is shown in Fig. 4c. The hexagonal contrast pattern with ~4 Å pores found in the experimental ADF−STEM image is in good agreement with that in the simulated image, which corresponds to the atomic structure of the 1L-Mt nanosheet. This is the first atomic-scale observation of free-standing Mt nanosheet by ADF−STEM. Note that the experimental ADF−STEM image was less detailed than the simulated one owing to the slight drift in the specimen. It should also be noted that the hexagonal pattern obtained in the experimental image (Fig. 4b) was slightly distorted. Although it was difficult to directly distinguish each of the Si, O, Al (or Mg) atom one by one, the distortion observed in the ADF contrast pattern could be an evidence for the atomic localization of isomorphous substituted cations or sites of vacancies, which

cause the change in length or angle of the chemical bonds. Until now, it has been difficult to observe the actual distribution of isomorphous substituted cations and sites of vacancies in the local atomic structure directly by cross-sectional electron microscopy of bulk clay mineral.[21,22,28]

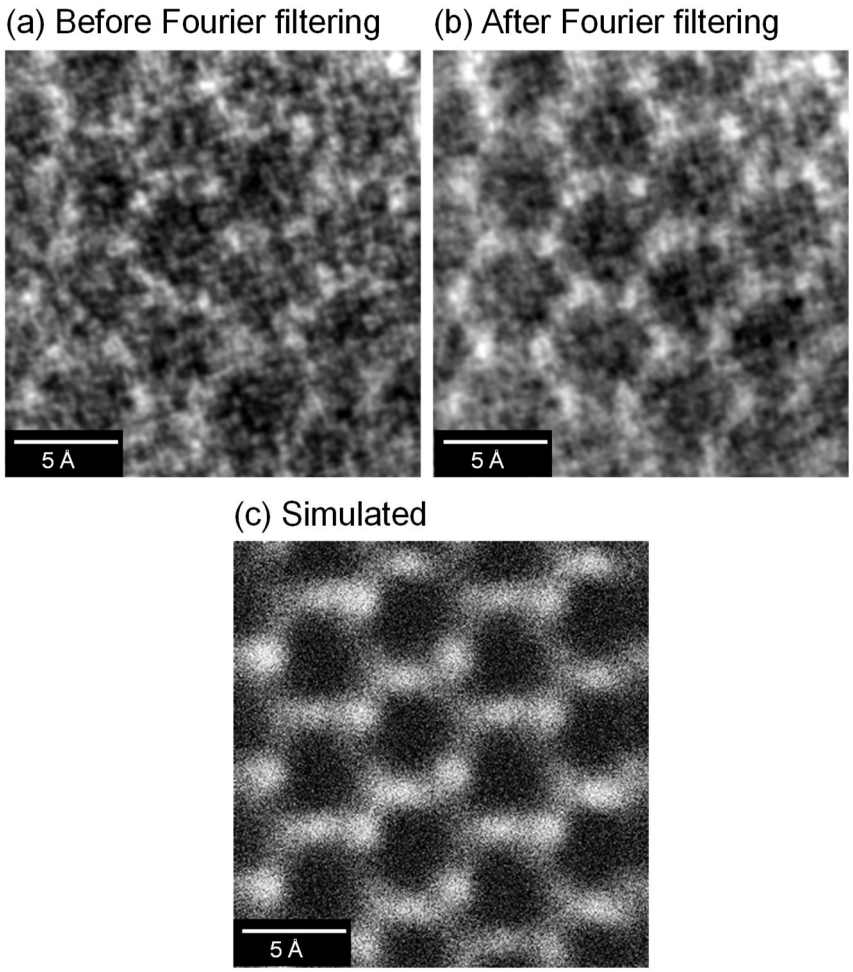

Figure 4. Atomic-scale imaging of Mt nanosheet. (a) and (b) are a higher magnification print of the ADF−STEM image before and after Fourier filtering, respectively. The selected area is also indicated (white square) in Fig. 3. (c) A simulated ADF–STEM image of 1L-Mt obtained via noise addition to the image in Fig. 1b.

3.4 Conclusion

In this section, we have demonstrated the first direct observation of a free-standing monolayer clay mineral nanosheet at the atomic scale using ADF−STEM. While bulk clay minerals are quickly damaged by electron beam, the ultra-thin monolayer Mt nanosheet was stably observed during the ADF−STEM observation because secondary electrons excited from the near-surface atoms may efficiently escape from the specimen to vacuum without causing damage. Furthermore, as compared to the simulated ADF−STEM, the hexagonal contrast pattern found in the experimental images corresponded to the atomic structure of Mt, which consisted of adjacent Si, Al, Mg, and O atoms with a pore of ~4 Å. The results offer the usefulness of the ADF−STEM techniques for the atomic scale imaging of clay nanosheets and similar 2D materials having more structural complexity than few-atom-thick graphene analogs, and thus widen the spectrum of atomic-scale characterization of various 2D nanomaterials.

3.5 Supporting information

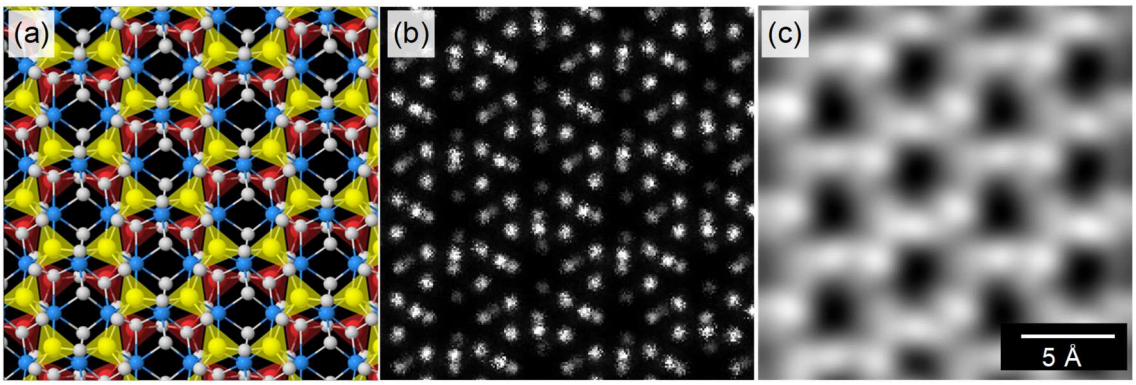

Figure S1. A correspondence between atomic structure model (a), the mapping of the projection potential following the atomic number dependence (i.e., Z contrast) of ADF signal (b), and the simulated ADF−STEM image (c).

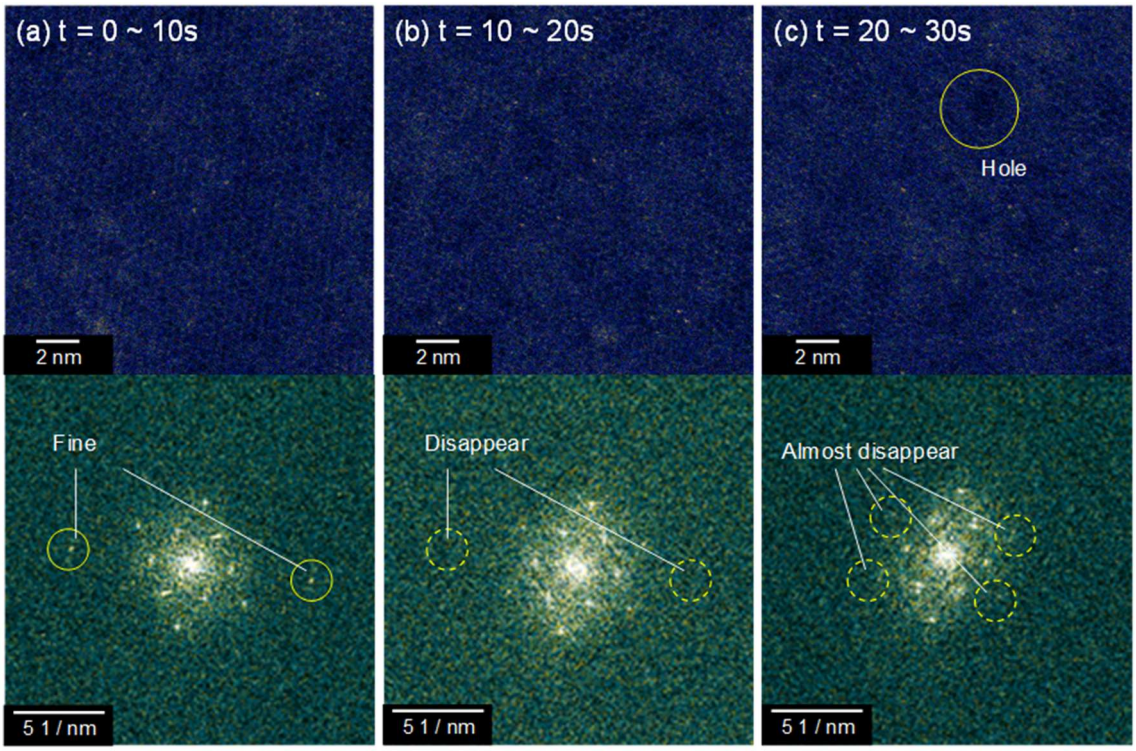

Figure S2. Sequential ADF–STEM images and corresponding FT images to demonstrate the effect of the electron beam damage with long time exposure. For the observations, a JEM-ARM200F (JEOL) equipped with spherical aberration correctors was used at an acceleration voltage of 80 kV. The convergence semi-angle of the incident probe was 14~17 mrad. The inner and outer detection semi-angle of ADF detector were 45 and 220 mrad, respectively.

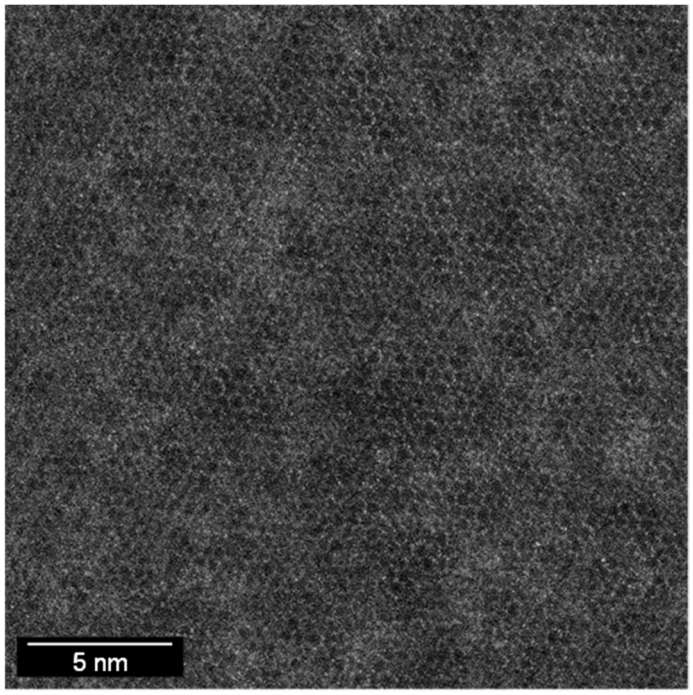

Figure S3. An ADF–STEM image of 1L-Mt nanosheet. The acceleration voltage and the incident probe current were 300 kV and ~ 30 pA, respectively. Acquisition time was set at 10s.

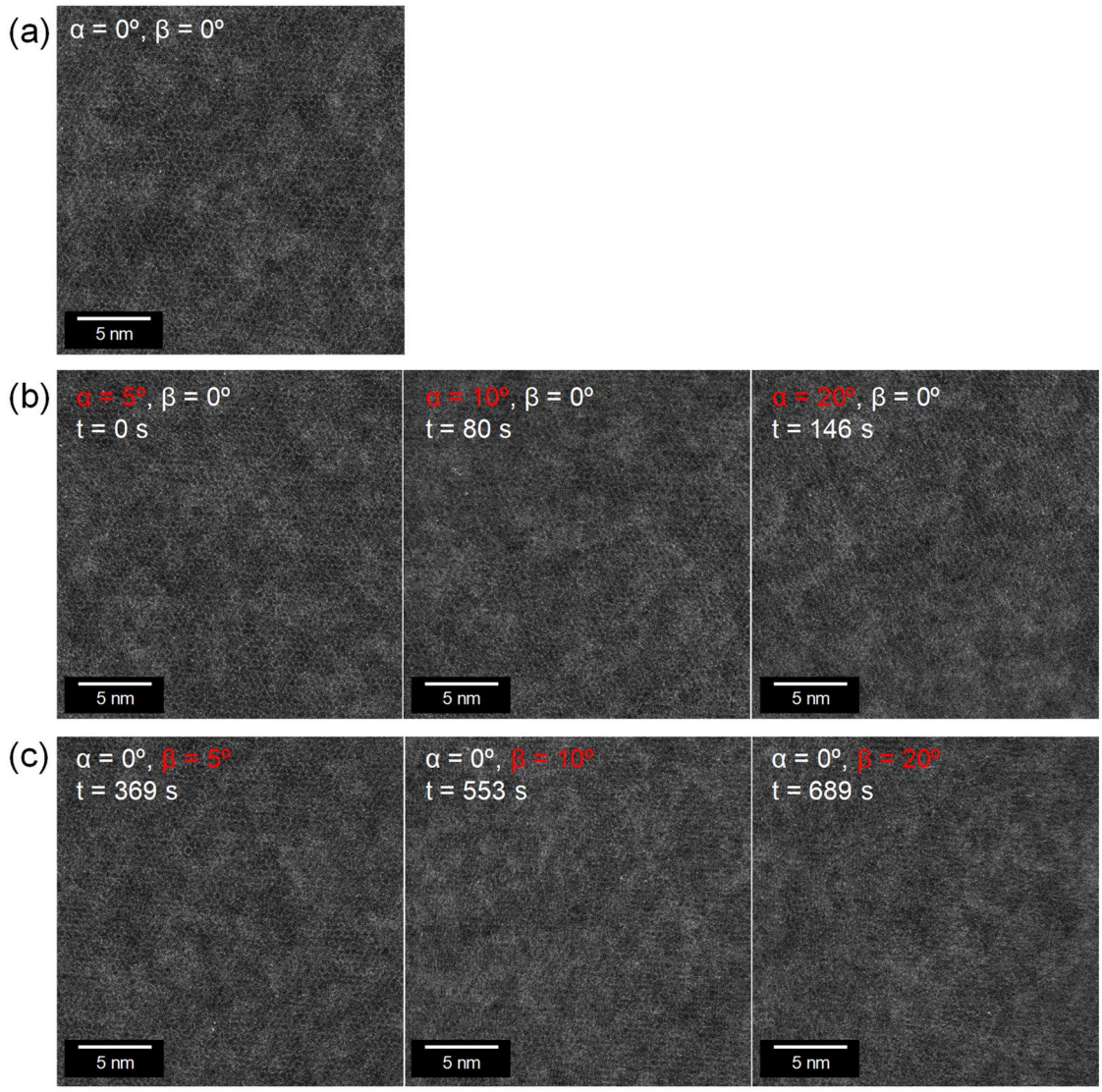

Figure S4. (a) an ADF–STEM image in plane direction with clear hexagonal contrast pattern. Series of ADF–STEM images tilted in (b) angle α around x-axis and (c) angle β around y axis.

Table S1. In-plane distance, d, of 1L-Mt nanosheet determined by SAED (Fig. 2b). The d values are in good agreement with the values of (hk0) facets reported elsewhere.*[20]

(h k l) *	d / Å
110, 020	4.63
130, 200	2.65
220, 040	2.32
310, 150, 240	1.75
330, 060	1.54
260, 400	1.32
350, 170, 420	1.27

3.6 References

(1) Tan, C.; Cao, X.; Wu, X. J.; He, Q.; Yang, J.; Zhang, X.; Chen, J.; Zhao, W.; Han, S.; Nam, G. H.; et al. Recent Advances in Ultrathin Two-Dimensional Nanomaterials. *Chem. Rev.* **2017**, *117*, 6225–6331.

(2) Mas-Ballesté, R.; Gómez-Navarro, C.; Gómez-Herrero, J.; Zamora, F. 2D Materials: To Graphene and Beyond. *Nanoscale* **2011**, *3*, 20–30.

(3) Hirsch, A.; Hauke, F. Post-Graphene 2D Chemistry: The Emerging Field of Molybdenum Disulfide and Black Phosphorus Functionalization. *Angew. Chem. Int. Ed.* **2018**, *57*, 4338–4354.

(4) Rao, C. N. R.; Sood, A. K.; Subrahmanyam, K. S.; Govindaraj, A. Graphene : The New Two-Dimensional Nanomaterial. *Angew. Chem. Int. Ed.* **2009**, *48*, 7752–7777.

(5) Wang, S.; Robertson, A.; Warner, J. H. Atomic Structure of Defects and Dopants in 2D Layered Transition Metal Dichalcogenides. *Chem. Soc. Rev.* **2018**, *47*, 6764–6794.

(6) Hashimoto, A.; Suenaga, K.; Gloter, A.; Urita, K.; Iijima, S. Direct Evidence for Atomic Defects in Graphene Layers. *Nature* **2004**, *430*, 870–873.

(7) Huang, P. Y.; Kurasch, S.; Srivastava, A.; Skakalova, V.; Kotakoski, J.; Krasheninnikov, A. V.; Hovden, R.; Mao, Q.; Meyer, J. C.; Smet, J.; et al. Direct Imaging of a Two-Dimensional Silica Glass on Graphene. *Nano Lett.* **2012**, *12*, 1081–1086.

(8) Börner, P. C.; Kinyanjui, M. K.; Björkman, T.; Lehnert, T.; Krasheninnikov, A. V; Kaiser, U. Observation of Charge Density Waves in Free-Standing 1T-$TaSe_2$ Monolayers by Transmission Electron Microscopy. *Appl. Phys. Lett.* **2018**, *113*, 173103.

(9) Yamashita, S.; Koshiya, S.; Nagai, T.; Kikkawa, J.; Ishizuka, K.; Kimoto, K. Quantitative Annular Dark-Field Imaging of Single-Layer Graphene—II: Atomic-Resolution Image Contrast. *Microscopy* **2015**, *64*, 409–418.

(10) Okumura, T.; Tamura, K.; Fujii, E.; Yamada, H.; Kogure, T. Direct Observation of Cesium at the Interlayer Region in Phlogopite Mica. *Microscopy* **2014**, *63*, 65–72.

(11) Kogure, T.; Murakami, T. Direct Identification of Biotite/Vermiculite Layers in Hydrobiotite Using High-Resolution TEM. *Mineral. J.* **1996**, *18*, 131–137.

(12) Beall, G. W.; Powell, C. E. *Fundamentals of Polymer–Clay Nanocomposites*; Cambridge University Press.: Cambridge, 2011.

(13) Chen, B.; Evans, J. R. G.; Greenwell, H. C.; Boulet, P.; Coveney, P. V; Bowden, A. A.; Whiting, A. A Critical Appraisal of Polymer–Clay Nanocomposites. *Chem. Soc. Rev.* **2008**, *37*, 568–594.

(14) Sanchez, C.; Belleville, P.; Popall, M.; Nicole, L. Applications of Advanced Hybrid Organic–Inorganic Nanomaterials: From Laboratory to Market. *Chem. Soc. Rev.* **2011**, *40*, 696–753.

(15) Okada, T.; Ide, Y.; Ogawa, M. Organic-Inorganic Hybrids Based on Ultrathin Oxide Layers: Designed Nanostructures for Molecular Recognition. *Chem. Asian J.* **2012**, *7*, 1980–1992.

(16) López Arbeloa, F.; Martínez Martínez, V.; Arbeloa, T.; López Arbeloa, I. Photoresponse and Anisotropy of Rhodamine Dye Intercalated in Ordered Clay Layered Films. *J. Photochem. Photobiol. C Photochem. Rev.* **2007**, *8*, 85–108.
(17) Thomas, J. K. Physical Aspects of Photochemistry and Radiation Chemistry of Molecules Adsorbed on SiO_2, γ-Al_2O_3, Zeolites, and Clays. *Chew. Rev* **1993**, *93*, 301–320.
(18) Barthel, J. Dr. Probe: A Software for High-Resolution STEM Image Simulation. *Ultramicroscopy* **2018**, *193*, 1–11.
(19) Gražulis, S.; Chateigner, D.; Downs, R. T.; Yokochi, A. F. T.; Quiró, M.; Lutterotti, L.; Manakova, E.; Butkus, J.; Moeck, P.; Le Bail, A. Crystallography Open Database-an Open-Access Collection of Crystal Structures. *J. Appl. Cryst.* **2009**, *42*, 726–729.
(20) *The X-Ray Identification and Crystal Structures of Clay Minerals*; Brown, G., Ed.; Mineralogical Society, Clay Minerals Group: London, 1961.
(21) Kogure, T. Imaging of Dioctahedral 2:1 Layers by High-Resolution Transmission Electron Microscopy (HRTEM): Possibility of Recording the Dehydroxylate. *Am. Mineral.* **2007**, *92*, 1368–1373.
(22) Kogure, T.; Okunishi, E. Cs-Corrected HAADF-STEM Imaging of Silicate Minerals. *J. Electron Microsc. (Tokyo).* **2010**, *59*, 263–271.
(23) Csencsits, R.; Gronsky, R. Damage of Zeolite Y in the TEM and Its Effects on TEM Images. *Ultramicroscopy* **1987**, *23*, 421–431.
(24) Robertson, I. D. M.; Eggleton, R. A. Weathering of Granitic Muscovite to Kaolinite and Halloysite and of Plagioclase-Derived Kaolinite to Halloysite. *Clays Clay Miner.* **1991**, *39*, 113–126.
(25) Jiang, N. Electron Beam Damage in Oxides: A Review. *Reports Prog. Phys.* **2015**, *79*, 016501.
(26) Egerton, R. F. Radiation Damage to Organic and Inorganic Specimens in the TEM. *Micron* **2019**, *119*, 72–87.
(27) Cazaux, J. Correlations between Ionization Radiation Effects in Transmission Electron. *Ultramicroscopy* **1995**, *60*, 41–425.
(28) Drits, V. A.; Besson, G.; Muller, F. An Improved Model for Structural Transformations of Heat-Treated Aluminous Dioctahedral 2:1 Layer Silicates. *Clays Clay Miner.* **1995**, *43*, 718–731.

Chapter 4

Distinctive Stability of Free-standing Monolayer Clay Mineral Nanosheet under Transmission Electron Microscopy

4.1 Introduction

In previous section we demonstrated the atomic-scale imaging of a free-standing (i.e., without any surfactants or supporting matrices) monolayer clay mineral by annular dark-field (ADF) STEM.[1,2] The monolayer clay mineral was observed at the atomic-scale without any destruction, although bulk clay minerals are generally sensitive to the electron beam irradiation, as reported for cross-sectional imaging at the atomic-scale via (S)TEM.[3–7] In this section, we demonstrate the outstanding stability of free-standing monolayer clay mineral by comparing the decrease of selected area electron diffraction (SAED) intensity against those of the two- or three-layered (2L or 3L) clay mineral. The critical dose was determined as the point at which the electron diffraction intensities were reduced to 1/e (corresponding to 37% reduction) of its initial value. In addition to the fascinating property of clay mineral as itself, clay mineral nanosheets can serve as a simple model for considering beam-damage mechanisms in oxide nanosheets without using any surfactants that are commonly required for many 2D materials in their synthetic or exfoliation processes.[8,9] The results here revealed the crucial effect of interlayer spaces to the beam damage mechanism rather than the thickness among a few layers of clay

mineral, which can also be useful for understanding the electron beam damage to a wide variety of nanomaterials that are strongly hydrated.

4.2 Experimental section

Sample preparation

Montmorillonite (Mt), a typical anionic clay mineral, was acquired from Kunimine Industries (Kunipia F with the chemical structure corresponding to $Na_{0.35}K_{0.01}Ca_{0.06}(Al_{1.56}Mg_{0.33}Fe_{0.09}Ti_{0.01})(Si_{3.87}Al_{0.13})O_{10}(OH)_2$ and the cation exchange capacity of 1.19 meq. g^{-1}) [10,11] and was purified using the following procedure. First, raw clay mineral dispersion (300 mL, 10 g L^{-1}) was placed in centrifuge bottles, which were then centrifuged at a rotation speed of 7000 rpm for 15 min. The obtained supernatant was collected and poured into a container with 1500 mL of ethanol. After 1 h of mixing at a temperature of 70 °C, the resulting colloidal solution was filtered using a PTFE membrane with a pore size of 0.1 μm (Millipore). The produced cake was collected and dried under vacuum by rotary pump overnight. The dried cake was dispersed in water, and the dispersion was stored overnight to achieve complete exfoliation into nanosheets. A specimen for STEM/TEM was prepared by drop casting the aqueous solution of monolayer Mt on a holey carbon-coated Cu grid.

ADF–STEM observation

For the STEM observations for determination of the layer number, a Titan Cubed G2 equipped with spherical aberration correctors was used at an acceleration voltage of 300 kV. The convergence semi-angle of the incident probe was 21.4 mrad. The inner and

outer detection semi-angle of ADF detector were 31.4 and 192 mrad, respectively. The incident probe current was set to ~30 pA.

Time series of TEM–SAED

TEM–SAED observation was performed by using the Titan Cubed G2 at an acceleration voltage of 300 kV. The dose rate was set to 10 e^{-} $Å^{-2}$ s^{-1} by monitoring the screen current and the exposure time was 3s for each image acquisition. Note that there is no calibration from the screen current to the actual number of electrons.

4.3 Results and Discussion

4.3.1 Determination of the stacking number of free-standing Mt nanosheet by ADF−STEM observation.

The atomic structure of the unit layer structure for typical monolayer montmorillonite (1L Mt) is shown in Figure 1a. The unit layer comprises 2:1 combination of tetrahedral silica and octahedral aluminum hydroxide sheets. The general chemical formula of the layered aluminosilicates, such as Mt, mica, and pyrophyllite, is $[Si_4O_8][Al_2O_2(OH)_2]$. Two-thirds of the oxygen atoms in the octahedral sheet are supplied by silica tetrahedra, and the others are supplied by hydroxyl groups (indicated as yellow spheres in Figure 1a). The isomorphous substitution of Al^{3+} to Mg^{2+} in the octahedral sheet produces anionic charges within the Mt structure. Figure 1b shows the ADF−STEM image of the free-standing Mt nanosheets on a holey carbon film at low magnification. The acceleration voltage and the incident probe current were 300 kV and ~30 pA, respectively. The free-standing Mt sample was prepared by pouring an aqueous dispersion

of the exfoliated monolayer Mt onto a holey carbon- coated Cu grid. As shown in Figure 1b, the free- standing Mt nanosheets were stacked horizontally. Hence, the electron beam was irradiated in a direction normal to the surface. The stacking number of the Mt nanosheets, ranging from 1L to 3L, was determined by the difference between their contrasts, as previously reported (Figure 1b).[1] To further analyze the stability of free-standing Mt under electron beam irradiation, we determined the critical doses of 1L, 2L, and 3L Mt from the intensity reduction in their SAED patterns. Note that free-standing Mt , especially 1L Mt, were difficult to find in normal TEM, due to the ultrathin structure consisted with light elements. Therefore, the stacking number of Mt was determined via ADF−STEM, where the contrast positively correlated with the atomic number or thickness of the specimen.[1]

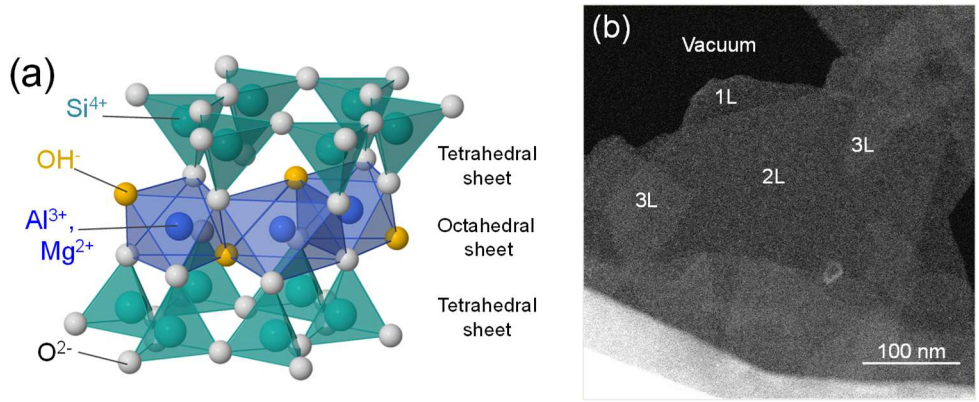

Figure 1. (a) Atomic structure model for a unit layer of montmorillonite showing the octahedral alumina sheet sandwiched by two tetrahedral silica sheets. Hydrogen atoms at the tetrahedral sheet edge are omitted for clarity. (b) ADF−STEM image of free-standing Mt nanosheets deposited on a holey carbon grid, and the corresponding stacked-layer number from one (1L) to three (3L).

4.3.2 The critical dose of electron beam damage as a function of the layer number.

Figure 2 shows a series of SAED patterns for (a) 1L, (b) 2L, and (c) 3L Mt at initial exposure and cumulative electron doses of 3, 15, and 30 × 103 e^{-} $Å^{-2}$. The acceleration voltage and the dwell for each pattern were 300 kV and 3 s, respectively. For the 1L Mt shown in Figure 2a, the diffraction spots remained clearly visible even after significant exposure to electrons, approximately 30 × 10^3 e^{-} $Å^{-2}$. The in-plane distance (d) of 1L Mt was indicated by yellow lines. A yellow dashed line, corresponding to the d value of 2.36 Å, was observed only for 1L Mt. The d values summarized in Table 1 are in good agreement with the values of (*hk*0) facets reported elsewhere.[12–14] Figure 2b and c show series of SAED images for 2L and 3L Mt at initial exposure and cumulative electron doses of 3, 15, and 30 × 10^3 e^{-} $Å^{-2}$. The red and blue circles in Figure 2b denote diffraction from nanosheet I and II which was distinguished by comparing the pattern of 1L Mt nanosheet. Some of the spots corresponding to the d value of 1.76 Å in the two nanosheets were overlapped, and they were excluded from the intensity analysis discussed later. In contrast to the results of 1L Mt, the diffraction patterns of the 2L and 3L Mt nanosheets show an obvious change after a certain amount of exposure, from appearing as sharp spots to be blurred, indicating the loss of their crystallinity. The outer spots, corresponding to smaller atomic spacing such as 1.34 or 1.29 Å, reduced rapidly, indicating their sensitivity to the electron beam irradiation.

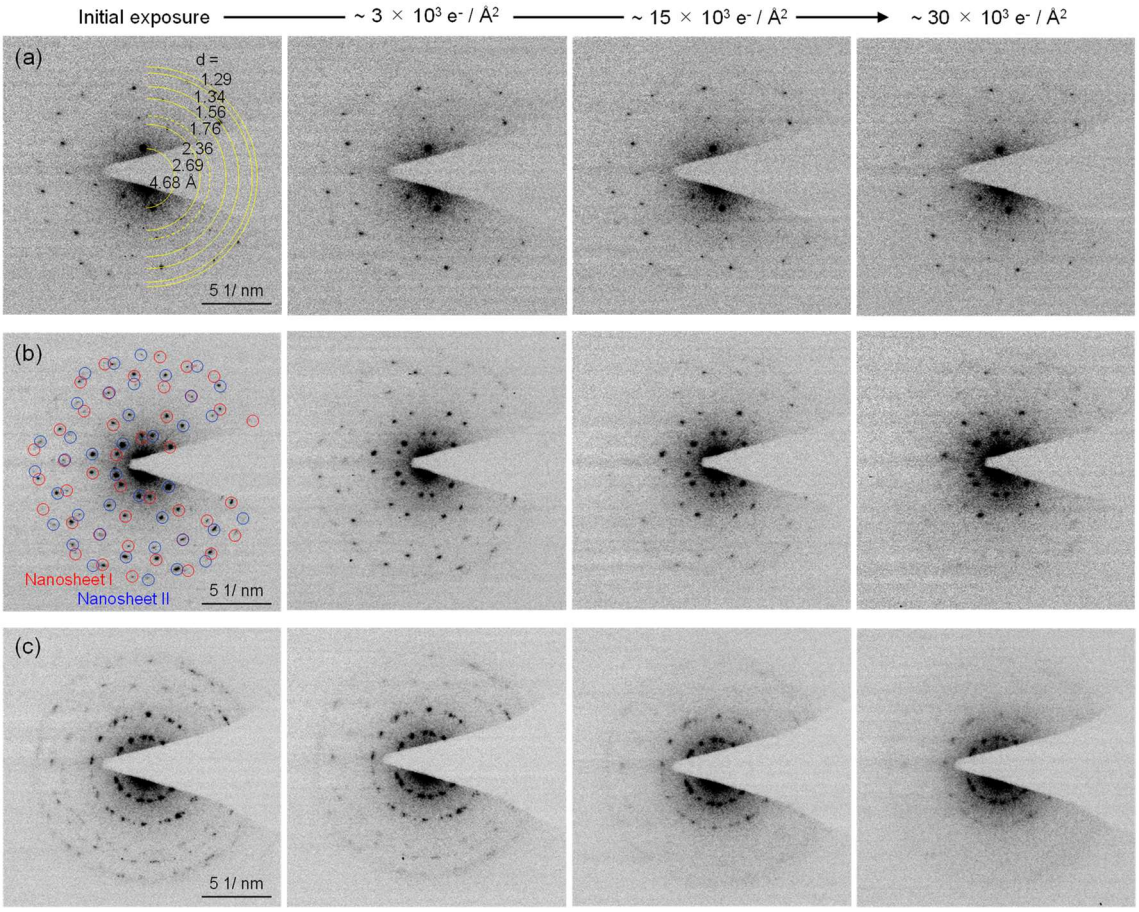

Figure 2. Series of SAED patterns for (a) monolayer (1L), (b) two-layered (2L), and (c) three-layered (3L) Mt at initial exposure and cumulative electron doses of 3, 15, and 30 × 10^3 e^- $Å^{-2}$. The acceleration voltage and the electron dose rate were 300 kV and 10 e^- $Å^{-2}$ s^{-1}, respectively. The dwell time for each pattern was set at 3 s. The in-plane distance (d) of 1L Mt was indicated by yellow lines in (a). Red and blue circles in panel b (left) denote diffraction from nanosheet I and II. Note that all the SAED patterns in the same line (a, b, and c) are scaled to the same display value range.

Table 1. The in-plane distance (d) of 1L Mt determined by SAED at initial exposure (Figure 2a, left). The d values are in good agreement with the values of (*hk*0) facets reported previously.[30]

(*hk*0)	d/Å
11, 02	4.68
13, 20	2.69
22, 04	2.36
31, 15, 24	1.76
33, 06	1.56
26, 40	1.34
35, 17, 42	1.29

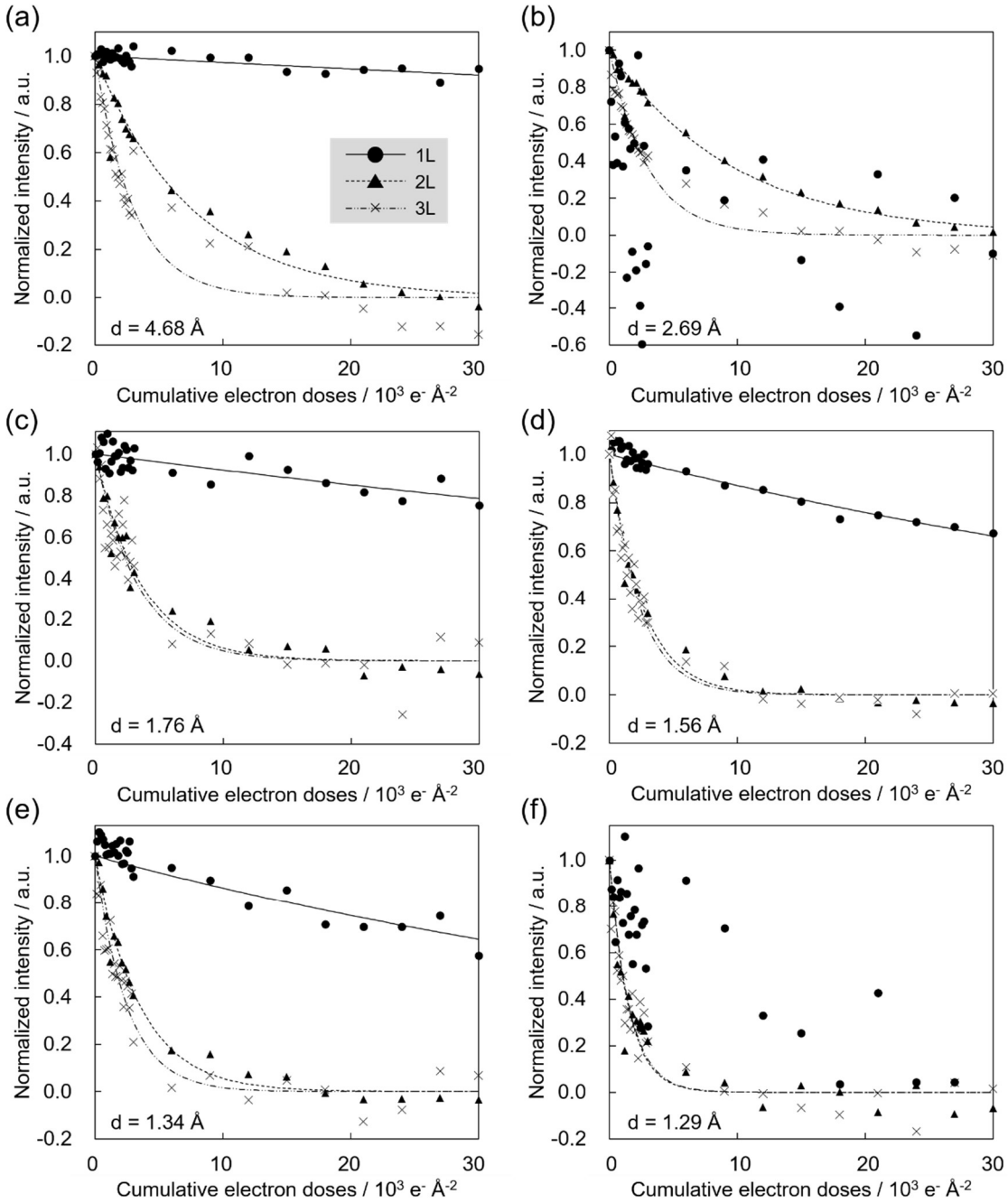

Figure 3. Relative intensity decay for the d-spacing of (a) 4.68, (b) 2.69, (c) 1.76, (d) 1.56, (e) 1.34, (f) 1.29 Å, corresponding to the diffraction from (11, 02); (13, 20); (31, 15, 24); (33, 06); (26, 40); and (35, 17, 42) facets as a function of the cumulative electron doses for 1L (●), 2L (▲), and 3L Mt (×), respectively. The acceleration voltage and the electron dose rate were 300 kV and 30 × 10^3 e^- $Å^{-2}$ s^{-1}, respectively.

Figure 3 shows normalized intensity decay for the d-spacing of (a) 4.68, (b) 2.69, (c) 1.76, (d) 1.56, (e) 1.34, (f) 1.29 Å, corresponding to the diffraction from (11, 02); (13, 20); (31, 15, 24); (33, 06); (26, 40); and (35, 17, 42) facets as a function of the cumulative electron doses for 1L (●), 2L (▲), 3L Mt (×), respectively. Black lines in Figure 3 indicate exponential decay curves determined by the least-squares method. The critical doses for each curve, determined as the point at which the electron diffraction intensities reduced to 1/e (corresponding to 37% reduction) of their initial value, are summarized in Table 2. Figure 3 was normalized to compare the critical doses of different stacked number of Mt nanosheets. An exponential approximation was first performed and the obtained constant term was set to zero, the data set was then normalized. Some negative values were found for the data set with a large variation relative to the absolute intensities. exponential approximation was first performed and the obtained constant term was set to zero, the data set was then normalized. Some negative values were found for the data set with a large variation relative to the absolute intensities. Note that normalization and exponential curve fitting for the d-spacing of 2.69 and 1.29 Å of 1L Mt was not performed correctly due to the large variation of the intensity. All critical doses for 1L Mt were significantly larger than those for 2L or 3L Mt ones. The critical dose for 2L Mt, however, was in the same order as that of 3L Mt. According to the results of 1L Mt the outer spots corresponding to smaller atomic spacing were reduced rapidly, indicating their sensitivity to the electron beam irradiation. For 2L and 3L Mt, the relationship between the critical dose and the d-spacing value was no longer observable. Additionally, Table 3 shows the critical doses for the two component nanosheets (noted as nanosheet I and II) in 2L Mt as indicated by red and blue circles in Figure 2b.

Table 2. The critical doses for 1L, 2L, 3L Mt, determined by exponential approximation in Figure 3.

	d / Å	Critical dose (10^3 e^- $Å^{-2}$)		
		1L	2L	3L
(a)	4.68	363.02	7.55	3.02
(b)	2.69	-	9.64	2.99
(c)	1.76	124.36	4.08	3.31
(d)	1.56	72.60	2.58	2.35
(e)	1.34	68.29	3.48	2.46
(f)	1.29	-	1.49	1.54

Table 3. The critical doses for the two component nanosheets (noted as nanosheet I and II) in 2L Mt as indicated by red and blue circles in Figure 2b. The values were determined by exponential approximation in Figure S1.

d / Å	Critical dose / (10^3 e^- $Å^{-2}$)	
	Nanosheet I	Nanosheet II
4.68	11.14	7.02
2.69	24.35	6.61
1.76	2.51	5.16
1.56	2.44	1.97
1.34	3.29	3.9
1.29	1.79	1.07

Since there was no significant difference in the critical dose of nanosheets I and II, the ordering between nanosheets I and II against the incident direction of electron beam could not be determined from SAED analysis (See Figure S1 in the Supplementary Information for the entire decay curves). These results clearly demonstrate that the free-standing 1L Mt nanosheet showed unexpected, distinct stability compared with 2L or more layered Mt under electron beam irradiation.

4.3.3 Mechanism of electron beam damage on Mt and the role of the interlayer space.

In free-standing Mt nanosheets during the TEM observation, multiple electron beam damage mechanisms can proceed simultaneously. The dominant mechanism of beam damage in insulating materials such as clay minerals is radiolysis damage caused by inelastic scattering—the transfer of energy from the incident electron to the electrons in the specimen. Other mechanism includes local heating or knock-on damage. The local heating also proceed the damage rate due to low thermal conductivity of clay minerals. Additionally, any hydrogens in the sample readily stripped by electron beam irradiation at the acceleration voltage of 300 kV, and the emitted hydrogens with high kinetic energy can cause knock-on damage in the structure.

Recently we demonstrated the stable ADF−STEM imaging of free-standing monolayer Mt at the atomic scale, and concluded that radiolysis damage were effectively suppressed due to the thin structure of the 1L Mt (0.96 nm) compared to the mean free path of secondary electrons in the oxides (ca. 10-20 nm).[15–17] Radiolysis damage is caused by secondary electrons produced by inelastic scattering, and the possibility of secondary electrons escaping from the sample surface into the vacuum depends on their depth from the surface.[15] Therefore, if the sample is an atomically thin film or small particulate matter,

the beam sensitivity decreases as the secondary electrons excited from near-surface atoms escape from the specimen to vacuum without causing damage.[16–18] The suppression of electron damage by lowering the dimension of the sample (from 3D to 2D or 1D) is becoming commonplace for direct imaging of beam-sensitive materials by electron microscopy.[18,19]

Note that since the escaped secondary electrons are not compensated by the neighboring electrons quickly in insulator, the specimen can be positively charged. For ionic materials such as clay minerals, this positive charge can induce an electric field in the specimen, which results in image drift or distortion, structural change, mass transport, or Coulomb explosion in some case. To avoid such explosive damage, we optimized the dose rate as 10 e^{-}Å^{-2} s^{-1}, which is mild condition that allows us to track the destruction process by SAED pattern. At high dose rate we could not get the fine SAED pattern even at the first scanning, which indicating the specimen was already destructed (See Figure S2 in the Supplementary Information). Such drastic destruction might be caused by Coulomb explosion at high dose rate.

In the present report, however, only the 1L Mt showed the remarkably high stability against to the electron beam irradiation, despite 2L and 3L samples being thin in comparison with the mean free path of secondary electrons.[15–17] Also, the critical doses for 2L and 3L Mt were of the same magnitude. According to the results, the absence of the interlayer space governs the difference in stability between 1L and multilayered Mt rather than the thickness. All surfaces in the 1L Mt were exposed to vacuum, whereas multilayered Mt included interlayer spaces (minimum of 4 Å under high vacuum [20,21]) as shown in Figure 4a and b, respectively.

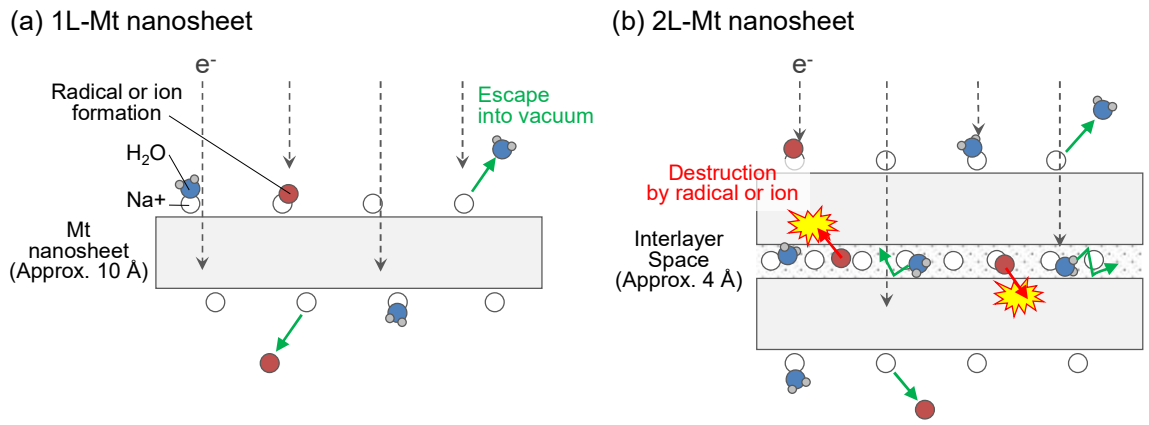

Figure 4. A plausible schematic illustration for the influence of the existence of the interlayer space on the destruction of (a) 1L and (b) 2L Mt, representing samples that include interlayer space.

Although multiple damage mechanism would proceed simultaneously as described above, the drastic difference of critical dose between 1L and 2L Mt can be plausibly explained by the effect of the interlayer space to hold water molecules. Generally, it is practically impossible to completely remove the water from clay minerals. Even after drying by heat or vacuum, certain amount of the water molecules remains in clay minerals due to their high activation energy for dehydration from counter cations under well-dried condition.[22–24] Kuligiewicz et al. demonstrated that the activation energy of dehydration for water molecules which coordinate the interlayer cations is 90–180 kJ/mol, while that for bulk water molecules in the interlayer, not directly coordinated to the interlayer cations, is 45–60 kJ/mol.[25] Note that the hydration number of sodium ion is decreased to 0.5-0.6 under well-dried condition.[25] When these water molecules irradiated by electron beam, excited water molecules, and other molecular species (i.e. $H^{\bullet}$, $OH^{\bullet}$, $HO_2^{\bullet}$, OH^-, H_3O^-, H_2, H_2O_2) are generated,[26,27] or desorption from the coordinated cations occurs. For the beam damage of zeolite, an aluminosilicate, the lower water content was

associated with higher stability during electron microscopy.[28,29] The generated ions or radical species decrease the strength of the Si-O or Al-O bonds, followed by a change in the structure. The same mechanism is true for the beam damage in clay minerals. During the observation in the experiment here, water molecules and the generated ions and radical species are hardly released from the interlayer spaces into the vacuum owing to the physical limitation of escape routes to the edges (Figure 4b); conversely, the same is easy in the monolayered sample, whose surfaces are completely exposed to vacuum, resulting in remarkable stability of 1L Mt. The results in Table 3, wherein nanosheets I and II in the 2L sample showed the same critical dose, indicate isotropic destruction from the interlayer space.

Furthermore, it is known that Al-OH in the octahedral site is relatively unstable, and dehydroxylation in the neighboring Al-OH sites and associated amorphization occurs in clay minerals under high temperature or irradiation.[25,30–32] The generated ions and radical species can pass through the six-membered rings of the Si-O tetrahedron and attack the Al-OH sites to promote dehydroxylation, and thus change the crystal structures. Although we were not able to distinguish the adjacent Si and Al atoms in monolayer Mt, ADF−STEM imaging may help monitor the evolution of the dehydroxylation process empirically, which has been previously studied only by thermogravimetry, X-ray diffraction, Fourier-transform infrared spectroscopy, or DFT calculations. [37,30,31]

4.5 Conclusions

In this section, we demonstrated the remarkable stability of free-standing monolayer Mt against the beam irradiation using electron diffraction technique, while 2L and 3L Mt showed similar low stabilities. The results suggested that the stability of 1L Mt was owing to the absence of interlayer space, as a site for hydration, rather than the thinness of the structure. Although complete dehydration of clay minerals was not achieved in the multilayered Mt, the monolayer Mt with entirely exposed surfaces to the vacuum enables the efficient release of water molecules imparting much less beam damage. Although we focused on Mt in this work as a good model for experimental demonstration owing to the moderate anionic charge density and the large particle size up to hundreds of nanometers, the results here can be applied for other clay minerals in principle because the hydration is a common phenomenon of clay minerals. The moderate anionic charge density of Mt eases the exfoliations into individual layers in aqueous dispersion, and relatively larger particle sizes (~ hundreds nm) that is comparable to the illuminated area in TEM have an advantage on avoiding the quick beam damage from edges of layers. Other common clay minerals such as mica (too high charge density) or saponite (sizes of only ~ tens nm) are therefore not the good model for this purpose. By using Mt we can thus focus on the dependence of electron beam damage on the layer number, i.e. the existence of the interlayer space for the first time. The findings here encourage further investigation using (S)TEM not only for the free-standing monolayer clay minerals but also for a wide variety of nanomaterials, such as the ones that are strongly hydrated in their interlayer spaces or nanopores.

4.4 Supporting information

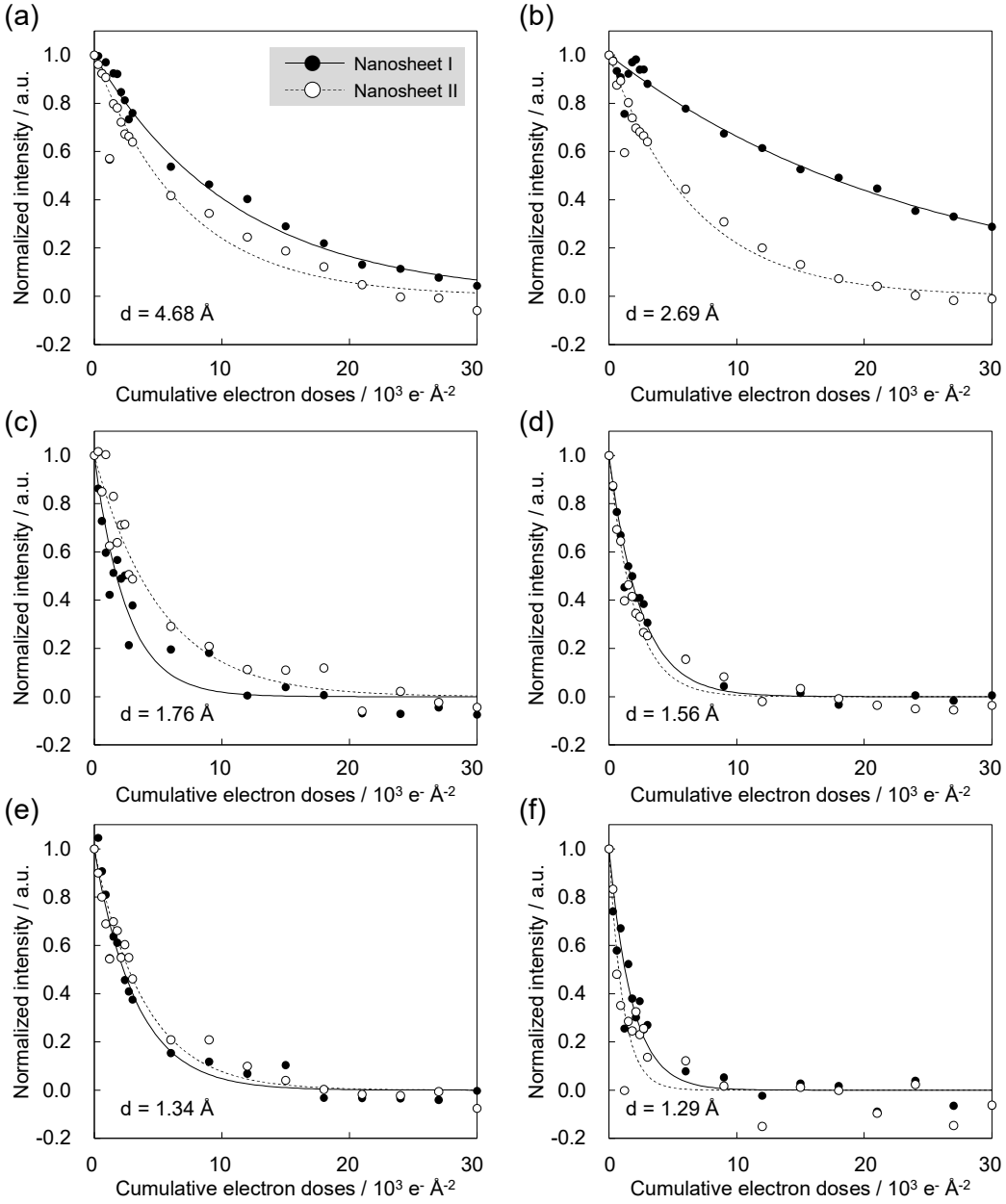

Figure S1. Relative intensity decay for the d-spacing of (a) 4.68, (b) 2.69, (c) 1.76, (d) 1.56, (e) 1.34, (f) 1.29 Å as a function of the cumulative electron doses for the two component nanosheets (noted as nanosheet I and II) in 2L Mt as indicated by red and blue circles in Figure 2b. Note that the value plotted in Figure 3 as 2L Mt is the average of the normalized intensity for nanosheet I and nanosheet II.

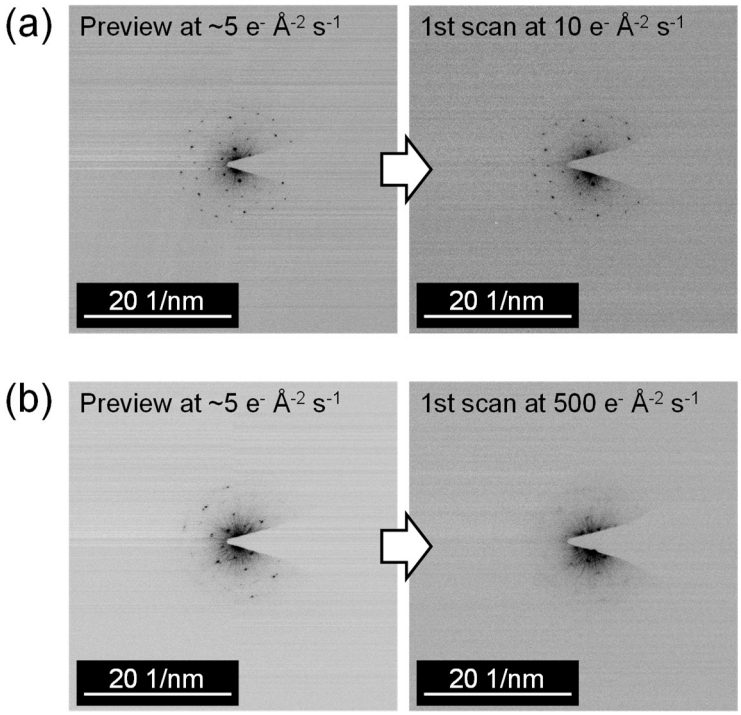

Figure S2. SAED patterns taken by 1st scanning at the dose rate of (a) 10 e^{-} $Å^{-2}$ s^{-1} and (b) 500 e^{-} $Å^{-2}$ s^{-1}. Preview SAED images shown together were taken at the low dose rate of ~5 e^{-} $Å^{-2}$ s^{-1} to ensure that the target area are initially crystalline. The exposure time for all the patterns were 3s.

4.6 References

(1) Akita, I.; Ishida, Y.; Yonezawa, T. Counting the Layer Number of Free-Standing Montmorillonite Nanosheets Using Annular Dark Field Scanning Transmission Electron Microscopy. *Clay Sci.* **2019**, *23*, 41–45.

(2) Akita, I.; Ishida, Y.; Yonezawa, T. Atomic-Scale Imaging of a Free-Standing Monolayer Clay Mineral Nanosheet Using Scanning Transmission Electron Microscopy. *J. Phys. Chem. Lett.* **2020**, *11*, 3357–3361.

(3) Okumura, T.; Tamura, K.; Fujii, E.; Yamada, H.; Kogure, T. Direct Observation of Cesium at the Interlayer Region in Phlogopite Mica. *Microscopy* **2014**, *63*, 65–72.

(4) Kogure, T.; Okunishi, E. Cs-Corrected HAADF-STEM Imaging of Silicate Minerals. *J. Electron Microsc. (Tokyo).* **2010**, *59*, 263–271.

(5) Kogure, T.; Murakami, T. Direct Identification of Biotite/Vermiculite Layers in Hydrobiotite Using High-Resolution TEM. *Mineral. J.* **1996**, *18*, 131–137.

(6) Kogure, T.; Jige, M.; Kameda, J.; Yamagishi, A.; Miyawaki, R.; Kitagawa, R. Stacking Structures in Pyrophyllite Revealed by High-Resolution Transmission Electron Microscopy (HRTEM). *Am. Mineral.* **2006**, *91*, 1293–1299.

(7) Robertson, I. D. M.; Eggleton, R. A. Weathering of Granitic Muscovite to Kaolinite and Halloysite and of Plagioclase-Derived Kaolinite to Halloysite. *Clays Clay Miner.* **1991**, *39*, 113–126.

(8) Tan, C.; Cao, X.; Wu, X. J.; He, Q.; Yang, J.; Zhang, X.; Chen, J.; Zhao, W.; Han, S.; Nam, G. H.; et al. Recent Advances in Ultrathin Two-Dimensional Nanomaterials. *Chem. Rev.* **2017**, *117*, 6225–6331.

(9) Roth, W. J.; Gil, B.; Makowski, W.; Marszalek, B.; Eliášová, P. Layer like Porous Materials with Hierarchical Structure. *Chem. Soc. Rev* **2016**, *45*, 3400–3438.

(10) Takahashi, T.; Ohkubo, T.; Suzuki, K.; Ikeda, Y. High Resolution Solid-State NMR Studies on Dissolution and Alteration of Na-Montmorillonite under Highly Alkaline Conditions. *Microporous Mesoporous Mater.* **2007**, *106*, 284–297.

(11) Seyama, H.; Soma, M. X-Ray Photoelectron and Auger Electron Spectroscopic Study of Mg-Montmorillonite. *Chem. Lett.* **1981**, *10*, 1009-1012.

(12) *The X-Ray Identification and Crystal Structures of Clay Minerals*; Brown, G., Ed.; Mineralogical Society, Clay Minerals Group: London, 1961.

(13) Środoń, J.; Drits, V. A.; Mccarty, D. K.; Hsieh, J. C. C.; Eberl, D. D. Quantitative X-Ray Diffraction Analysis of Clay-Bearing Rocks from Random Preparations. *Clays Clay Miner.* **2001**, *49*, 514–528.

(14) Rich, C. I. Determination of (060) Reflections of Clay Minerals by Means of Counter Type X-Ray Diffraction Instruments. *Am. Mineral.* **1957**, *42*, 569–570.

(15) Seiler, H. Secondary Electron Emission in the Scanning Electron Microscope. *J. Appl. Phys.* **1983**, *54*, R1.

(16) Jiang, N. Electron Beam Damage in Oxides: A Review. *Reports Prog. Phys.* **2015**, *79*, 016501.

(17) Egerton, R. F. Radiation Damage to Organic and Inorganic Specimens in the TEM. *Micron* **2019**, *119*, 72–87.

(18) Skowron, S. T.; Roberts, S. L.; Khlobystov, A. N.; Besley, E. The Effects of Encapsulation on Damage to Molecules by Electron Radiation. *Micron* **2019**, *120*, 96–103.
(19) Nakamura, E. Atomic-Resolution Transmission Electron Microscopic Movies for Study of Organic Molecules, Assemblies, and Reactions: The First 10 Years of Development. *Acc. Chem. Res.* **2017**, *50*, 1281–1292.
(20) Sato, T.; Watanabe, T.; Otsuka, R. Effects of Layer Charge, Charge Location, and Energy Change on Expansion Properties of Dioctahedral Smectites. *Clays Clay Miner.* **1992**, *40*, 103–113.
(21) Ferrage, E.; Lanson, B.; Sakharov, B. A.; Drits, V. A. Investigation of Smectite Hydration Properties by Modeling Experimental X-Ray Diffraction Patterns: Part I: Montmorillonite Hydration Properties. *Am. Mineral.* **2005**, *90*, 1358–1374.
(22) Mooney, R. W.; Keenan, A. G.; Wood, L. A. Adsorption of Water Vapor by Montmorillonite. II. Effect of Exchangeable Ions and Lattice Swelling as Measured by X-Ray Diffraction. *J. Am. Chem. Soc.* **1952**, *74*, 1371–1374.
(23) Środoń, J.; McCarty, K. D. Surface Area and Layer Charge of Smectite from CEC and EGME/H_2O-Retention Measurements. *Clays Clay Miner.* **2008**, *56*, 155–174.
(24) Schoonheydt, R. A.; Johnston, C. T. The Surface Properties of Clay Minerals. In *Layered Mineral Structures and their Application in Advanced Technologies*; Brigatti, M. F., Mottana, A., Eds.; Mineralogical Society of Great Britain and Ireland, 2011; Vol. 11, pp 337–373.
(25) Kuligiewicz, A.; Derkowski, A. Tightly Bound Water in Smectites. *Am. Mineral.* **2017**, *102*, 1073–1090.
(26) Swallow, A. J. *Radiation Chemistry; an Introduction*; Longman: London, 1973.
(27) Woehl, T. J.; Jungjohann, K. L.; Evans, J. E.; Arslan, I.; Ristenpart, W. D.; Browning, N. D. Experimental Procedures to Mitigate Electron Beam Induced Artifacts during in Situ Fluid Imaging of Nanomaterials. *Ultramicroscopy* **2013**, *127*, 53–63.
(28) Bursill, L. A.; Lodge, E. A.; Thomast, J. M. Zeolitic Structures as Revealed by High-Resolution Electron Microscopy. *Nature* **1980**, *286*, 111–113.
(29) Csencsits, R.; Gronsky, R. Damage of Zeolite Y in the TEM and Its Effects on TEM Images. *Ultramicroscopy* **1987**, *23*, 421–431.
(30) Allard, T.; Balan, E.; Calas, G.; Fourdrin, C.; Morichon, E.; Sorieul, S. Radiation-Induced Defects in Clay Minerals: A Review. *Nucl. Instrum. Meth. B* **2012**, *277*, 112–120.
(31) Fourdrin, C.; Allard, T.; Monnet, I.; Menguy, N.; Benedetti, M.; Calas, G. Effect of Radiation-Induced Amorphization on Smectite Dissolution. *Environ. Sci. Technol.* **2010**, *44*, 2509–2514.
(32) Kogure, T. Imaging of Dioctahedral 2:1 Layers by High-Resolution Transmission Electron Microscopy (HRTEM): Possibility of Recording the Dehydroxylate. *Am. Mineral.* **2007**, *92*, 1368–1373.

Chapter 5

Direct imaging of individual organic molecules in supramolecular assembly strongly fixed via multivalent electrostatic interactions

5.1 Introduction

Improved electron microscopic equipment and techniques for the precise control of low-dimensional nanomaterials[1–4] have led to advancements in the direct observation of single organic molecules and their supramolecular assemblies. Electron microscopy, including aberration corrected transmission electron microscopy (TEM) and scanning TEM (STEM), is the only atomic-scale imaging technique that allows for direct observation of the local structure of individual molecules with high spatio-temporal resolution.[5,6] Instead, conventional characterization methods for organic materials, such as optical spectroscopy and X-ray techniques, provide statistically averaged data based on a large number of molecules.

The isolation of organic molecules has been a key aspect of stable TEM and STEM research during the last two decades, where the much smaller secondary electron scattering cross-sections of these molecules result in less damage.[5–7] Electron beam damage is an issue particularly for the study of beam sensitive organic molecules and their assemblies and are typically suppressed using low acceleration voltages or low electron-dose conditions.[8–11] Macroscopic supporting materials are required for fixation

and isolation of the target molecules during stable TEM and STEM observation, as they prevent dropout, migration, and aggregation. The supporting material and target molecule should be distinguishable with a large contrast, where nanocarbon materials (e.g., graphene, carbon nanotubes, and fullerene) are the most commonly used supporting substrate. Several methods have been developed for the fixation of molecules to nanocarbon substrates, including encapsulation into graphene layers, carbon nanotubes, or fullerene, direct attachment via covalent bonding, and weak adsorption via non-covalent interactions (e.g., van der Waals or π-π interactions).[5,6,12–14] High-resolution TEM (HRTEM) can be used to visualize an entire molecular framework,[5,7] while high-angle annular dark field (ADF) STEM captures heavy metal atom markers (e.g., Pt,[13] Cu,[14] Ru,[15] and W[16]) coordinated within the molecule. These heavy metal atom markers exhibit bright contrast in ADF-STEM, which allows for visualization of single molecules on a host material with a more complex structure than graphene analogs with a single atom thickness. Organic molecules in supramolecular assemblies based on non-covalent interactions exhibit a flexible and non-periodic structure that is easily affected by the dropout, migration, or aggregation of the molecules under electron beam irradiation. Thus, TEM and STEM analysis of these organic molecules remains a challenge.

The use of anionic charged clay mineral nanosheets as a host material for a supramolecular assembly of well-isolated organic molecules has been investigated to prevent aggregation via multivalent electrostatic interactions.[17] These clay mineral nanosheets are a 2D nanomaterial with a thickness of *ca*. 1 nm, and can be obtained by exfoliating clay minerals, which is a layered aluminosilicate. There are many types of clay minerals, where the smectite group (e.g., saponite and montmorillonite) is widely used owing to its unique characteristics, including moderate anionic charge density,

exfoliation to individual nanosheets (or stacking thereof) in aqueous solutions, and optical transparency of smaller exfoliated particles in visible light.[17–20] The general chemical formula of smectite is $[(Si_{8-x}Al_x)(Mg_{6-y}Al_y)O_{20}(OH)_4]\cdot(x-y)Y^+$, where Y represents the balancing cations that compensate for the anionic charge (Figure 1). A completely exfoliated clay mineral (i.e., monolayer) can thus be defined as a family of 2D nanosheets.

Stable atomic-scale imaging of monolayer clay mineral nanosheets via ADF-STEM was recently reported for the first time by the current authors.[21,22] The present study aimed to directly image single organic molecules and supramolecular assemblies on monolayer clay mineral nanosheets using heavy metal atom markers. Electrostatic interactions are a weak non-covalent interaction, and enabled strong fixation of each organic molecule on the ionic 2D nanosheet supports. The local information obtained via electron microscopy using the proposed approach was complemented with averaged information from spectroscopic analysis to correlate the structural characteristics and properties or functionalities of individual molecular species during characterization.

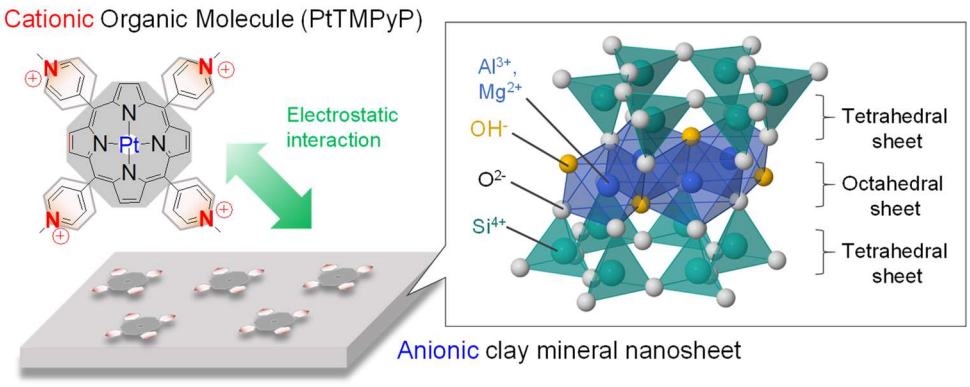

Figure 1. Schematic illustrations of a supramolecular assembly based on multivalent electrostatic interactions between the anionic clay mineral nanosheet and cationic organic molecule (PtTMPyP) (left), and the unit structure of the monolayer clay mineral nanosheet (montmorillonite) (right).

5.2 Experimental section

Specimen preparation

Montmorillonite is a typical anionic clay mineral and was acquired from Kunimine Industries (Kunipia F). The chemical structure of montmorillonite corresponded to the formula $Na_{0.66}(Al_{3.34}Mg_{0.66})Si_8O_{20}(OH)_4$ with a cation exchange capacity (CEC) of 1.19 meq g^{-1}. The montmorillonite was purified by preparing a raw clay dispersion (300 mL, 10 g L^{-1}) in centrifuge bottles, which was centrifuged at a rotation speed of 7000 rpm for 15 min. The supernatant was collected, poured into a container with 1500 mL ethanol, and mixed for 1 h at 70 °C. The resulting colloidal solution was filtered through a polytetrafluoroethylene (PTFE) membrane with a pore size of 0.1 μm (Millipore). The solids were collected and dried under vacuum in a rotary pump overnight. The dried solids were dispersed in ultrapure water and stored overnight for complete exfoliation into nanosheets. Pt(II) tetrakis(1-methylpyridinium-4-yl) porphyrin chloride (PtTMPyP; Frontier Scientific) was dissolved in ultrapure water. The water content of the clay and PtTMPyP was determined via thermogravimetry and differential thermal analysis (TG-DTA) using a thermogravimetry analyzer (TGA, Shimadzu DTG60H) before preparing the aqueous solutions.

Characterization

The PtTMPyP-clay assemblies were prepared by mixing the aqueous solutions of clay and PtTMPyP. The saturated concentration for monomer adsorption was determined based on the ultraviolet-visible (UV-vis) adsorption spectra on a series of samples with known loading levels of PtTMPyP vs. CEC of clay ranging from 10% to

160 (UV-1800; SHIMADZU). The STEM/TEM specimens were prepared by drop-casting the water dispersion of PtTMPyP-clay on a perforated carbon-coated Cu grid. STEM analysis was conducted using a JEM-ARM200F (JEOL) equipped with spherical aberration correctors at an acceleration voltage of 80 kV and camera length of 100 mm. The probe size was set to 8C with a condenser lens aperture of 30 μm (CL2) in size. The convergence semi-angle of the incident probe was 13.8 mrad, and the inner and outer detection semi-angles of the ADF detector were 54 and 220 mrad, respectively. Fourier transform was performed using the DigitalMicrograph (Gatan).

5.3 Results and discussion

5.3.1 Monomeric adsorption of cationic molecules on anionic clay mineral nanosheet via multivalent electrostatic interactions.

The monomeric adsorption of PtTMPyP on the clay mineral nanosheets was confirmed using absorption spectroscopy, where the absorption spectra of the PtTMPyP aqueous solution (free molecules) and PtTMPyP-clay assembly dispersions are given in Figure 2a. The concentration of molecules on the clay mineral nanosheets was expressed as the loading level vs. the cation exchange capacity (CEC) of the clay, which is the ratio between the amount of cation charges of the molecule and the CEC of the clay mineral nanosheet. Specifically, a loading level of 100% vs. CEC of the clay indicated that the number of cationic sites in the guest adsorbed on the clay surface was the same as the number of anionic sites on the clay surface. The maximum absorption wavelengths of the Soret band were 401 nm for the free molecules and 422 nm for the molecules adsorbed on the sheet. This shift to the longer wavelengths upon adsorption on the sheet was

attributed to planarization of the methylpyridinium substituents with respect to the porphyrin core.[23] The Lambert–Beer plot of the absorbance at 401 and 422 nm against the loading level exhibited linearity at concentrations below 90%, indicating monomeric adsorption on the clay mineral nanosheet (Figure 2b). At concentrations above 90%, the spectra can be expressed based spectral fitting of two components for free PtTMPyP (λ_{max} = 401 nm) and adsorbed PtTMPyP on clay (λ_{max} = 422). Therefore, the excess PtTMPyP was in the bulk solution and did not undergo further deposition or aggregation on the clay mineral nanosheets. Accordingly, ADF-STEM samples were prepared at a saturated adsorption concentration of 90% (PtTMPyP90%-clay) as the optimal condition.

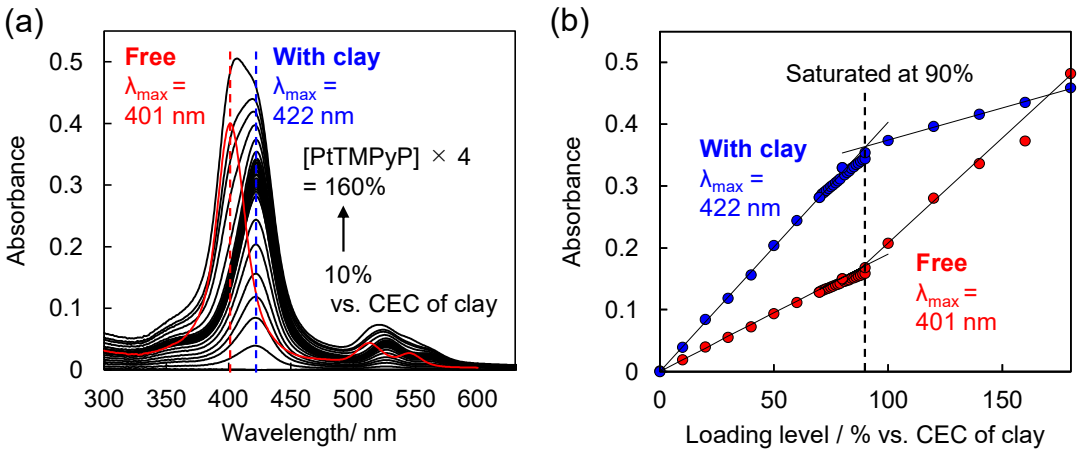

Figure 2. Spectral characterization of PtTMPyP-clay dispersion in water. (a) Absorption spectra of PtTMPyP-clay assemblies at various molecule loading levels up to 160% vs. CEC of clay in aqueous solution, where the maximum absorption wavelength of PtTMPyP in water (free) and adsorbed on clay mineral nanosheet (with clay) are 401 (red) and 422 nm (blue), respectively. (b) Lambert-Beer plots obtained from the absorption spectra at 401 (red) and 422 nm (blue).

5.3.2 ADF−STEM observation of PtTMPyP-clay mineral nanosheet assemblies.

ADF−STEM images of the PtTMPyP90%-clay assemblies were acquired at low and medium magnification corresponding to the pixel size of 0.25×0.25 and 0.04×0.04 nm^2 per pixel, respectively (Figure 3). The monolayer region was determined from the contrast difference in the low magnification observations (Figure 3a),[24] while uniform distribution of the Pt markers on the entire nanosheet surface was observed at medium magnification, where no segregation to the edge or interior of the sheets occurred (Figures 3b and c). The contrast and the number of Pt atoms increased as the number of layers was increased from one (1L) to three (3L). In addition to the bright contrast of the Pt atoms, the clay mineral nanosheets were observed stably and exhibited the characteristic periodic hexagonal contrast pattern of pristine clay mineral nanosheets.[21,22] These observations demonstrated that Pt atoms are a valid marker for ADF−STEM imaging of guest molecules assembled on a clay mineral nanosheet, as well as on simpler substrates such as graphene.[13–15] The Fourier transform (Figure 3d) corresponding to the medium magnification ADF-STEM image of the monolayer region (Figure 3c) revealed that the in-plane distance was similar to previously reported values for the (*hk*0) facet of montmorillonite.[25] This was confirmed in all observations, indicating that the crystal structure of the nanosheets remained intact after monomeric adsorption of PtTMPyP on the clay nanosheet substrates via multivalent electrostatic interaction. ADF−STEM images of PtTMPyP90%-clay were acquired at pixel time of 10, 15, and 20 μs at high magnification (1024×1024 pixels, 0.013×0.013 nm^2/pixel). Only the images acquired during the first scan have been discussed further to avoid including artifacts caused by the degradation of the clay mineral nanosheets by repeated scanning. The image focus was optimized in an additional region near the target region. The first scans in different

fields of view are given in Figures 4a to c. The Pt atom markers were observed stably, and no aggregation, migration, or dropout occurred, even at the atomic scale. A pixel time longer than 15 μs was optimal for distinguishing the periodical contrast of the clay mineral nanosheet and bright contrast of Pt atoms without significant streaking.

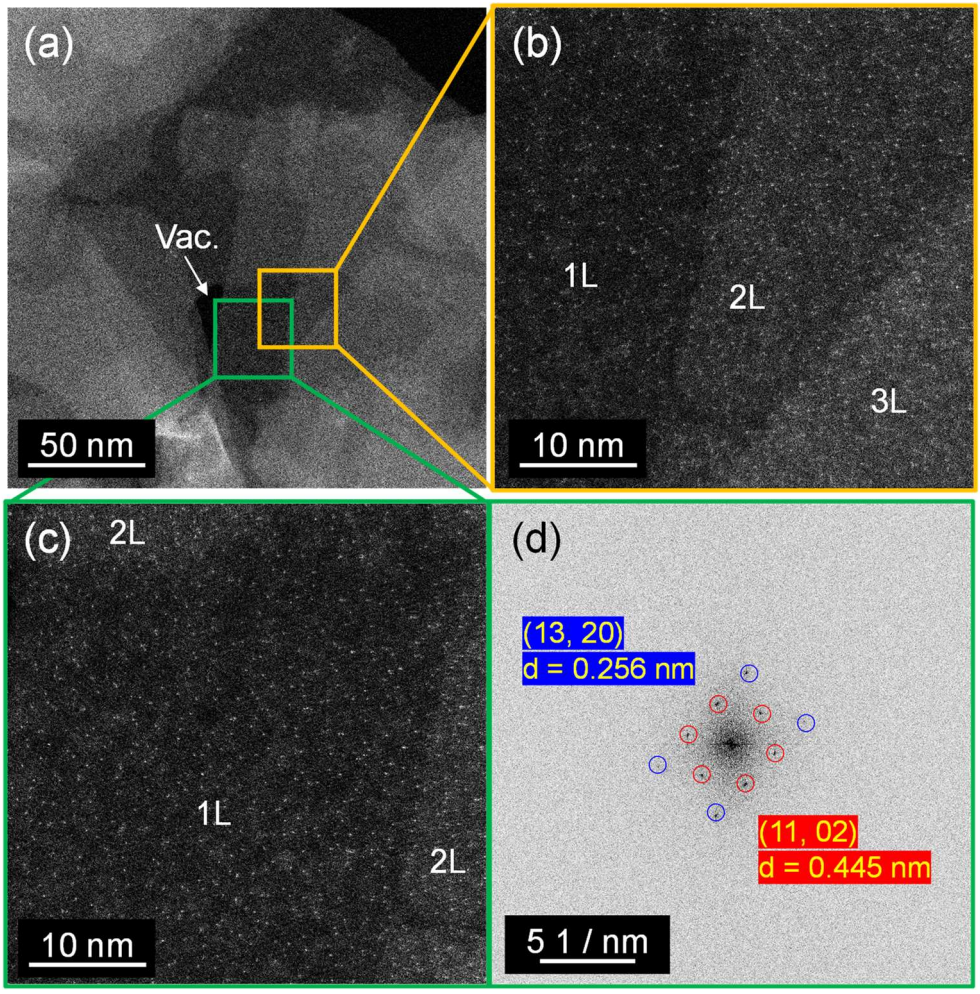

Figure 3. ADF−STEM images of PtTMPyP90%-clay at various magnifications. (a) Layer number from one (1L) to three (3L) was determined at low magnification (1024×1024 pixels, 0.25×0.25 nm^2/pixel, 20 μs/pixel). (b, c) Uniform dispersion of the Pt marker on monolayer clay mineral nanosheet of the green and orange regions at medium magnification (1024×1024 pixels, 0.04×0.04 nm^2/pixel, 20 μs/pixel). (d) Corresponding Fourier transform of the green area in inverted color.

The local loading level of PtTMPyP-clay was determined by dividing the area of the monolayer region by the number of Pt atoms in each field of view, as denoted in Figures 4a to c and Figure S1. The average loading level over the 16 fields of view was 87.5 ± 4.8%, which was in good agreement with the optimal preparation ratio of 90% determined by absorption spectroscopy (Figure 2). The occupied areas and corresponding ADF-STEM images are given in Table S1 and Figure S1. To the best of our knowledge, this is the first successful atomic-scale observation of a molecular assembly constructed via weak non-covalent interactions, where the observations corresponded well with the averaged spectroscopic data.

The direct observations were used to determine the individual intermolecular distances and relative conformations, which is not possible in conventional spectroscopic analyses. The histogram of the nearest-neighbor distance of each bright spot (i.e., the intermolecular distance of PtTMPyP) was shown in Figure S2a. The average intermolecular distance on the ADF-STEM projection of Figure 3c was 0.90 nm, which is much shorter than the diameter of the PtTMPyP molecule of 1.26 nm and the intermolecular distance of 1.65 nm assuming a uniform arrangement of the bright spots on the projection (Figure S2b and c). The diameter of PtTMPyP was determined as 1.26 nm using the semi-empirical molecular orbital method, where the cross-sectional area of the molecule was assumed to be circular.[26] Note that the existence of aggregation cannot be determined from only the intermolecular distance since three-dimensional information (i.e., 3D structure through the sheet) is compressed into 2D image on the ADF-STEM projection. The three-dimensional relative configuration of the molecules was, therefore, sorted into three groups by considering the number of neighboring bright spots as well as the intermolecular distance (Figure 4d). Circles with a diameter of 1.26 nm were

superimposed onto the center of the Pt atoms in the ADF−STEM image of PtTMPyP90%-clay acquired at a pixel time of 20 μs, where the circles were shaded blue, yellow or red depending on the state of the molecule (Figure 4d). The blue circles indicated a completely isolated molecule, where the distance from the nearest Pt marker was larger than 1.26 nm. The yellow circles indicated that the molecules were isolated as monomers when observed from the front and back through the clay mineral nanosheet, but the distance from the nearest Pt marker was less than 1.26 nm. Most of the Pt markers were assigned to this group. The red circles indicated Pt markers that could not be interpreted as monomers, as they occurred in a region in which three molecules overlapped. This migration was attributed to electron beam irradiation, and untangling did not occur during further scanning. The subsequent ADF-STEM images of PtTMPyP90%-clay are given in Figure S3. No obvious changes in the number and relative conformation of the Pt markers was observed during four times of repeated scanning, while the clay mineral nanosheets were gradually damaged with each scan. Note that dozens scans disrupted the relative conformation of the isolated Pt markers as the clay mineral nanosheet decomposed, but no significant desorption or aggregation of the markers was observed (Figure S4). The Pt markers exhibited excellent stability during ADF−STEM analysis compared to specimens prepared via simple physisorption. Specimens based on conventional substrates typically exhibit a low barrier for migration that allows for significant molecular motions on a shorter time scale than image capture.[6,27–29] Furthermore, Pt atoms physisorbed on clay mineral nanosheets, which were prepared by sputtering deposition, showed less stability during ADF−STEM observation (Figure S5). These unexpected results suggest strong fixation of PtTMPyP molecules via multivalent electrostatic interactions during the observation.

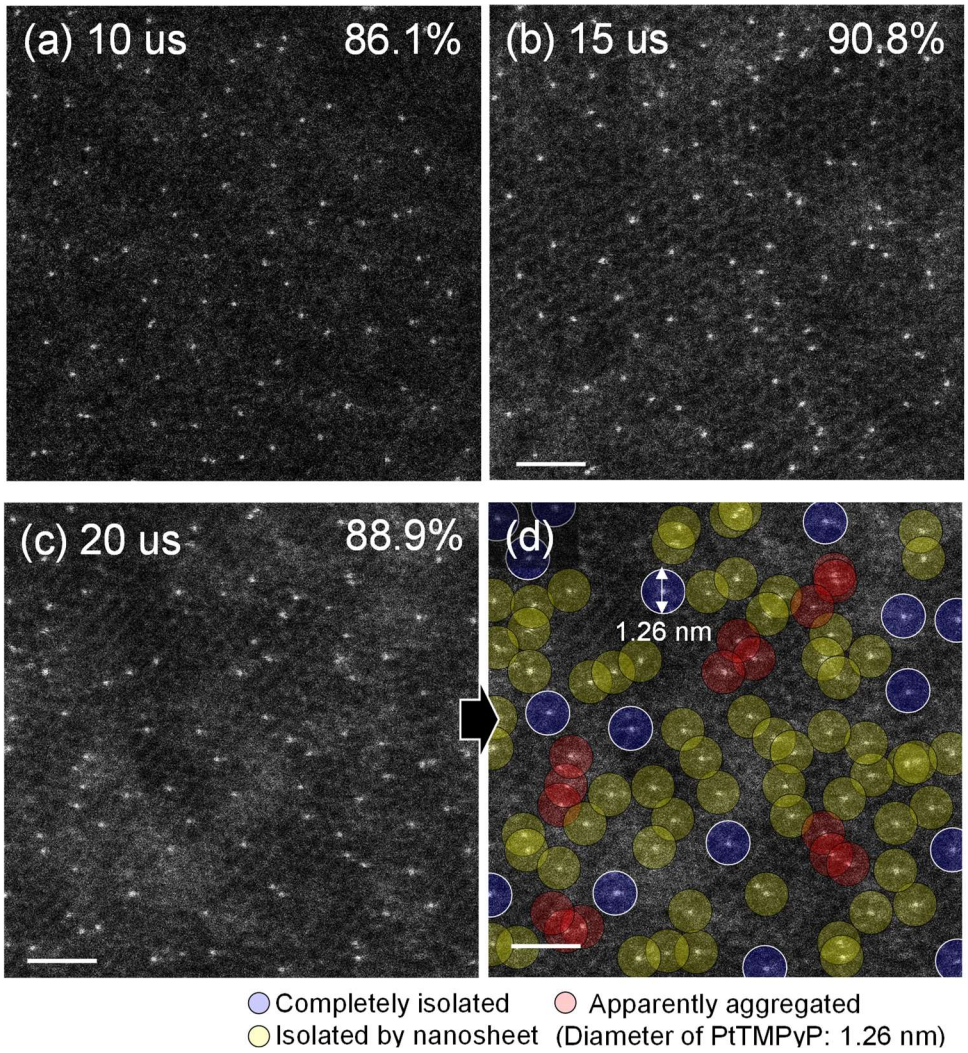

Figure 4. ADF−STEM images of PtTMPyP90%-clay acquired at high magnification at various pixel times. Images were acquired during the first scan in different fields of view, where pixel times included (a) 10, (b) 15, and (c) 20 μs (1024×1024 pixels, 0.013×0.013 nm^2/pixel). The percentages in each panel given the local loading level (area of the monolayer region divided by the number of Pt atoms). (d) Image acquired at a pixel time of 20 μs with the diameter of the PtTMPyP molecules (1.26 nm) superimposed onto the center of the Pt marker atoms. Scale bars = 2 nm.

It should be noted that hydrogen atoms are easily knocked on by electron beam irradiation, leading to cleavage of the C-H bonds and subsequent cross-linking between adjacent molecules during TEM and STEM analysis of molecular assemblies.[6,14] This cross-linking can lead to pseudo-stability of the heavy metal markers. Therefore, we confirmed that there was a low possibility of cross-linking at least between the molecules, since the completely independent molecules remained stable during several scans using specimens with a lower molecular density of 20% vs. CEC of clay to ensure a higher proportion of completely isolated PtTMPyP molecules (Figure 5). The overlaid circles shaded in the same manner as Figure 4d. However, the effect of molecular residues and the possibility of cross-linking between molecules and sheets cannot be discussed from this experiment, and thus further investigation is needed in this regard

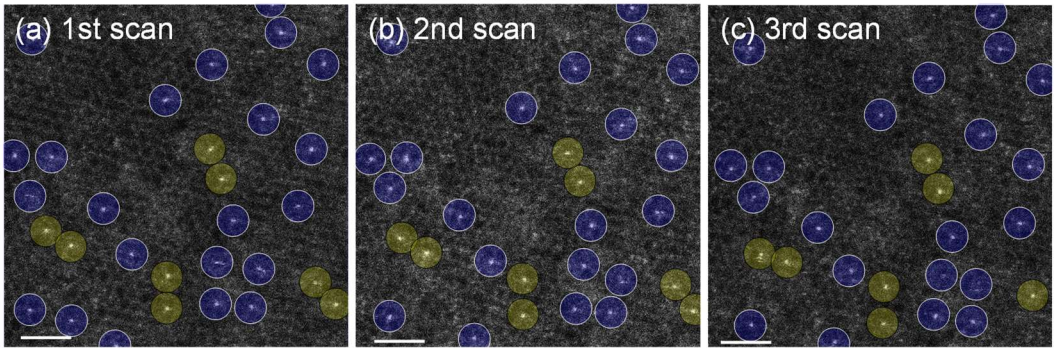

Figure 5. Stability of Pt markers during sequential ADF–STEM scanning. Sequential ADF−STEM images of PtTMPyP20%-clay continuously acquired during the (a) first, (b) second, and (c) third scans (1024×1024 pixels, ×15M, 0.013 nm^2/pixel, 20 μs/pixel), where the Pt markers were classified as either completely isolated (blue) or isolated by the clay mineral nanosheet (yellow) based on the diameter of PtTMPyP (1.26 nm). Dwell time of the image was 20.9 s. Scale bars = 2 nm.

5.3.3 Estimation of Coulombic attraction energy for multivalent electrostatic interaction.

The fixation of the molecules via multivalent electrostatic interactions in this system was evaluated based on the Coulombic attraction energy (V) as follows:

$$V = \alpha \frac{1}{r} \qquad (1)$$

$$\alpha = \frac{1}{4\pi\varepsilon\varepsilon_0} q_1 q_2 N_A \ (const) \qquad (2)$$

where r is the point-charge distance, ε is the relative permittivity, ε_0 is the permittivity of free space, q is the amount of charge, and N_A is the Avogadro constant. Determining the relative permittivity of the medium between the molecules and clay mineral nanosheets was challenging. Instead, an ε value of 1 was used during the calculations because moisture was mostly removed from the system during vacuum drying at 65 °C, and previously reported ε values of atomically thin two-dimensional materials are close to 1.[30–32] Assuming that a PtTMPyP molecule adsorbs on a monolayer clay mineral nanosheet, the Coulombic attraction energy (V_n; n = 1, 2, 3, or 4) between the four cationic charges of methylpyridinium substituents in PtTMPyP and the nearest four anionic charges of the clay surface were calculated. The Coulombic attraction energy of multivalent electrostatic interactions (V_{MEI}) was determined as follows:

$$V_{MEI} = V_1 + V_2 + V_3 + V_4$$

$$= \alpha \left(\frac{1}{r_1} + \frac{1}{r_2} + \frac{1}{r_3} + \frac{1}{r_4}\right) = \alpha \sum_{n=1}^{4} \frac{1}{r_n} \qquad (3)$$

The variable anion-cation distance (r_n) was determined based on several assumptions. The CEC (1.19 meq g^{-1}) and specific surface area (780 m^2 g^{-1}) of clay gives a surface anion charge density of 0.943 e^- nm^{-2}. Thus, assuming a hexagonal array, the distance between the anion charges in the plane direction was 1.11 nm. The intramolecular distance

between the cationic charges of PtTMPyP was calculated as 1.05 nm.[33] Further, assuming that the anion and cation charges were localized at the octahedral layer of the clay mineral nanosheet and at the nitrogen atom of the methylpyridinium substituent in PtTMPyP, the *z* height between the cation and anion charges was 7.4 Å. The *z* height of PtTMPyP on the clay mineral nanosheets was based on a dihedral angle between the porphyrin core and methylpyridinium substituents of 43°, which was chosen based on a previous report on structural minimization of metal-free TMPyP adsorbed on clay mineral nanosheets.[33] Consequently, the maximum and minimum Coulombic attraction energy per molecule under vacuum (STEM atmosphere) was calculated as 173 and 154 kcal mol^{-1} via the least-square method for variable *r*. The arrangements of PtTMPyP on clay mineral nanosheets corresponding to the maximum and minimum total Coulombic attraction energy are shown in Figure 6. Further, the anion-cation distance and Coulombic attraction energy between each of the four cation charges in a molecule and the nearest anion charge in the clay mineral nanosheets are given in Table S2. The high charge density of the clay mineral nanosheet sled to minimal location dependence of V_{MEI} (*ca*. 20 kcal in the above calculations). Thus, the molecules at all locations on the nanosheet are under a uniform influence of the Coulombic interactions. The order of magnitude of the maximum and minimum total Coulombic attraction energies was comparable to the dissociation energy of covalent bonds such as C–C and C=C bonds (83.65 and 146.03 kcal mol^{-1}, respectively). This was much larger than the dissociation energy of π−π or CH−π non-covalent interactions in graphemic materials (11.95 kcal mol^{-1})[28] or the maximum adsorption energy of Pt atoms on graphene is *ca*. 33 kcal mol^{-1} by DFT calculations.[34] The stable observation of molecular assemblies during ADF−STEM analysis was thus attributed to strong fixation via multivalent electrostatic interactions. This estimation is

based on many assumptions. For example, repulsion between neighboring molecules was ignored because the repulsive forces parallel to the *xy*-plane with the surrounding molecules cancel one another under very dense conditions, as was the case in 90% CEC adsorption.

The strong multivalent interaction and the dense charge of the nanosheets allowed the strong fixation of the adsorbed molecules at the initial location of adsorption, thereby preventing rearrangement on the surface. This result is in good agreement with a previous report that multi-cationic molecules strongly adsorb on the clay mineral nanosheet surface, and do not desorb in an aqueous dispersion.[20,35] The local adsorption density of the PtTMPyP20%-clay specimen varied widely from 0% to 55.5% due to mixing of the clay and molecule dispersions (Figure S6).[35] This phenomenon also led to the deviation of intermolecular distance in PtTMPyP90%-clay (Figure 4).

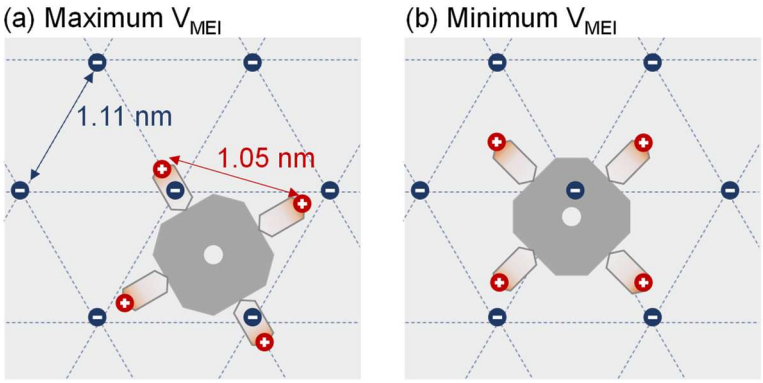

Figure 6. Schematic arrangement of PtTMPyP on clay mineral nanosheet. Arrangements at the (a) maximum and (b) minimum total Coulombic attraction energy of multivalent electrostatic interaction (V_{MEI}), where the average distance between the anion charges is 1.11 nm and the intramolecular distance between the cation charges of PtTMPyP is 1.05 nm.

5.4 Conclusion

In conclusion, strong fixation of organic molecules via multivalent electrostatic interactions enabled stable imaging of individual organic molecules in a supramolecular assembly on two-dimensional clay mineral nanosheets via electron microscopy. This approach facilitated visualization of the conformation of the individual molecules and assembly. Stable TEM and STEM imaging of organic molecules and supramolecular structures constructed via non- covalent interactions are crucial in the advancement of electron microscopic techniques. Common graphene-support based systems have limitations due to the small energy required to stabilize target molecules, but this strategy can be applied to a wide range of supramolecular systems consisting of various guest molecules and host materials. This approach is expected to widen the scope of atomic-scale imaging of organic molecules and assemblies.

5.5 Supporting information

Table S1. Occupied area per molecule and corresponding loading level based on ADF−STEM analysis.

Area	Occupied Area (nm^2)	Corresponding loading level (%) vs. CEC of clay
1	4.33	97.8
2	5.32	79.8
3	4.62	91.8
4	4.93	86.1
5	4.67	90.8
6	4.77	89.0
7	4.77	88.9
8	5.10	83.2
9	4.57	92.7
10	4.67	90.8
11	4.88	87.0
12	4.93	86.1
13	4.93	86.1
14	5.22	81.3
15	4.99	85.1
16	5.16	82.2
Average	4.86 ± 0.26	87.5 ± 4.8

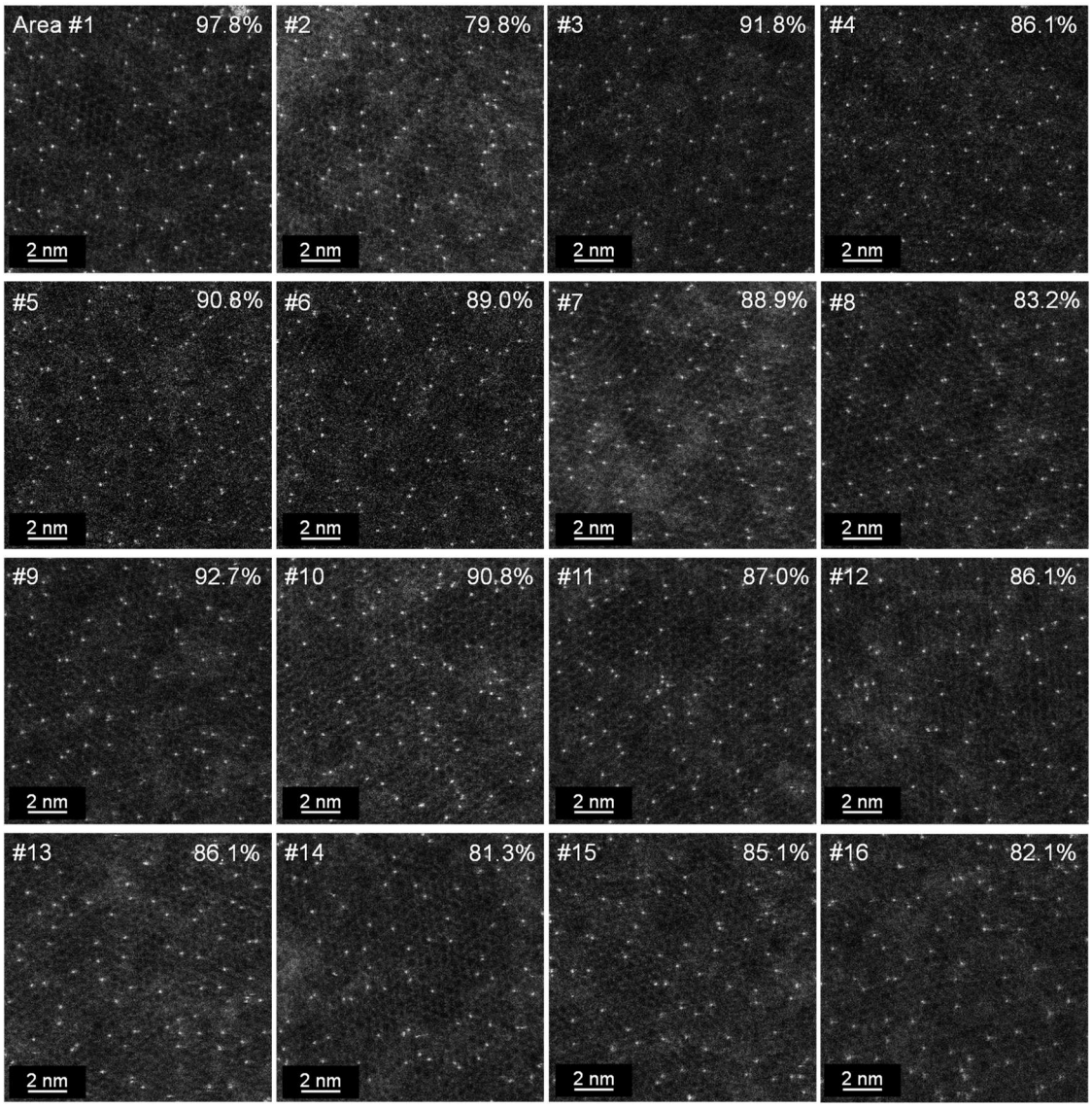

Figure S1. ADF−STEM images of PtTMPyP90%-clay used to determine adsorption density. The pixel time varied, where 20 μs was used for #1, 2, 7, 10, and 14, 15 μs was used for #8, 9, 15, and 16, and 10 μs was used for #3 and 4. The image size was 1024 × 1024 pixels, except for #5 and 6 with 512 × 512 pixels. The percentages in each panel give the local loading level of each field of view. The occupied area was based on a total area calculated by adding a 0.63 nm margin (radius PtTMPyP) to the monolayer region due to molecules at the edge of the field of view.

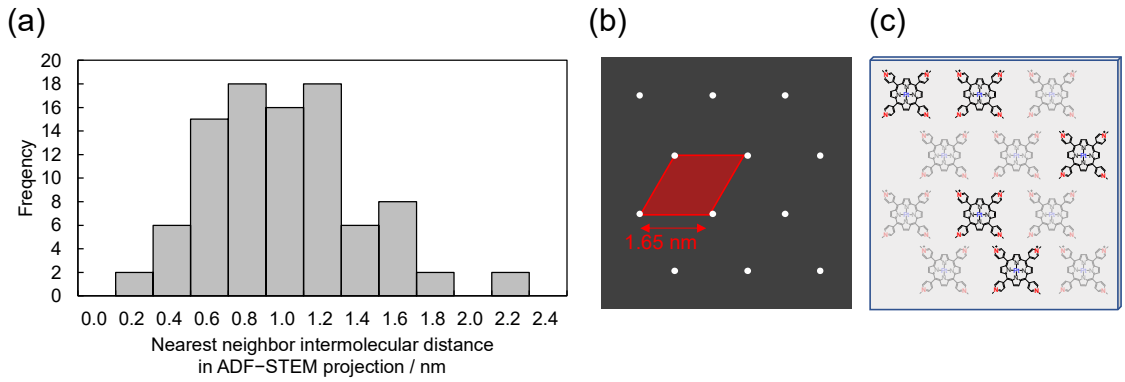

Figure S2. Analysis of the intermolecular distance for PtTMPyP90%-clay. (a) The histogram of nearest neighbor intermolecular distance determined from the ADF−STEM image in Figure 3c (N = 93). (b) An illustration showing that the averaged distance between Pt markers was 1.65 nm at the loading level of 90% on assumption of hexagonal array in ADF−STEM projection. Gray background and white dots are corresponding to the clay mineral nanosheet and Pt markers, respectively. (c) Representative configuration of PtTMPyP molecules on both sides of clay mineral nanosheet at the density corresponding to panel b. The molecules adsorbed on the back side of the figure are indicated by pale color.

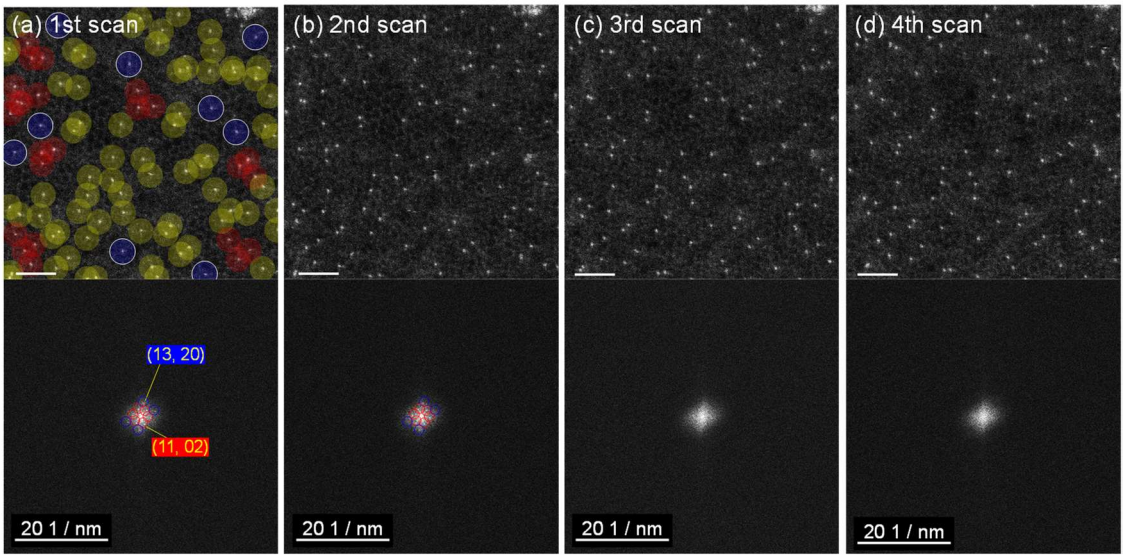

Figure S3. Sequential ADF−STEM images and corresponding FT patterns of PtTMPyP90%-clay from first to forth scan at high magnification (1024×1024 pixels, 0.013×0.013 nm^2/pixel, 20 μs/ pixel). Pt markers were circled according to the diameter of PtTMPyP (1.26 nm) and shaded blue, yellow or red depending on the state of the molecule. Scale bar = 2 nm.

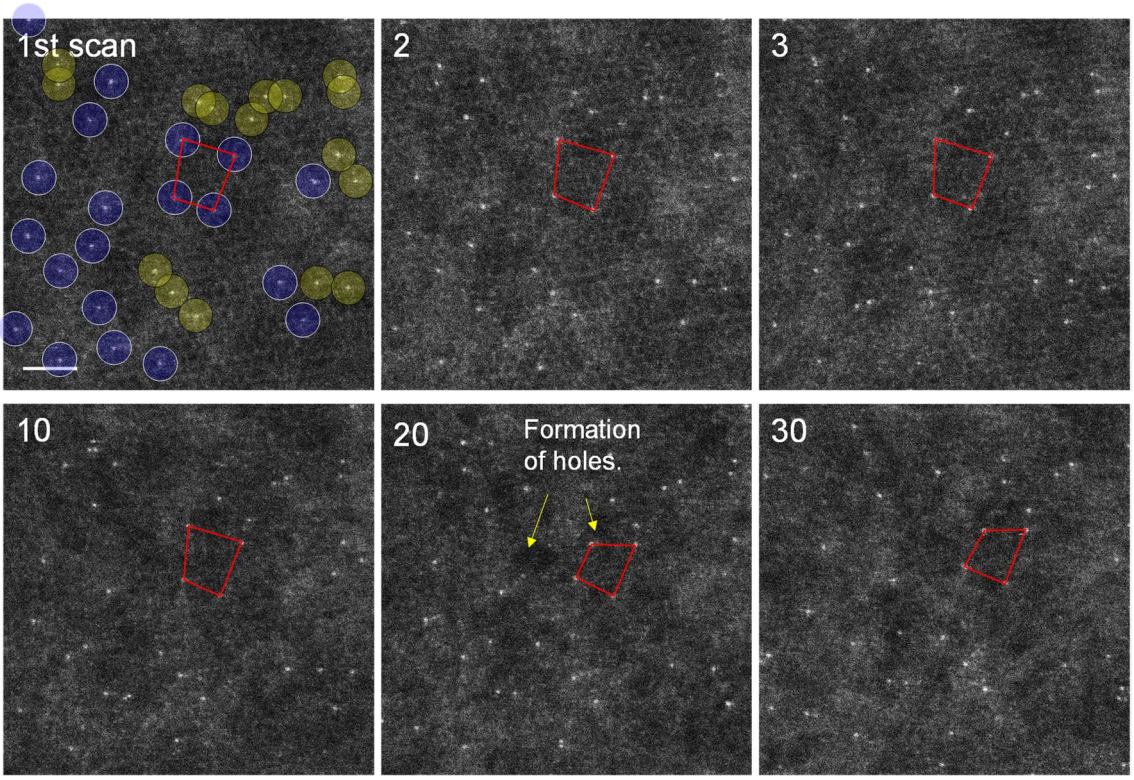

Figure S4. Sequential ADF−STEM images of PtTMPyP20%-clay from first to thirties scans at high magnification (1024×1024 pixels, 0.013×0.013 nm^2/pixel, 20 μs/ pixel). Pt markers were circled according to the diameter of PtTMPyP (1.26 nm) and shaded blue, yellow or red depending on the state of the molecule. Scale bar = 2 nm. The red squares are landmarks of the relative conformation of representative completely independent Pt markers. The relative conformation was changed obviously around the holes of clay mineral nanosheet that formed after *ca.* 20 scans.

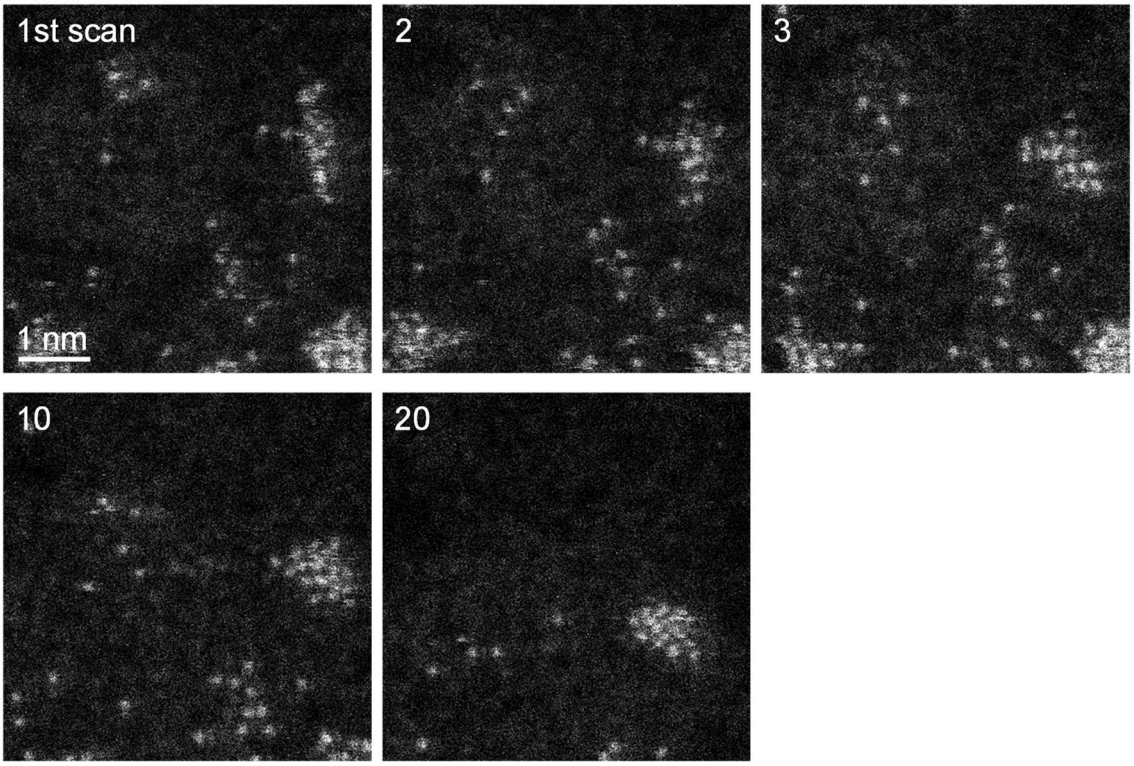

Figure S5. Sequential ADF−STEM images of physisorbed Pt atoms on clay mineral nanosheet from first to twenties scans at high magnification. The configuration of Pt single atoms or the shape of Pt clusters changed significantly from scan to scan compared to the case of the supramolecular assemblies via electrostatic interactions (Figure 5 in the main text). The specimen was prepared by the following procedure. First, the aqueous solution of clay mineral nanosheet was drop casted on a holey carbon coated Cu grid. After heating and vacuum drying the prepared grid at 65°C overnight, sputtering deposition of Pt was conducted with the custom-designed magnetron sputtering instrument based on MSP-10 (Shinkuu Device). The sputtering deposition was carried out for 1s at a current of 10 mA under 2 Pa of Ar in the chamber.

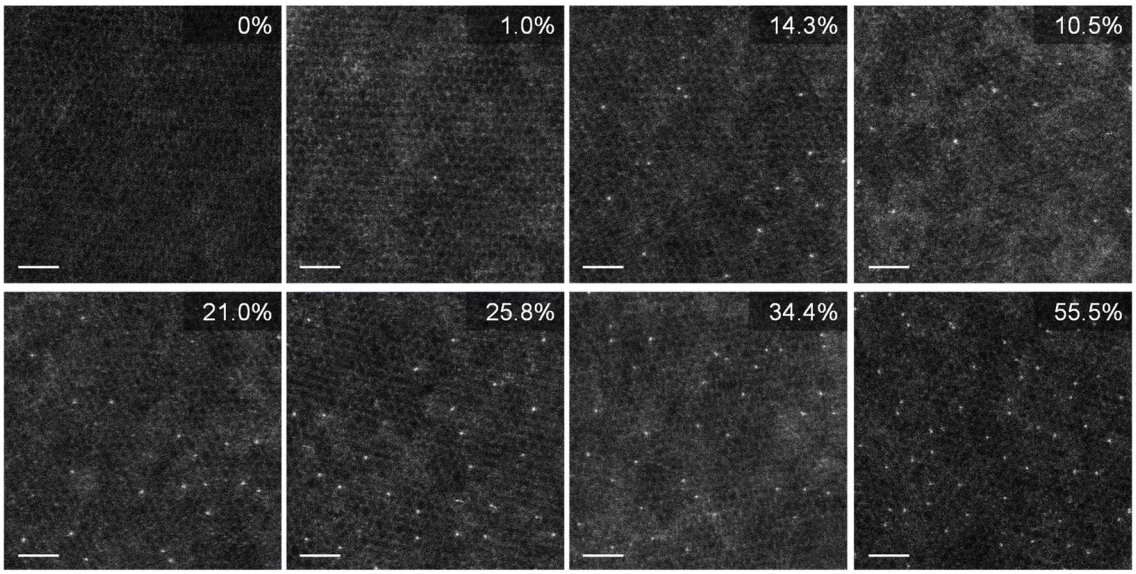

Figure S6. Representative ADF−STEM images of PtTMPyP20%-clay at varying local adsorption densities of PtTMPyP (1024×1024 pixels, 0.013×0.013 nm^2/pixel, 20 μs/pixel). Each image is the first scans in a certain fields of view, where the percentages in each panel give the local loading level of each field of view as calculated from experimental ADF−STEM images. Scale bar = 2 nm.

Table S2. Anion-cation distance and Coulombic attraction energy (V) between the four cation charges in a molecule (n = 1 to 4) and the nearest anion charge in the clay mineral nanosheet at the maximum and minimum total energy.

n	Maximum		Minimum	
	r (nm)	V (kcal mol^{-1})	r (nm)	V (kcal mol^{-1})
1	0.771	43.1	0.785	42.4
2	0.764	43.5	0.957	34.7
3	0.771	43.1	0.958	34.7
4	0.764	43.5	0.787	42.2
Total	-	173.2	-	153.0

5.6 References

(1) Tan, C.; Cao, X.; Wu, X. J.; He, Q.; Yang, J.; Zhang, X.; Chen, J.; Zhao, W.; Han, S.; Nam, G. H.; et al. Recent Advances in Ultrathin Two-Dimensional Nanomaterials. *Chem. Rev.* **2017**, *117*, 6225–6331.

(2) Büchner, C.; Heyde, M. Two-Dimensional Silica Opens New Perspectives. *Prog. Surf. Sci.* **2017**, *92*, 341–374.

(3) Lin, Y. C.; Susi, T.; Kotakoski, J.; Ramasse, Q. M.; Kepaptsoglou, D.; Meyer, J. C.; Suenaga, K. Towards Atomically Precise Manipulation of 2D Nanostructures in the Electron Microscope. *2D Mater.* **2017**, *4*, 042004.

(4) Sohlberg, K.; Pennycook, T. J.; Zhou, W.; Pennycook, S. J. Insights into the Physical Chemistry of Materials from Advances in HAADF-STEM. *Phys. Chem. Chem. Phys.* **2015**, *17*, 3982–4006.

(5) Nakamura, E. Atomic-Resolution Transmission Electron Microscopic Movies for Study of Organic Molecules, Assemblies, and Reactions: The First 10 Years of Development. *Acc. Chem. Res.* **2017**, *50*, 1281–1292.

(6) Skowron, S. T.; Chamberlain, T. W.; Biskupek, J.; Kaiser, U.; Besley, E.; Khlobystov, A. N. Chemical Reactions of Molecules Promoted and Simultaneously Imaged by the Electron Beam in Transmission Electron Microscopy. *Acc. Chem. Res.* **2017**, *50*, 1797–1807.

(7) Koshino, M.; Tanaka, T.; Solin, N.; Suenaga, K.; Isobe, H.; Nakamura, E. Imaging of Single Organic Molecules in Motion. *Science* **2007**, *316*, 853–853.

(8) Chen, Q.; Dwyer, C.; Sheng, G.; Zhu, C.; Li, X.; Zheng, C.; Zhu, Y. Imaging Beam-Sensitive Materials by Electron Microscopy. *Adv. Mater.* **2020**, *32*, 1–42.

(9) Krivanek, O. L.; Dellby, N.; Murfitt, M. F.; Chisholm, M. F.; Pennycook, T. J.; Suenaga, K.; Nicolosi, V. Gentle STEM: ADF Imaging and EELS at Low Primary Energies. *Ultramicroscopy* **2010**, *110*, 935–945.

(10) Sasaki, T.; Sawada, H.; Hosokawa, F.; Sato, Y.; Suenaga, K. Aberration-Corrected STEM/TEM Imaging at 15kV. *Ultramicroscopy* **2014**, *145*, 50–55.

(11) Susi, T.; Meyer, J. C.; Kotakoski, J. Quantifying Transmission Electron Microscopy Irradiation Effects Using Two-Dimensional Materials. *Nat. Rev. Phys.* **2019**, *1*, 397–405.

(12) Skowron, S. T.; Roberts, S. L.; Khlobystov, A. N.; Besley, E. The Effects of Encapsulation on Damage to Molecules by Electron Radiation. *Micron* **2019**, *120*, 96–103.

(13) Gerkman, M. A.; Sinha, S.; Warner, J. H.; Han, G. G. D. Direct Imaging of Photoswitching Molecular Conformations Using Individual Metal Atom Markers. *ACS Nano* **2019**, *13*, 87–96.

(14) Mittelberger, A.; Kramberger, C.; Meyer, J. C. Insights into Radiation Damage from Atomic Resolution Scanning Transmission Electron Microscopy Imaging of Mono-Layer $CuPcCl_{16}$ Films on Graphene. *Sci. Rep.* **2018**, *8*, 4813.

(15) Koshiya, S.; Yamashita, S.; Kimoto, K. Microscopic Observation of Dye Molecules for Solar Cells on a Titania Surface. *Sci. Rep.* **2016**, *6*, 2–7.

(16) Kengmana, E. S.; Lee, J. K.; Li, X.; Warner, J. H.; Han, G. G. D. Self-Assembly of Bowlic Supramolecules on Graphene Imaged at the Individual Molecular Level Using Heavy Atom Tagging. *Small* **2020**, 2002860.

(17) Ishida, Y. Manipulation of Supramolecular 2D Assembly of Functional Dyes toward Artificial Light-Harvesting Systems. *Pure Appl. Chem.* **2015**, *87*, 3–14.
(18) Takagi, S.; Eguchi, M.; Tryk, D. A.; Inoue, H. Porphyrin Photochemistry in Inorganic/Organic Hybrid Materials: Clays, Layered Semiconductors, Nanotubes, and Mesoporous Materials. *J. Photochem. Photobiol. C Photochem. Rev.* **2006**, *7*, 104–126.
(19) Okada, T.; Ide, Y.; Ogawa, M. Organic-Inorganic Hybrids Based on Ultrathin Oxide Layers: Designed Nanostructures for Molecular Recognition. *Chem. Asian J.* **2012**, *7*, 1980–1992.
(20) Bujdák, J. Effect of the Layer Charge of Clay Minerals on Optical Properties of Organic Dyes. A Review. *Appl. Clay Sci.* **2006**, *34*, 58–73.
(21) Akita, I.; Ishida, Y.; Yonezawa, T. Atomic-Scale Imaging of a Free-Standing Monolayer Clay Mineral Nanosheet Using Scanning Transmission Electron Microscopy. *J. Phys. Chem. Lett.* **2020**, *11*, 3357–3361.
(22) Akita, I.; Ishida, Y.; Yonezawa, T. Distinctive Stability of Free-Standing Monolayer Clay Mineral Nanosheet under Transmission Electron Microscopy. *Phys. Chem. Chem. Phys.* **2020**, *22*, 25095–25102.
(23) Ishida, Y.; Masui, D.; Shimada, T.; Tachibana, H.; Inoue, H.; Takagi, S. The Mechanism of the Porphyrin Spectral Shift on Inorganic Nanosheets: The Molecular Flattening Induced by the Strong Host-Guest Interaction Due to the "Size-Matching Rule." *J. Phys. Chem. C* **2012**, *116*, 7879–7885.
(24) Akita, I.; Ishida, Y.; Yonezawa, T. Counting the Layer Number of Free-Standing Montmorillonite Nanosheets Using Annular Dark Field Scanning Transmission Electron Microscopy. *Clay Sci.* **2019**, *23*, 41–45.
(25) *The X-Ray Identification and Crystal Structures of Clay Minerals*; Brown, G., Ed.; Mineralogical Society, Clay Minerals Group: London, 1961.
(26) Stewart, J. J. P. Comparison of the Accuracy of Semiempirical and Some DFT Methods for Predicting Heats of Formation. *J. Mol. Model.* **2004**, *10*, 6–12.
(27) Colliex, C.; Gloter, A.; March, K.; Mory, C.; Stéphan, O.; Suenaga, K.; Tencé, M. Capturing the Signature of Single Atoms with the Tiny Probe of a STEM. *Ultramicroscopy* **2012**, *123*, 80–89.
(28) Georgakilas, V.; Tiwari, J. N.; Kemp, K. C.; Perman, J. A.; Bourlinos, A. B.; Kim, K. S.; Zboril, R. Noncovalent Functionalization of Graphene and Graphene Oxide for Energy Materials, Biosensing, Catalytic, and Biomedical Applications. *Chem. Rev.* **2016**, *116*, 5464–5519.
(29) Daukiya, L.; Seibel, J.; De Feyter, S. Chemical Modification of 2D Materials Using Molecules and Assemblies of Molecules. *Adv. Phys. X* **2019**, *4*, 1625723.
(30) Hüser, F.; Olsen, T.; Thygesen, K. S. How Dielectric Screening in Two-Dimensional Crystals Affects the Convergence of Excited-State Calculations: Monolayer MoS_2. *Phys. Rev. B* **2013**, *88*, 245309.
(31) Laturia, A.; Van de Put, M. L.; Vandenberghe, W. G. Dielectric Properties of Hexagonal Boron Nitride and Transition Metal Dichalcogenides: From Monolayer to Bulk. *npj 2D Mater. Appl.* **2018**, *2*, 6.
(32) Mathew, K.; Sundararaman, R.; Letchworth-Weaver, K.; Arias, T. A.; Hennig, R. G. Implicit Solvation Model for Densityfunctional Study of Nanocrystal Surfaces and Reaction Pathways. *J. Chem. Phys.* **2014**, *140*, 084106.

(33) Ishida, Y.; Shimada, T.; Tachibana, H.; Inoue, H.; Takagi, S. Regulation of the Collisional Self-Quenching of Fluorescence in Clay/Porphyrin Complex by Strong Host-Guest Interaction. *J. Phys. Chem. A* **2012**, *116*, 12065–12072.
(34) Hasegawa, S.; Kunisada, Y.; Sakaguchi, N. Diffusion of a Single Platinum Atom on Light-Element-Doped Graphene. *J. Phys. Chem. C* **2017**, *121*, 17787–17795.
(35) Ishida, Y.; Masui, D.; Tachibana, H.; Inoue, H.; Shimada, T.; Takagi, S. Controlling the Microadsorption Structure of Porphyrin Dye Assembly on Clay Surfaces Using the "Size-Matching Rule" for Constructing an Efficient Energy Transfer System. *ACS Appl. Mater. Interfaces* **2012**, *4*, 811–816.

Chapter 6

Simultaneous Visualization of Different Types of Molecules Using Metal Markers

6.1 Introduction

In previous section the direct imaging of individual molecules on clay mineral nanosheet was achieved by ADF−STEM using Pt (Z = 78) atom marker coordinated to the center of the molecule. The advantages of this method can be further emphasized by exploring other types of heavy metal markers that can be used in addition to Pt. As the ease of coordination depends on the type of marker element and the structure of the target molecule, the search for selectable marker candidates is also essential for the future synthesis of new visualizable molecules. Considering the contrast of ADF-STEM, which is proportional to the 1.4-1.7 power of the atomic number, and the thickness of clay mineral nanosheets consisted of a few atoms, there should be a threshold for the atomic number to be effective as a marker in ADF−STEM imaging. Various types of elements have been reported to be used as markers in ADF observations for nanocarbon-based systems (e.g., Pt,[1,2] Cu,[3] Ru,[4] and W[5]). Mittelberger et al. reported visualization of Cu phthalocyanine by ADF−STEM, where relatively lighter element Cu (Z = 29) worked as marker owing to one-atom-thick structure of graphene.[3] The elements with such smaller atomic number, however, will not work as markers on relatively thick (~ 1 nm) clay mineral nanosheets.

In this section I demonstrated the ability to visualize the marker atoms in ADF-STEM using the organic molecules containing three different atom markers (Figure 1) to determine the threshold of the atomic number. The molecules differed only in the elements of the marker coordinated to the center were used to exclude any influence from other than the atomic number of the marker. Additionally, two types of molecules with different atom markers adsorbed on clay minerals were distinguished by differences in ADF−STEM contrast.

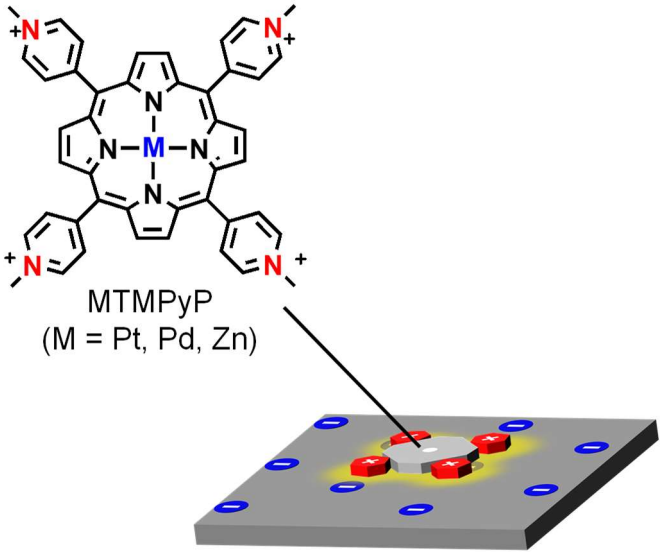

Figure 1. Schematic illustrations of a supramolecular assembly based on multivalent electrostatic interactions between the anionic clay mineral nanosheet and cationic organic molecule. MTMPyP. M indicates a marker atom coordinated to the center (M = Pt, Pd, Zn).

6.2 Experimental section

Specimen preparation.

Montmorillonite is a typical anionic clay mineral and was acquired from Kunimine Industries (Kunipia F). The chemical structure of montmorillonite corresponded to the formula $Na_{0.66}(Al_{3.34}Mg_{0.66})Si_8O_{20}(OH)_4$ with a cation exchange capacity (CEC) of 1.19 meq g^{-1}. The montmorillonite was purified by preparing a raw clay dispersion (300 mL, 10 g L^{-1}) in centrifuge bottles, which was centrifuged at a rotation speed of 7000 rpm for 15 min. The supernatant was collected, poured into a container with 1500 mL ethanol, and mixed for 1 h at 70 °C. The resulting colloidal solution was filtered through a polytetrafluoroethylene (PTFE) membrane with a pore size of 0.1 μm (Millipore). The solids were collected and dried under vacuum in a rotary pump overnight. The dried solids were dispersed in ultrapure water and stored overnight for complete exfoliation into nanosheets. Pt(II) tetrakis(1-methylpyridinium-4-yl) porphyrin chloride (PtTMPyP), Pd(II) tetrakis(1-methylpyridinium-4-yl) porphyrin chloride (PfTMPyP), and Zn(II) tetrakis(1-methylpyridinium-4-yl) porphyrin chloride (ZnTMPyP) were purchased from Frontier Scientific and dissolved in ultrapure water. The water content of the clay and MTMPyP (M = Pt, Pd, Zn) was determined via thermogravimetry and differential thermal analysis (TG-DTA) using a thermogravimetry analyzer (SHIMADZU DTG60H) before preparing the aqueous solutions. The MTMPyP-clay assemblies were prepared by mixing the aqueous solutions of clay and MTMPyP. The saturated concentration for monomer adsorption was determined based on the ultraviolet-visible (UV-vis) adsorption spectra on a series of samples with known loading levels of MTMPyP vs. CEC of clay ranging from 10% to 160 (UV-1800; SHIMADZU).

The saturation adsorption densities of PdTMPyP and ZnTMPyP were similar to the results for PtTMPyP described in chapter 5. The absorption spectra of PdTMPyP-clay at various loading level and the corresponding Lambert-Beer plot are given in Figure S1 in Supporting Information. When the number of charges and the structure of the molecule are the same, the saturation adsorption capacity of single molecule adsorption on clay mineral nanosheet is the same to the case of PtTMPyP regardless of the metal atom coordinated to the center.[6] This was also applicable to ZnTMPyP.

ADF−STEM experiments and simulations.

The STEM/TEM specimens were prepared by drop-casting the water dispersion of MTMPyP-clay on a perforated carbon-coated Cu grid. STEM analysis was conducted using a JEM-ARM200F (JEOL) equipped with spherical aberration correctors at an acceleration voltage of 80 kV and camera length of 100 mm. The convergence semi-angle of the incident probe was 13.8 mrad, and the inner and outer detection semi-angles of the ADF detector were 54 and 220 mrad, respectively. Fourier transform was performed using the DigitalMicrograph (Gatan). The ADF–STEM image simulations were performed using a multislice program Dr. Probe.[7] The unit cell information of montmorillonite for simulation was downloaded from the Crystallography Open Database[8] with CIF number 1100106 followed by modification. The cell dimension is a = 5.411(4), b = 9.0(5), c = 10.25(2) Å, β = 100.3(1)º. The electron optical parameters were set to the experimental conditions. The model used in the multislice calculations was constructed to ensure that the nitrogen atoms of the methylpyridinium group of the molecule and the oxygen atoms on the surface of the clay mineral nanosheets were in closet position. The z height of MTMPyP on the clay mineral nanosheets was based on a dihedral angle between the

porphyrin core and methylpyridinium substituents of 43°, which was chosen based on a previous report on structural minimization of metal-free TMPyP adsorbed on clay mineral nanosheets.[9]

6.3 Results and discussion

ADF-STEM images simulation was conducted for three different porphyrin-clay mineral nanosheet assemblies including Pt (Z = 78), Pd (Z = 46), and Zn (Z = 30) as markers (Figure 2). The simulated ADF−STEM images in Figure 2b-d and the corresponding intensity profiles in Figure 2e indicated that Pt and Pd atom were realized as bright spot although Zn atom were not distinguishable from the contrast in clay minerals. Note that the carbon skeleton could also not be identified, since their contrast was interfered with by the clay minerals nanosheet.

Figure 3 shows the experimental ADF−STEM images of MTMPyP-clay mineral nanosheet and pristine clay mineral nanosheet. The loading level of molecules was 90% vs. CEC of clay. As predicted from the simulation results in Figure 2, the contrast of Pt and Pd atoms were realized as a clear bright spot, confirming the uniform and well-dispersed adsorption of the molecules similar to the results in Chapter 5. For ZnTMPyP-clay assemblies in Figure 3c, however, there were no obvious bright spots corresponding to the molecules, and the images were similar to the result of the pristine clay mineral nanosheet. These results suggest that the threshold of atomic number for ADF−STEM markers on clay mineral nanosheets should be between Zn (Zn = 30) and Pd (Z = 46).

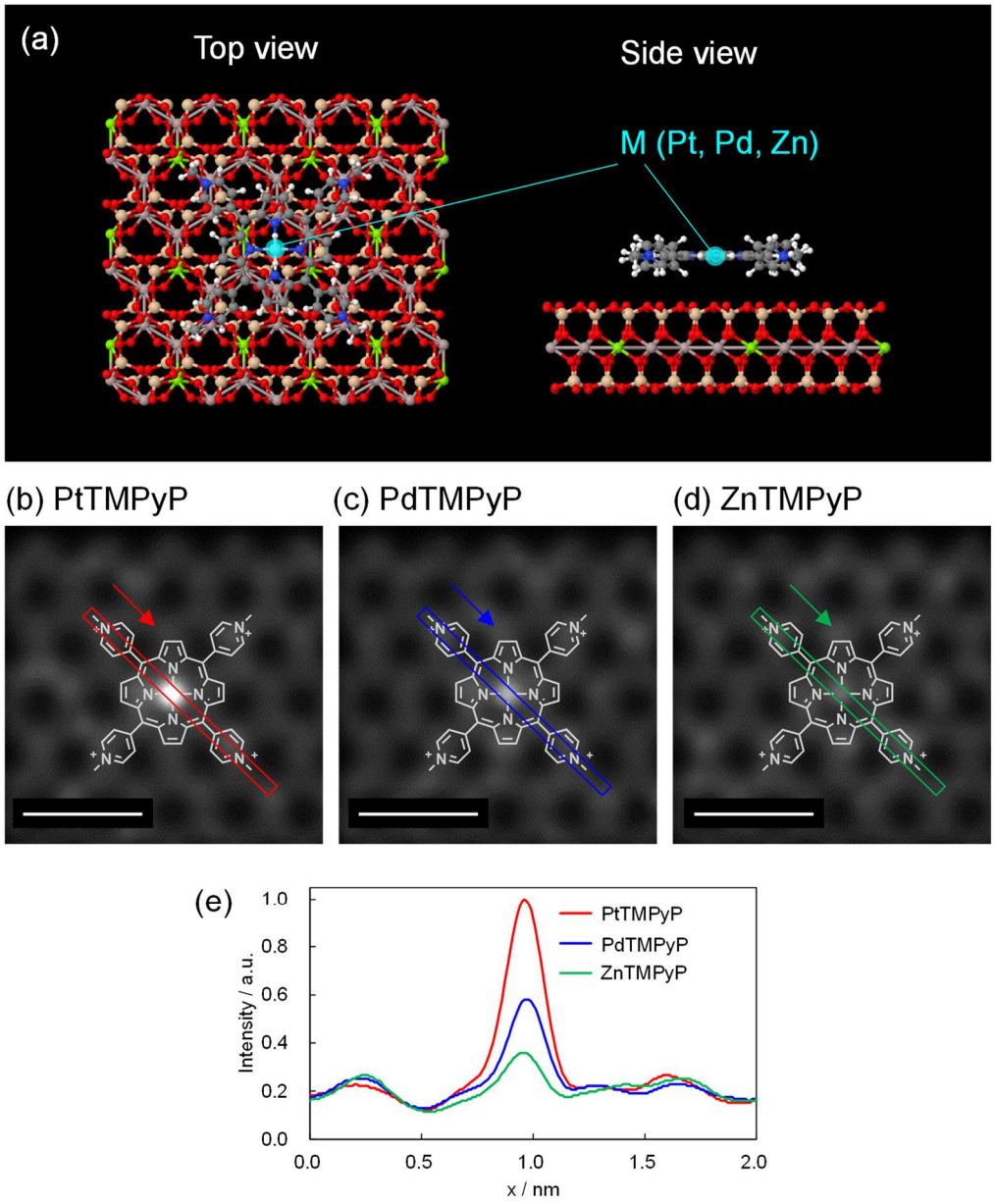

Figure 2. (a) Atomic models of MTMPyP on clay mineral nanosheet and simulated ADF−STEM images of (b) PtTMPyP, (c) PdTMPyP, and (d) ZnTMPyP on clay mineral nanosheet. (e) Intensity profiles of the boxed regions in panel b to c. Scale bars = 1 nm.

Note that the intensity histogram of the bright spots obtained from the ADF-STEM images of PtTMPyP (Figure S3a) and PdTMPyP (Figure S3b) show unimodal distribution. The intensity of each bright spot was determined by extracting the value at the center of signal intensity around the spot. The distribution of intensity is caused by the blurring of bright spots by molecular vibration and drift of the specimen, and the overlap with the contrast of clay mineral nanosheets. The difference in height through the nanosheet may also affect the contrast of the marker, but it is difficult to separate it from the effects from other factors mentioned above, and it was impossible to distinguish which side of the single layer nanosheet the molecule was adsorbed on.

Furthermore, the assemblies of two types of molecules with different markers and clay mineral nanosheets were prepared using a mixture of PtTMPyP and PdTMPyP aqueous solutions. This binary assembly is hereafter denoted as Pt+PdTMPyP-clay mineral nanosheet. ADF-STEM images simulation of Pt+PdTMPyP-clay mineral nanosheet in Figure 4b indicates that Pt and Pd markers was visualized simultaneously on clay mineral nanosheets and there were obvious differences in their contrast. Figure 4c is the intensity profile of the boxed region in Figure 4b and suggests that the ratio of the peak heights of platinum and palladium was approximately 2.

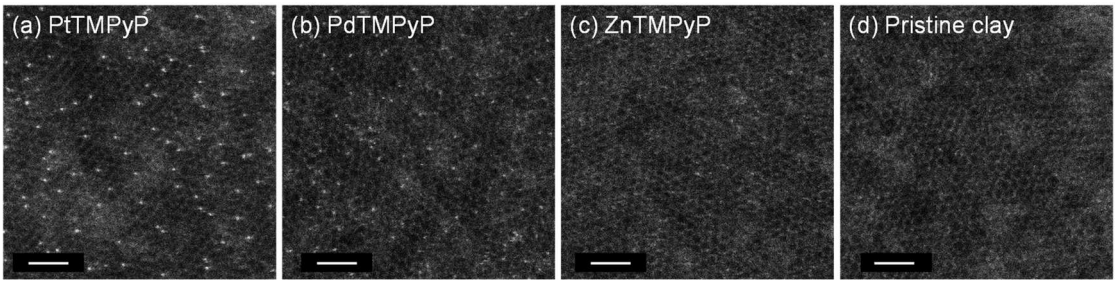

Figure 3. Experimental ADF−STEM images of (a) PtTMPyP, (b) PdTMPyP (c) ZnTMPyP-clay mineral nanosheet and (d) pristine clay mineral nanosheet. The loading level of molecules was 90% vs. CEC of clay. The image size and pixel size were 1024×1024 pixels and 0.013×0.013 nm^2/pixel, respectively. The pixel time was set to 20 μs. Scale bars = 2 nm.

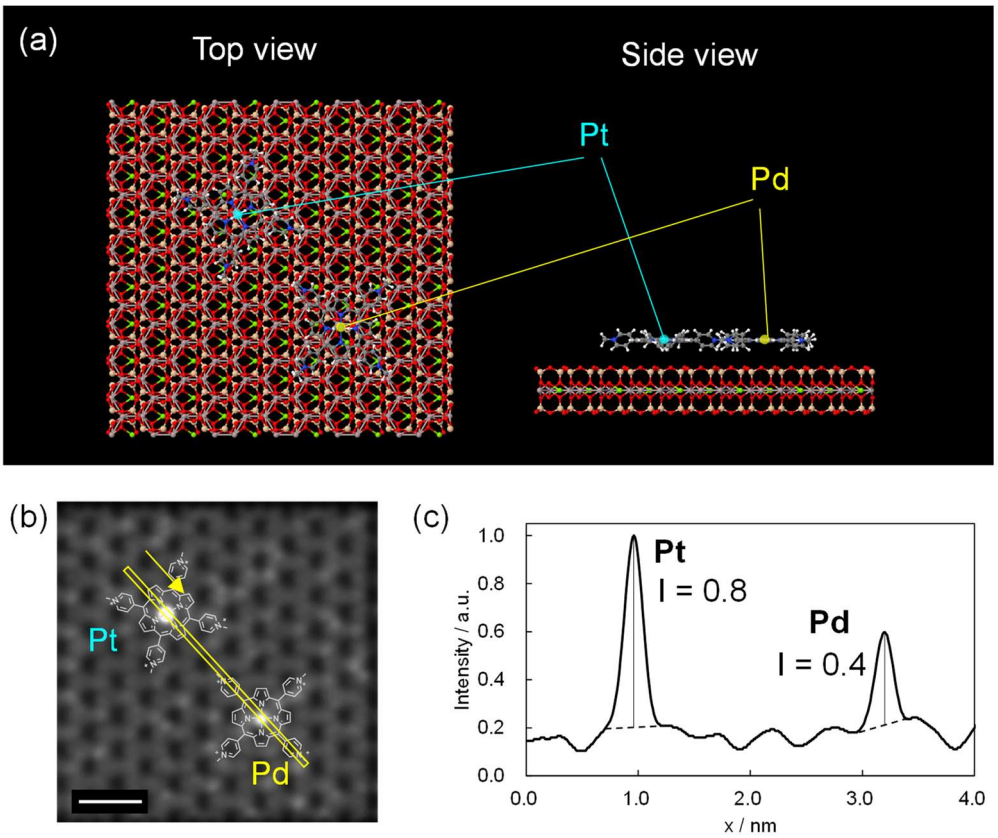

Figure 4. (a) Atomic models of PtTMPyP and Pd TMPyP on clay mineral nanosheet, (b) the corresponding simulated ADF−STEM images, and (c) the intensity profile of the blue boxed region in panel b.

Pt+PdTMPyP-clay mineral nanosheet assemblies were prepared using a aqueous solution of PtTMPyP and PdTMPyP in 1:1 (mol/mol). Figure 5a and b show the absorption spectra of Pt+PdTMPyP (black), PtTMPyP (red), and PdTMPyP (blue) molecules free in water and assembled with clay mineral nanosheet at 45 % vs. CEC of clay, respectively. The maximum absorption wavelengths of the Soret band for Pt+PdTMPyP were 410 nm for the free molecules and 434 nm for the molecules adsorbed on the sheet. This shift to the longer wavelengths upon adsorption on the sheet was attributed to planarization of the methylpyridinium substituents with respect to the porphyrin core.[6] As shown in the spectrum of the sum shown in green line, the spectra of Pt+PdTMPyP can be expressed based spectral fitting of two components for PtTMPyP (red) and PdTMPyP (blue). Therefore, the single molecular adsorption of each type proceeded independently, even when these two molecules were mixed. ADF-STEM samples were prepared at a saturated adsorption concentration of 90% vs CEC of clay. The normalized absorption spectra of Pt+PdTMPyP45% and 90%-clay were in agreement with each other, conforming that there was no aggregate formation even at 90% (Figure S2).

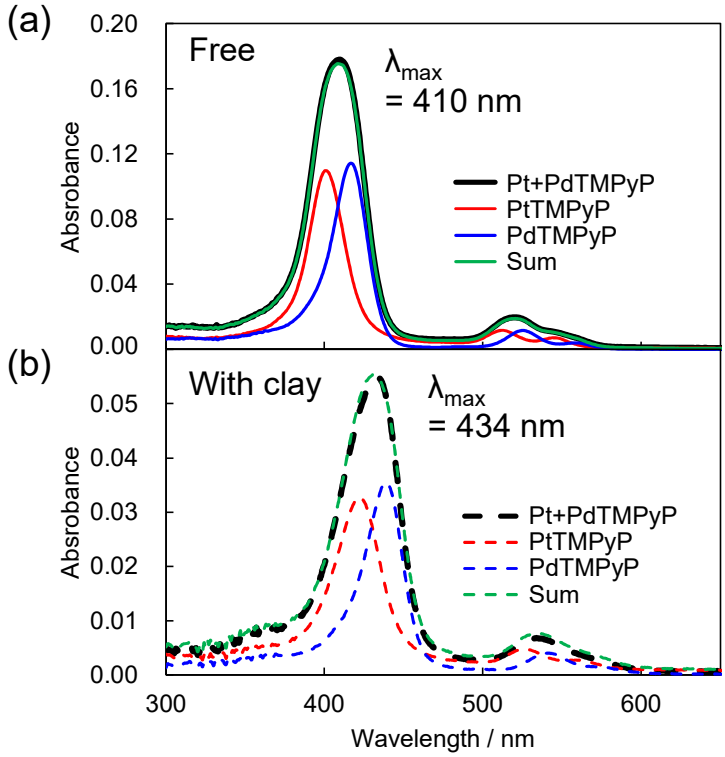

Figure 5. Absorption spectra of Pt+PdTMPyP (black), PtTMPyP (red), and Pd TMPyP (blue) molecules (a) free in water and (b) assembled with clay mineral nanosheets. Green line indicates the sum of the spectra for PtTMPyP and PdTMPyP. MTMPyP-clay assemblies were prepared at 45% vs. CEC of clay in aqueous solution.

Figure 6a is an experimental ADF−STEM image of Pt+PdTMPyP90%-clay assemblies. Figure 6b emphasizes the bright spots by different color tones and Figure 6d is a magnified image of the boxed area in Figure 6b. The highly bright and slightly darker spots were observed on the clay mineral nanosheets, which were considered to be Pt and Pd markers, respectively. The bright and slightly dark bright spots were randomly arranged without segregation,[10] and their ratio was around 1 to 1. Furthermore, the sequential ADF−STEM images in Figure 6c-e and the corresponding intensity profiles in Figure 6f-h indicated that the combination of brightness and darkness of the bright spots did not change even after repeated scans. Similar to the intensity profile of the simulation, the contrast ratio between Pt (brighter spots) and Pd (slightly darker spots) was approximately 2. Therefore, when the atomic numbers are as far apart as Pt (Z = 78) and Pd (Z = 46), it is possible to detect simultaneously and distinguish them on clay mineral nanosheet in ADF−STEM imaging. Additionally, the full width half maxima and relative configuration of the marker atoms are similar during several scanning, suggesting that the molecules are strongly fixed via multivalent electrostatic interactions and the motion of molecules were suppressed as described in chapter 5. Note that the intensity histogram of Pt+PdTMPyP-clay without considering the effect of contrast for clay mineral nanosheet in Figure S3c exhibits the bimodal distribution, where the two peaks were considered to be Pt and Pd atoms. Although the two peaks in the histogram partly overlap, the atomic species can be assigned more accurately by separating the contrast of the clay mineral nanosheets by local line analysis as shown in Figure 6f-h.

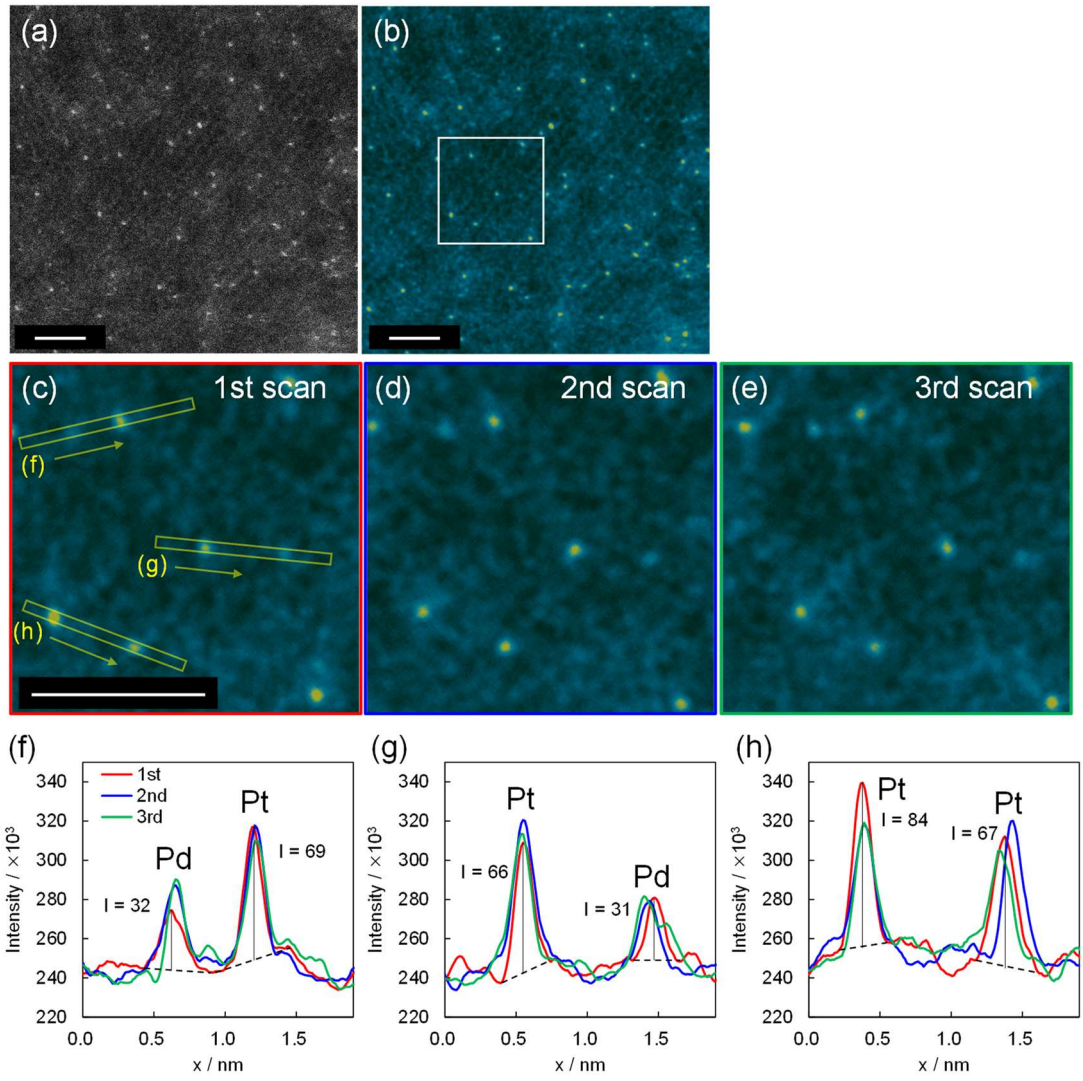

Figure 6. (a) Experimental ADF−STEM image of Pt+PdTMPyP-clay mineral nanosheet and (b) the corresponding image displayed with different color tone to emphasize the contrast of the markers. (c-e) an enlarged image of the white boxed region in panel b from 1st to 3rd scans, and (f-h) the corresponding intensity profiles of the yellow boxed regions in panel d of 1st (red), 2nd (blue), and 3rd (green) scans. The loading level of molecules was 90% vs. CEC of clay. The image size and pixel size were 1024×1024 pixels and 0.013×0.013 nm^2/pixel, respectively. The pixel time was set to 20 μs. Scale bars = 2 nm.

6.4 Conclusion

In conclusion, I here demonstrated the ability to visualize the marker atoms in ADF-STEM for the direct imaging of individual molecules in the clay nanosheet based assemblies using the molecules containing three different atom markers. The results suggest that the threshold of atomic number for ADF−STEM markers on clay mineral nanosheets should be between Zn (Z = 30) and Pd (Z = 46) since the contrast of ADF-STEM imaging is generally proportional to the 1.4-1.7 power of the atomic number. Also, using the molecules coordinated with Pt and Pd atoms, identification of molecule types by differences in ADF contrast of marker atoms was also demonstrated. The knowledge of the atomic number of the markers obtained from this experiment will be a guideline for future visualization of more detailed molecular structures and more complex assembly structures. In this experiment, only markers for the molecular center were used, but in the future, it is expected that markers will be introduced at the substituents and edges of the molecule to obtain further information such as intermolecular orientations. For example, substitution of terminal hydrogen by iodine may be effective for such observation as well as suppression of electron damage in the guest molecule.[11–13] Although there are limitations in the identification of markers only by ADF contrast, more precise identification will be possible when combined with analytical electron microscopy such as EELS, which allows elemental analysis at the atomic level.

6.5 Supporting information

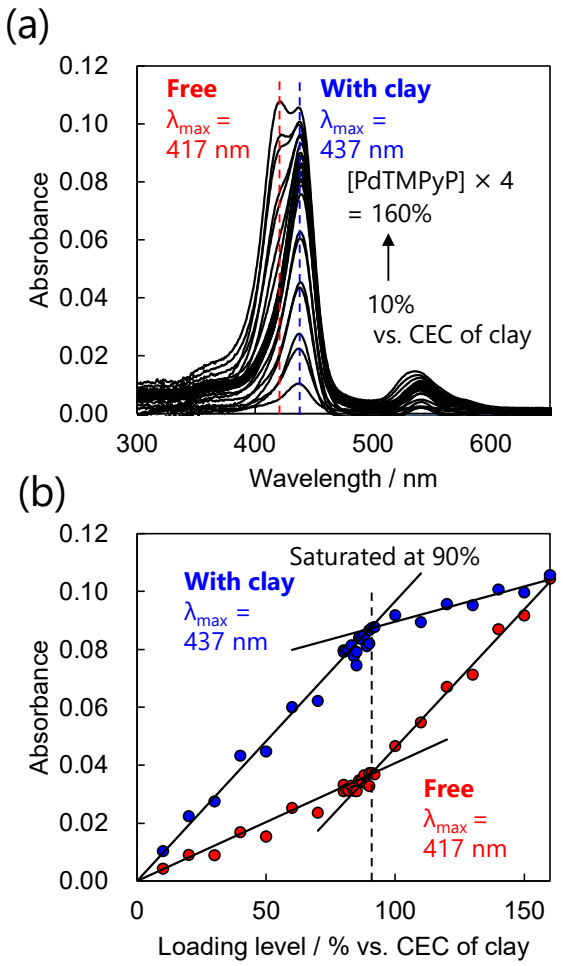

Figure S1. Spectral characterization of PdTMPyP-clay dispersion in water. (a) Absorption spectra of PtTMPyP-clay assemblies at various molecule loading levels up to 160% vs. CEC of clay in aqueous solution and (b) Lambert-Beer plots obtained from the absorption spectra at 417 (red) and 437 nm (blue).

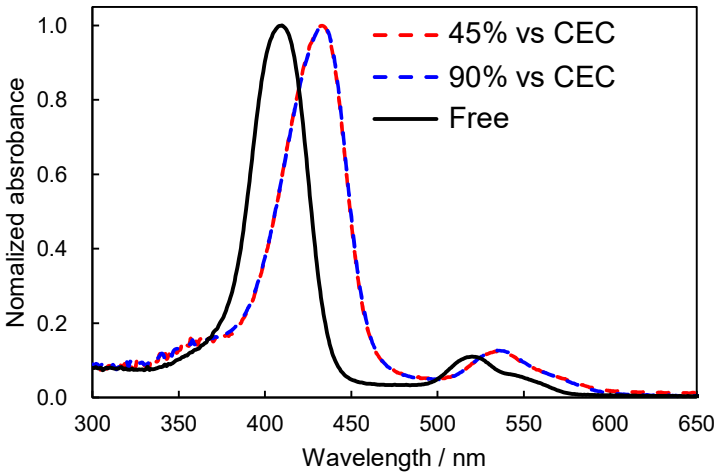

Figure S2. Normalized absorption spectra of Pt+PdTMPyP free in water, Pt+PdTMPyP45%, and 90%-clay assemblies.

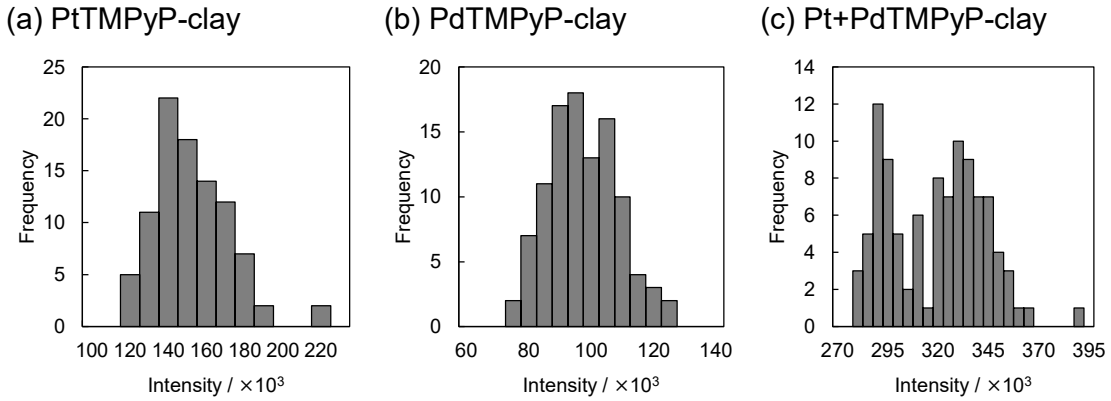

Figure S3. The histograms of intensity distribution for bright spots in ADF−STEM images of (a) PtTMPyP-clay, (b) PdTMPyP-clay, and (c) Pt+PdTMPyP-clay in Figure 3a, b, and Figure 6a, respectively. The intensity of each bright spot was determined by extracting the value at the center of signal intensity around the spot.

6.6 References

(1) Gerkman, M. A.; Sinha, S.; Warner, J. H.; Han, G. G. D. Direct Imaging of Photoswitching Molecular Conformations Using Individual Metal Atom Markers. *ACS Nano* **2019**, *13*, 87–96.

(2) Gerkman, M. A.; Lee, J. K.; Li, X.; Zhang, Q.; Windley, M.; Fonseca, M. V; Lu, Y.; Warner, J. H.; Han, G. G. D. Direct Imaging of Individual Molecular Binding to Clean Nanopore Edges in 2D Monolayer MoS_2. *ACS Nano* **2020**, *14*, 153–165.

(3) Mittelberger, A.; Kramberger, C.; Meyer, J. C. Insights into Radiation Damage from Atomic Resolution Scanning Transmission Electron Microscopy Imaging of Mono-Layer $CuPcCl_{16}$ Films on Graphene. *Sci. Rep.* **2018**, *8*, 4813.

(4) Koshiya, S.; Yamashita, S.; Kimoto, K. Microscopic Observation of Dye Molecules for Solar Cells on a Titania Surface. *Sci. Rep.* **2016**, *6*, 2–7.

(5) Kengmana, E. S.; Lee, J. K.; Li, X.; Warner, J. H.; Han, G. G. D. Self-Assembly of Bowlic Supramolecules on Graphene Imaged at the Individual Molecular Level Using Heavy Atom Tagging. *Small* **2020**, 2002860.

(6) Ishida, Y.; Masui, D.; Shimada, T.; Tachibana, H.; Inoue, H.; Takagi, S. The Mechanism of the Porphyrin Spectral Shift on Inorganic Nanosheets: The Molecular Flattening Induced by the Strong Host-Guest Interaction Due to the "Size-Matching Rule." *J. Phys. Chem. C* **2012**, *116*, 7879–7885.

(7) Barthel, J. Dr. Probe: A Software for High-Resolution STEM Image Simulation. *Ultramicroscopy* **2018**, *193* (April), 1–11.

(8) Gražulis, S.; Chateigner, D.; Downs, R. T.; Yokochi, A. F. T.; Quiró, M.; Lutterotti, L.; Manakova, E.; Butkus, J.; Moeck, P.; Le Bail, A. Crystallography Open Database-an Open-Access Collection of Crystal Structures. *J. Appl. Cryst.* **2009**, *42*, 726–729.

(9) Ishida, Y.; Shimada, T.; Tachibana, H.; Inoue, H.; Takagi, S. Regulation of the Collisional Self-Quenching of Fluorescence in Clay/Porphyrin Complex by Strong Host-Guest Interaction. *J. Phys. Chem. A* **2012**, *116*, 12065–12072.

(10) Ishida, Y.; Masui, D.; Tachibana, H.; Inoue, H.; Shimada, T.; Takagi, S. Controlling the Microadsorption Structure of Porphyrin Dye Assembly on Clay Surfaces Using the "Size-Matching Rule" for Constructing an Efficient Energy Transfer System. *ACS Appl. Mater. Interfaces* **2012**, *4*, 811–816.

(11) Egerton, R. F. Mechanisms of Radiation Damage in Beam-Sensitive Specimens, for TEM Accelerating Voltages between 10 and 300 kV. *Microsc. Res. Tech.* **2012**, *75*, 1550–1556.

(12) Koshino, M.; Kurata, H.; Isoda, S. Stability Due to Peripheral Halogenation in Phthalocyanine Complexes. *Microsc. Microanal.* **2007**, *13*, 96–107.

(13) Skowron, S. T.; Chamberlain, T. W.; Biskupek, J.; Kaiser, U.; Besley, E.; Khlobystov, A. N. Chemical Reactions of Molecules Promoted and Simultaneously Imaged by the Electron Beam in Transmission Electron Microscopy. *Acc. Chem. Res.* **2017**, *50*, 1797–1807.

Chapter 7

Summary and perspectives

Summary

Chapter 1: General introduction summarized supramolecular assemblies via non-covalent interactions, self-assemblies via electrostatic interactions using clay mineral nanosheets, and direct imaging of individual molecules by aberration-corrected electron microscopy. The purpose and objectives of this study were provided.

	Prior researches in S/TEM observation of individual molecules	Organic molecules-clay mineral nanosheet assemblies
(i) Suppression of electron beam damage	• Low acceleration voltage • Low electron dose • **Low dimensional specimen** • **Isolated molecules**	• Thinness of clay nanosheet (ca. 1nm) • Isolation and fixation via multivalent electrostatic interaction
(ii) Effective fixation of molecules	• Encapsulation • Covalent bond • **Non-covalent interaction**	
(iii) Sufficient contrast form light elements	• Nanocarbons imparting easy contrast distinction • Heavy atoms working as marker in ADF–STEM	• Lack of knowledge of atomic resolution observations of clay mineral nanosheets • Extensive variety of metalloporphyrin

Chapter 2: In this section, I demonstrate the direct determination of the layer number of free-standing montmorillonite (Mt) nanosheets using annular dark field (ADF) scanning transmission electron microscopy (STEM). The layer number of the free-standing Mt nanosheets deposited on a holey carbon-coated grid was successfully counted to range from monolayer to four layers by the difference in the ADF contrast. Meanwhile, counting

of the layer numbers was difficult using conventional TEM and bright field STEM due to the low contrast. Therefore, ADF−STEM can potentially be applied to further investigate the clay nanosheets and their molecular complexes by the atomic scale imaging for a deeper understanding of clay-nanosheet-based chemistry.

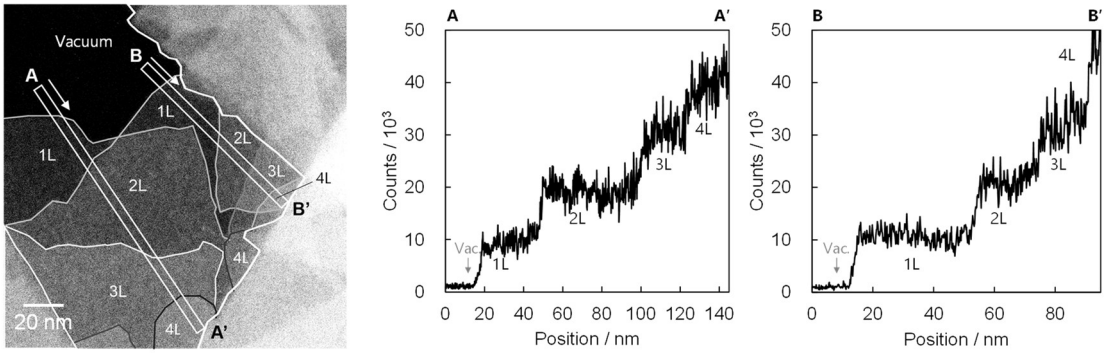

Chapter 3: Among 2D materials, clay mineral nanosheets have been extensively studied owing to their specific features, such as high surface charge and large surface area. Although aberration-corrected scanning transmission electron microscope (STEM) enables the atomic-scale visualization of ultrathin 2D materials such as graphene, imaging of electron-beam sensitive 2D materials with structural complexity is an intricate problem. In this section, I report the first atomic-scale imaging of a free-standing monolayer clay mineral nanosheet using ADF−STEM. The monolayer clay nanosheet was stably observed under optimal conditions, and I confirmed that the hexagonal contrast pattern with a pore of ~4 Å corresponds to the atomic structure of clay mineral consisted of adjacent Si, Al, Mg, and O atoms, by comparing with simulations. The findings offer the usefulness of ADF−STEM techniques for the atomic scale imaging of clay minerals and various 2D materials having electron-beam sensitivity and structural-complexity than few-atom-thick graphene analogs.

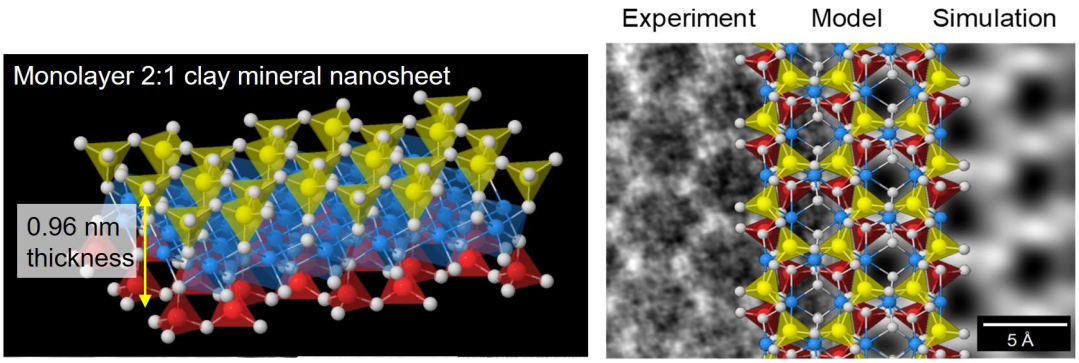

Chapter 4: I reported a stable imaging of free-standing (without any surfactants or matrices) monolayer clay mineral by ADF−STEM at the atomic-scale (Chapter 3), while bulk clay minerals are generally sensitive to the electron beam irradiation. In this section, I demonstrated that the monolayer clay mineral exhibited the outstanding stability under electron beam irradiation compared to two- or three-layered nanosheets via electron diffraction analysis. As the results, monolayer clay mineral nanosheet exhibited the remarkable stability against the beam irradiation using electron diffraction technique, while 2L and 3L Mt showed similar low stabilities. The results suggested that the stability of 1L Mt was owing to the absence of interlayer space, as a site for hydration, as well as its low thickness (~1 nm-thick). The findings here inspire further investigation in free-standing clay mineral using (S)TEM and also for a wide variety of nanomaterials which are strongly hydrated.

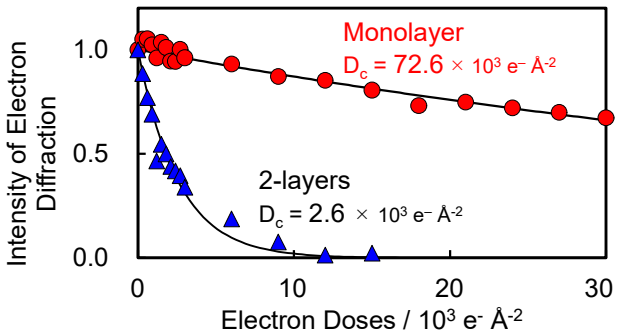

Chapter 5: Recent developments in electron microscopy and novel techniques for the precise control of low-dimensional substrate materials have led to the emergence of direct imaging of organic molecules. However, supramolecular assemblies constructed via non-covalent interactions are structurally unstable under electron bean irradiation. In this section, direct imaging of the single organic molecules and supra-molecular assemblies on the monolayer clay mineral nanosheets was demonstrated via ADF−STEM using heavy metal atom markers. The versatility of multivalent electrostatic interactions for the stable fixation of organic molecules during electron microscopic imaging was demonstrated. To the best of our knowledge, this is the first successful atomic-scale observation of a molecular assembly constructed via weak non-covalent interactions, where the observations corresponded well with the averaged spectroscopic data. Fixation and isolation effect via multivalent electrostatic interaction can be applied to a wide range of supramolecular systems comprising various guest molecules and host materials, thereby broadening the scope of atomic-scale imaging. The local information obtained via electron microscopy using the proposed approach was complemented with averaged information from spectroscopic analysis to correlate the structural characteristics and properties or functionalities of individual molecular species during characterization.

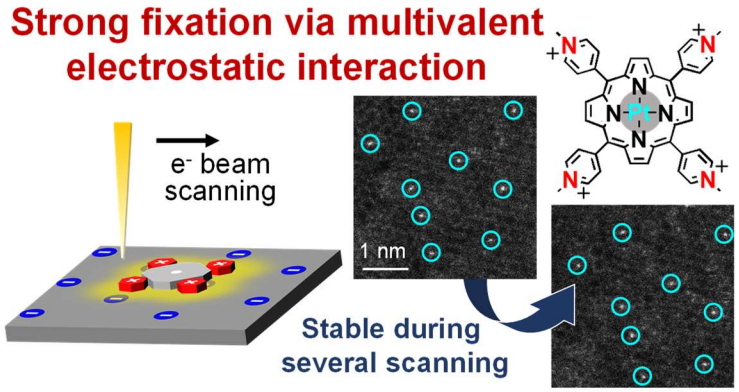

Chapter 6: According to the results in Chapter 5, the ability to visualize the marker atoms in ADF-STEM for the direct imaging of individual molecules in the clay nanosheet based assemblies was demonstrated using the molecules containing three different atom markers. The results suggest that the threshold of atomic number for ADF−STEM markers on clay mineral nanosheets should be between Zn (Z = 30) and Pd (Z = 46) since the contrast of ADF-STEM imaging is generally proportional to the 1.4-1.7 power of the atomic number. Also, using the molecules coordinated with Pt and Pd atoms, identification of molecule types by differences in ADF contrast of marker atoms was also demonstrated. The knowledge of the atomic number of the markers obtained from this experiment will be a guideline for future visualization of more detailed molecular structures and more complex assembly structures.

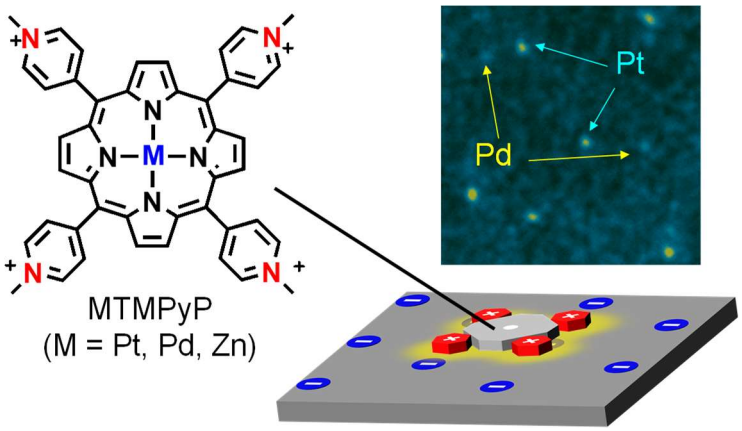

Perspectives

In this thesis I demonstrate the fixation and isolation effect of multivalent electrostatic interactions for direct imaging of individual molecules in supramolecular assemblies. Individual molecules were successfully visualized by ADF−STEM using heavy metal atom markers (Figure 1a). This is the first successful atomic-scale observation of a molecular assembly constructed via weak non-covalent interactions, where the individual intermolecular distances and relative conformations were determined (Figure 1b).

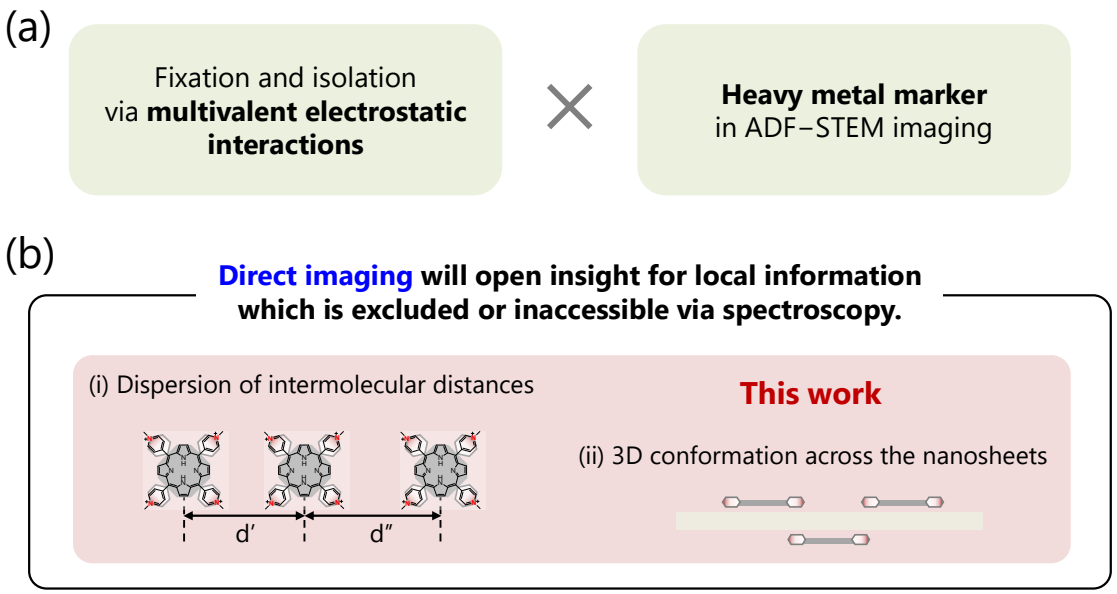

Figure 1. Summary of the findings in this thesis.

Based on this approach, further local information, which is not possible in conventional spectroscopic analyses, would be revealed. Newly designed and synthesized porphyrin derivatives, which have heavy metal marker in the functional group will widen the spectrum of investigation for observing the structural changes of the molecules, their collective structure and spatial arrangement in complexes. The molecular design

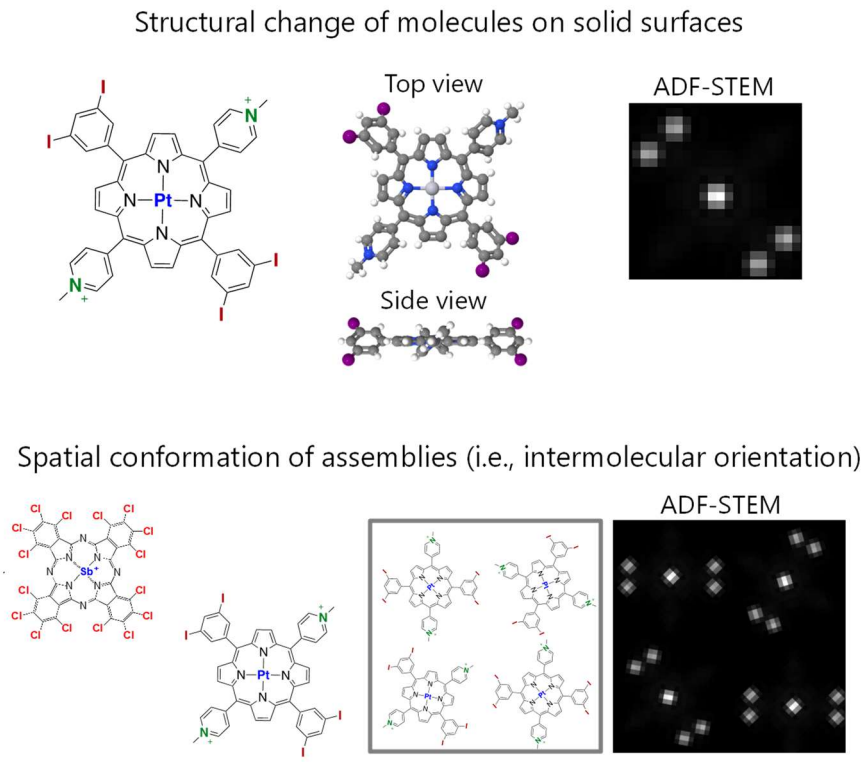

Figure 2. The local information revealed by electron microscopy combined with newly synthesized molecules.

introduces a cationic charge for electrostatic interaction, a heavy metal marker atom in the center, and halogen marker atoms to determine the structural change or spatial conformations (Figure 2). Halogen substitution of terminal hydrogen may also be effective in suppressing electron damage in the guest molecule. The use of halogenated molecules would enable us to observe the samples for longer periods of time and at higher magnifications. Additionally, through systematic observations of variations in the type and number of cationic charge sources, the effects of fixation by electrostatic interactions can be quantitatively evaluated. Although the ability to simultaneously observe both sides of a nanosheet is one of the strengths of the transmission electron microscope, some effort is required to obtain accurate information in the z-direction. A through-focus method and

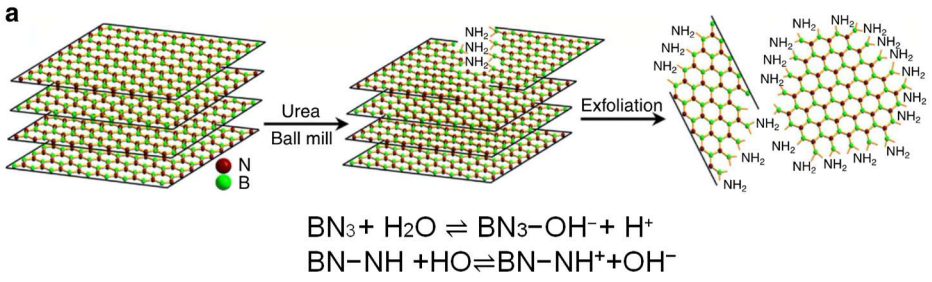

Figure 3. Schematic image of synthesis for charged h-BN nanosheets (W. Lei, et al, *Nat. Commun.* **2015**, *6,* 1–8.)

a three-dimensional tomography have limitations in terms of flexibility and stability of the sample, and z-direction resolution when applied to two-dimensional nanomaterials. These methods will be applied to obtain the information on z-direction in near future by using bulky molecules that increase the distance between molecules and nanosheet and ease the observation of height information.

The fixation and isolation effect by multivalent electrostatic interactions presented in this thesis, therefore, has the potential to be developed for the observation of assemblies using other 2D nanosheet, or for observation by analytical electron microscopy. Although clay minerals are great in terms of abundance, synthesized hexagonal boron nitride nanosheets with controlled anion charge density could be considered as a future host materials, which consist of light element with one-atom-thick structure (Figure 3). The positional stability for relatively long periods of time is an advantage in analytical electron microscopy such as electron energy loss spectroscopy (EELS)−STEM. Senga and Suenega have demonstrated single-atom EELS−STEM analysis for light elements which were not detectable in ADF−STEM imaging, although the spatial resolution is limited by the incident probe size, signal delocalization and atomic movement in nanospace. (Figure 4).

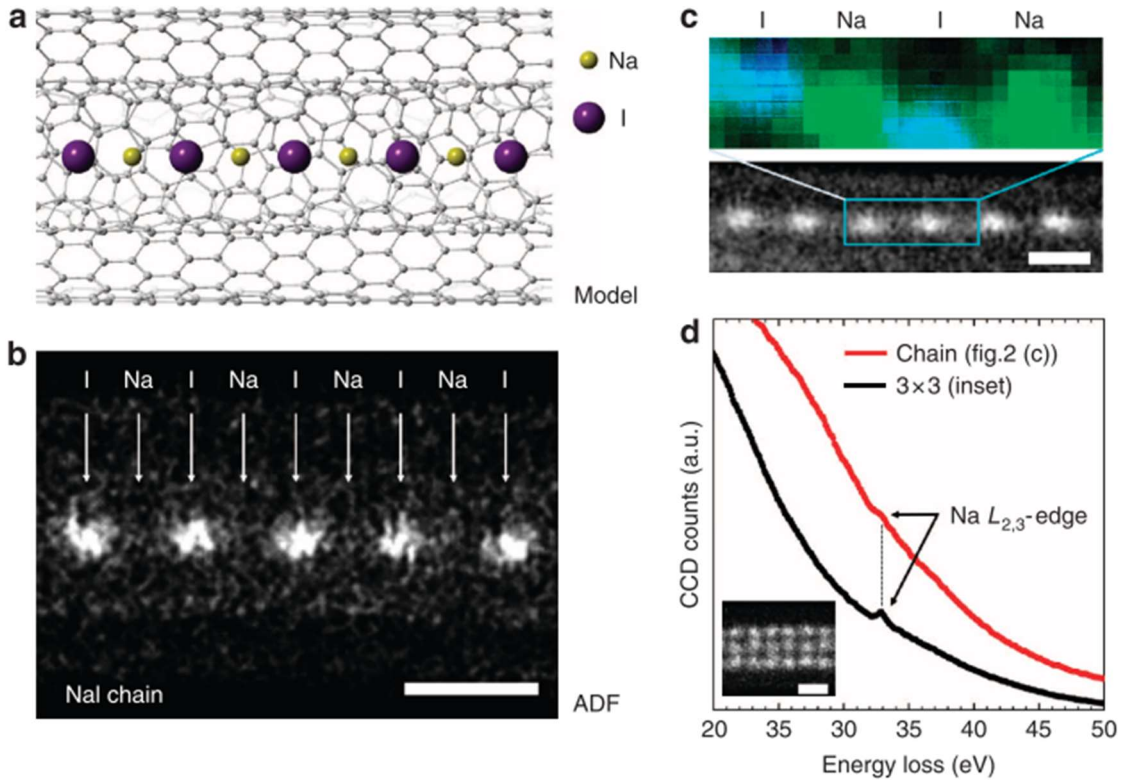

Figure 4. Na atom detection in a 1D NaI crystal. (a,b) A schematic model and an ADF image of a NaI atomic chain in a double walled carbon nanotube, respectively. In the ADF image, Na atoms are invisible while I atoms present as bright spots. (c) An elemental map (upper panel) of a NaI atomic chain shown in a ADF image (bottom panel). (d) The EELS spectrum (red line in d) taken from the NaI atomic chain shown in c. A reference spectrum taken from the 3×3 NaI nanowire is also shown (black line in d). Scale bars, 0.5 nm. (R. Senga et al., *Nat. Commun.* **2015***, 6,* 1–6.)

EELS studies on pyridinic-N defect in graphene realized the identification of graphemic- and pyridinic- nitrogen atoms at the atomic scale. EELS−STEM, therefore, provides an identification of nitrogen atoms of porphyrin rings and methylpyridinium groups, as well as the location of light elements, which are not available in ADF−STEM. Another attractive method is difference phase contrast (DPC)−STEM imaging using a segmented detector, which allows direct visualization of the electromagnetic field in the sample. As shown in the example of single atoms of gold, quantitative mapping of the electric field by DPC-STEM has high sensitivities (Figure 5). Furthermore, the electric field distribution obtained from DPC−STEM can be converted to a charge density distribution in real space (Figure 6). Direct imaging of the location of anionic charge in clay mineral nanosheet and cationic charge in guest molecules would be visualized by DPC−STEM, which allows quantitative understanding of electrostatic interaction in the assemblies.

These various observations drive the structural analysis of individual types of assemblies, but are also essential for precise control of the structures and functions of more complex and flexible supramolecular assemblies by the electron microscopic observation.

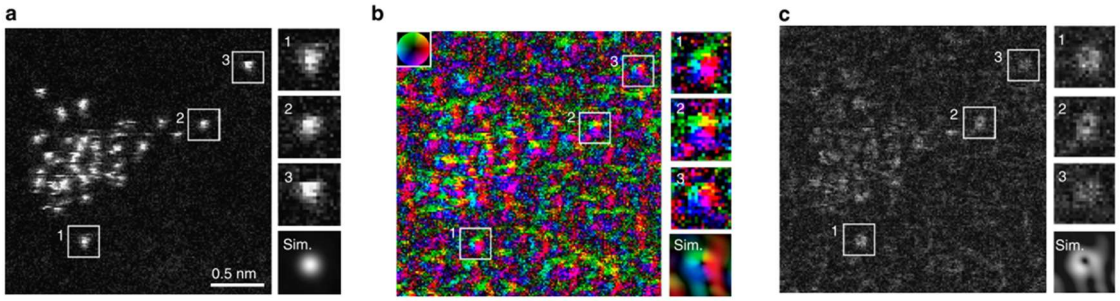

Figure 5. Simultaneous atomic-resolution ADF STEM image and electric field vector map and electric field strength map of Au single atoms. (a) ADF STEM image. (b,c) Electric field vector and electric field strength maps constructed from the segmented-detector STEM images. The inset color wheel indicates how color and shade denote the electric field orientation and strength. Simulated single Au atom images are also shown, which include a 10 nm-thick amorphous carbon substrate beneath the single Au atom. (N. Shibata et al., *Nat. Commun.* **2017**, *8,* 1–7.)

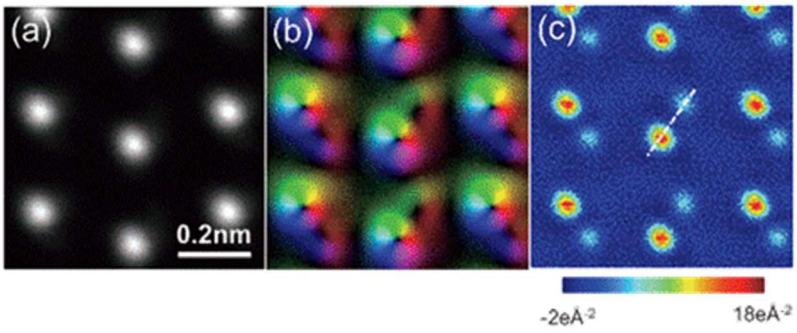

Figure 6. Quantitative mapping of the GaN projected total charge density in real-space by aberration-corrected DPC-STEM. (a) Experimental atomic resolution Z-contrast image for a GaN single crystal down the [11$\bar{2}$0] axis. The scale bar corresponds to 10 Å. (b) A projected electric field for GaN obtained from the experimental data. The color and brightness, respectively, denote the direction and magnitude of the field. (c) Projected total charge density map calculated from (b). The scale bars correspond to 2 Å. (G. Sánchez-Santolino et al., *ACS Nano* **2018***, 12,* 8875–8881.)

Acknowledgements

The author would like to express his sincerest gratitude Professor Tetsu Yonezawa, Division of Materials Science and Engineering, Faculty of Engineering, Hokkaido University, for his kind guidance, helpful suggestions, and hearty encouragement through this work.

The author would like to express his sincerest appreciation to associated professor, Yohei Ishida, Division of Materials Science and Engineering, Faculty of Engineering, Hokkaido University, for his helpful advices and suggestions.

The author would like to thank Mr. Ryo Oota and Ms. Naomi Hirai, for their sincere technical supports on the operation of electron microscopy.

The author would like to thank the members of Novel Materials Hybrid Engineering Laboratory at Hokkaido University, for their continuing collaborations, and hearty supports during the course of this study.

Finally, the author is particularly grateful to her parents, Mr. Jun-ichi Akita and Mrs. Toshie Akita for their understanding and long lasting support.

2021

Ikumi AKITA